FreeBook

CRC Press
Taylor & Francis Group

Advances in Remote Sensing of Vegetation

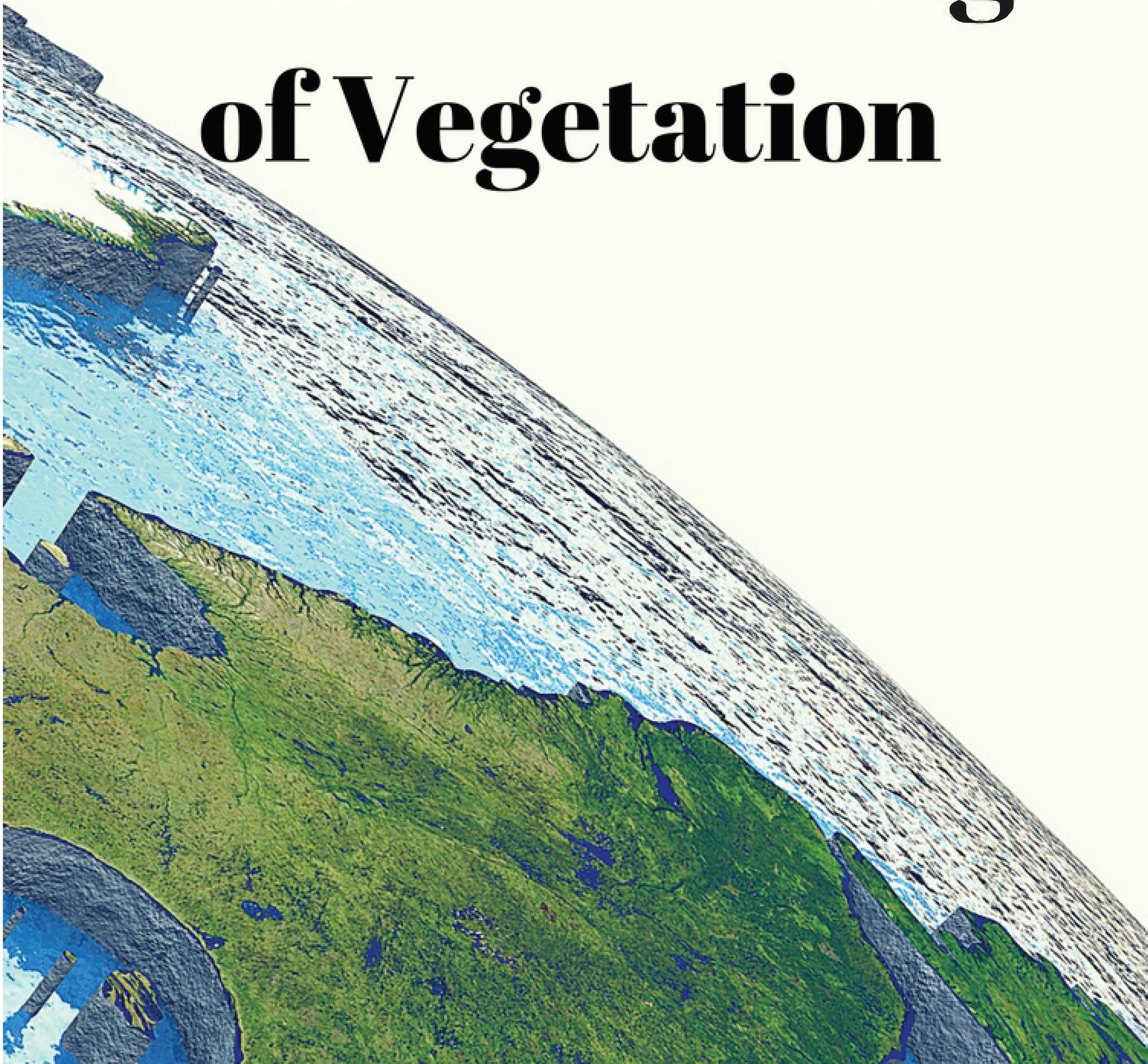

Table of Contents

Save on Essential Books in Remote Sensing

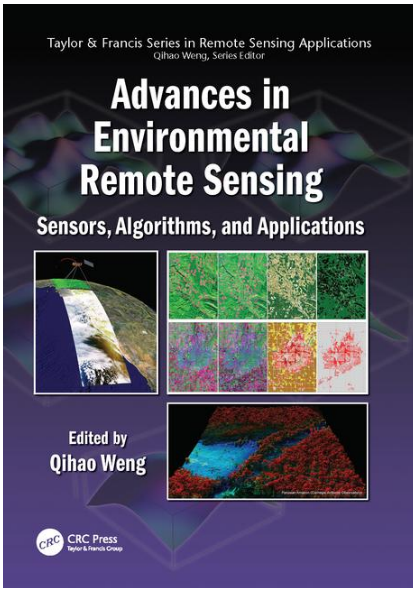

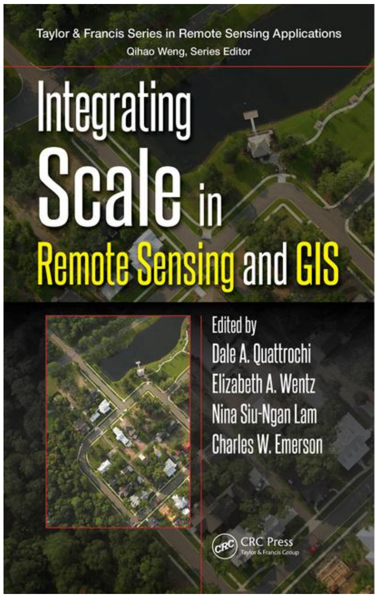

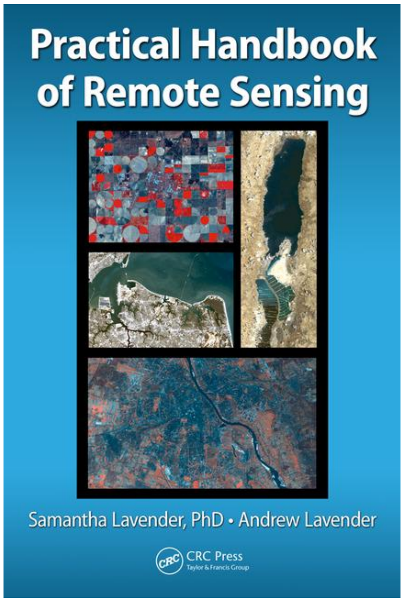

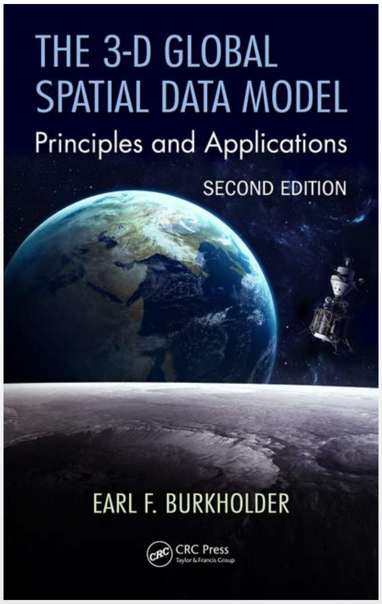

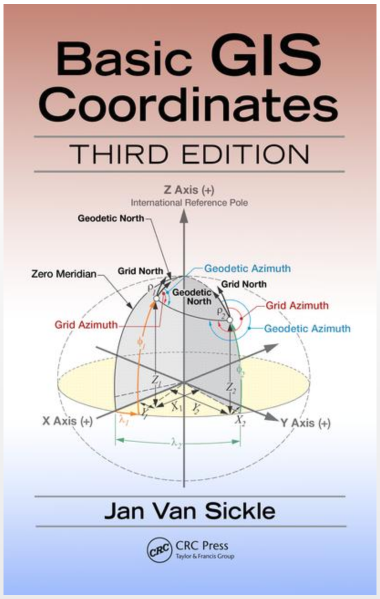

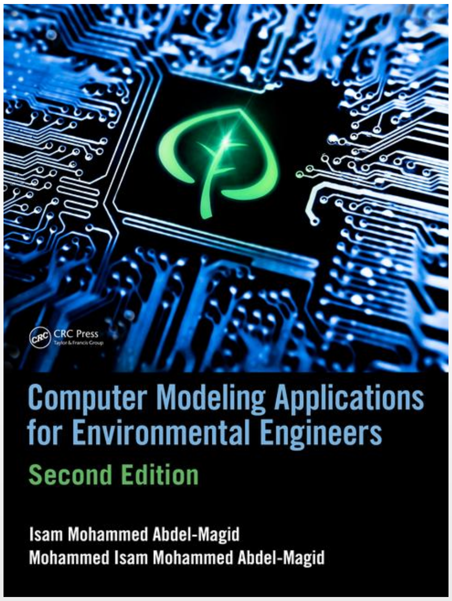

SAVE 20%* + Receive *FREE Shipping!

Visit crcpress.com to browse our collection of books in GIS & Remote Sensing

Enter code *FBK17* at time of checkout.

Introduction

The main purpose of compiling this FREE BOOK, **Advances in Remote Sensing of Vegetationis** to provide comprehensive review articles from leading authorities to examine the developments in concepts, methods, techniques, and applications in vegetation remote sensing. The articles selected from published books can serve as references to researchers, scientists, engineers, and policy- makers who wish to keep up with new developments in environmental remote sensing.

Chapter 1 provides an overview of spectral characteristics for a set of plant biophysical and biochemical parameters. A wide range of techniques are reviewed, including spectral derivative analysis, spectral matching, spectral index analysis, hyperspectral transformation, spectral unmixing analysis, and hyperspectral classifications. Also, discusses two general analytical approaches empirical/ statistical methods and physically based modeling. The chapter concludes with the authors'perspectives on the future directions of hyperspectral remote sensing of vegetation biophysical parameters.

The improvement of object-based image analysis OBIA software capacity and the increased availability of high spatial resolution satellite images and LiDAR data, vegetation-mapping capabilities are expected to grow rapidly in terms of both the accuracy and the amount of biophysical vegetation parameters that can be retrieved Chapter 2 reviews the development of OBIA and the current status of its application in vegetation mapping. Two case studies are provided to illustrate this mapping capacity. The first case uses LiDAR data to map riparian zone extent and to estimate plant project cover (PPC) within the riparian zone in central Queensland, Australia and the second case study aims at extracting individual tree crowns from a digital surface model (DSM) by using OBIA and grid computing techniques in the federal state of Upper Austria, Austria.

Image classification is a fundamental protocol in digital image processing and pro-vides crucial information for subsequent environmental and socioeconomic applications. Generating a satisfactory classification image from remote sensing data is not a straight-forward task. Chapter 3 provides a brief overview of the major steps in image classification, and examines the techniques for improving classification performance, including the use of spatial information, multitemporal and ancillary data, and image fusion. A case study explores the role of vegetation indices and textural images in improving vegetation classification performance in a moist tropical region of the Brazilian Amazon with Landsat Thematic Mapper (TM) imagery.

Thermal infrared (TIR) remote sensing techniques have been applied in urban climate and environmental studies. Chapter 4 examines the current practices, problems, and prospects of this particular field of study, especially the applications of remotely sensed TIR data in urban studies. The majority of previous researches have focused on land-surface temperature (LST) patterns and their relationships with urban-surface biophysical characteristics, especially with vegetation indices and land-use/land-cover types. Less attention has been paid to the derivation of urban heat island (UHI) parameters from LST data and to the use of remote sensing techniques to estimate surface energy fluxes. This chapter outlines the major recent advances, future research directions, and the impacts of planned TIR sensors with LDCM and HyspIRI missions.

LiDAR has been increasingly used in many geospatial applications due to its high data resolution, low consumption of time and cost, compared to many traditional remote sensing technologies. Unlike other remotely sensed data, LiDAR data focus solely on geometry rather than on radiometry. Chapter 5 offers a detailed introduction of the basic concept of LiDAR, and types of sensors and platforms. This chapter further provides a review of LiDAR remote sensing applications in estimating forest biophysical parameters and surface and canopy fuels, and for characterizing wildlife habitats.

Please note this Free Book does not include references, endnotes and footnotes.Fully referenced versions of each book can be accessed through crcpress.com.

Chapter 1

Hyperspectral Remote Sensing of Vegetation Bioparameters

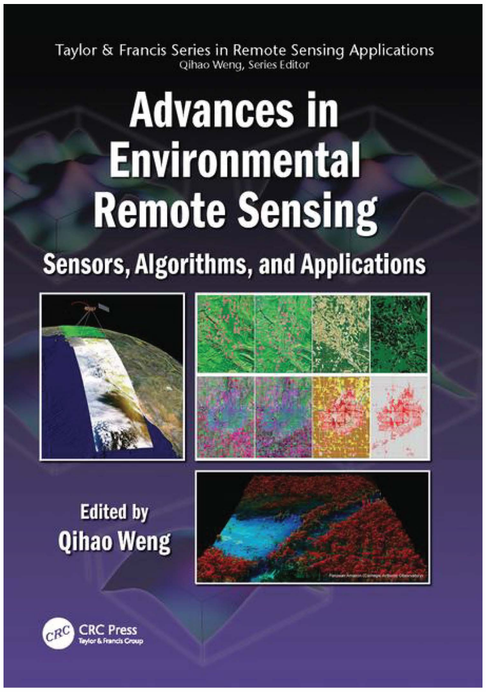

Advances in Environmental Remote Sensing: Sensors, Algorithms, and Applications

By Qihao Weng

© 2011 Taylor & Francis Group. All rights reserved.

To purchase a copy, click here.

The spectral reflectance properties and characteristics of a list of typical plant bio parameters, including the biophysical and biochemical parameters (Table 5.1), have been the subject of systematic plant spectral reflectance studies. Typical biophysical parameters for their spectral analysis consist of vegetation canopy LAI, specific leaf area (SLA), crown closure.

TABLE 5.1

Typical Plant Biophysical and Biochemical Parameters

Biophysical Parameter	Definition and Description	Spectral Response and Characteristics
LAI	The total one-sided area of all leaves in the canopy per unit area of ground.	The absorption spectral features caused by pigments in the visible region and by water content and other biochemicals in the SWIR region are useful for extracting and mapping LAI and CC.
SLA	Projected leaf area per unit leaf dry mass (cm^2/g).	Not directly related to water absorption bands, but SLA is a leaf structural property linked to the entire constellation of foliar chemicals and photosynthetic processes.
CC	Percentage of land area covered by the vertical projection of plants (tree crowns).	Same as that for LAI.
Species	Various plant species and species composition.	Spectral differences due to differences and variation in phenology/ physiology, internal leaf structure, biochemicals, and ecosystem type.
Biomass	The total of absolute amount of vegetation present (often considered in terms of the aboveground biomass) per unit area of ground.	Spectral responses to LAI, stand/ community structure, species and species composition, and image textural information.
NPP	The net flux of carbon between the atmosphere and terrestrial vegetation can be expressed on an annual basis in terms of net biomass accumulation, or NPP (Goetz and Prince 1996).	Spectra reflect vegetation condition and changes in LAI or canopy light absorption through time in visible and NIR regions.
fPAR	Effective absorbed fPAR in the visible region.	In the visible spectral region 400–700 nm, most absorbed by plant pigments, such as Chl-a and -b, Cars, and Anths; and leaf water and N contents for photosynthesis.
Chls (Chl-a, Chl-b)	Green pigments Chl-a and Chl-b for plant photosynthesis processing, found in green photosynthetic organisms, (mg/m^2 or $nmol/cm^2$).	Chl-a absorption features are near 430 and 660 nm, and Chl-b absorption features are near 450 and 650 nm in vivo (Lichtenthaler 1987; Blackburn 2006). But it is known that in situ Chl-a absorbs at both 450 and 670 nm.
Cars	Any of a class of yellow to red pigments, including carotenes and xanthophylls (mg/m^2).	Cars absorption feature in the blue region is near 445 nm in vivo (Lichtenthaler 1987). But it is known that in situ Cars absorb at 500 nm and even at a little bit longer wavelength.
Anths	Any of various water-soluble pigments that impart to flowers and other plant parts colors ranging from violet and blue to most shades of red (mg/m^2).	Anths absorption feature in the green region is at 530 nm in vivo, but in situ Anths absorb around 550 nm (Gitelson et al. 2001, 2009; Blackburn 2006).
N	Plant nutrient element (%).	The central wavelengths of N absorption features are near 1.51, 2.06, 2.18, 2.30, and 2.35 μm.

TABLE 5.1 (*Continued*)

Biophysical Parameter	Definition and Description	Spectral Response and Characteristics
P	Plant nutrient element (%).	No direct and significant absorption features across 0.40–2.50 μm, but it does indirectly affect the spectral characteristics of other biochemical compounds.
K	Plant nutrient element (%).	Foliar K concentration has only a slight effect on sclerenhyma cell walls, and thus on NIR reflectance.
W	Leaf or canopy water content or concentration (%).	The central wavelengths of those absorption features are near 0.97, 1.20, 1.40, and 1.94 μm.
Lignin	A complex polymer, the chief noncarbohydrate constituent of wood, which binds to cellulose fibers and hardens and strengthens the cell walls of plants (%).	The central wavelengths of lignin absorption features are near 1.12, 1.42, 1.69, and 1.94 μm.
Cellulose	A complex carbohydrate, which is composed of glucose units, and forms the main constituent of the cell wall in most plants (%).	The central wavelengths of cellulose absorption features are near 1.20, 1.49, 1.78, 1.82, 2.27, 2.34, and 2.35 μm.
Protein	Any of a group of complex organic macromolecules that contain carbon, hydrogen, oxygen, N, and usually sulfur, and are composed of one or more chains of amino acids (%).	The central wavelengths of protein absorption features are near 0.91, 1.02, 1.51, 1.98, 2.06, 2.18, 2.24, and 2.30 μm.

(CC), vegetation species and composition, biomass, effective absorbed fPAR, and net primary productivity (NPP), which reflect photosynthesis rate. Typical biochemical parameters are major pigments (Chls, carotenoids [Cars], and anthocyanins [Anths]), nutrients (nitrogen [N], phosphorus [P], and potassium [K]), leaf or canopy water content (W), and other biochemicals (e.g., lignin, cellulose, and protein). Analysis results are useful for determining the physicochemical properties of plants derived from spectral data and helpful for extracting bioparameters in order to assess vegetation and ecosystem conditions. Some analysis results of spectral characteristics for the list of typical biophysical and biochemical parameters from hyperspectral data are summarized in Sections 5.2.1 through 5.2.7.

Leaf Area Index, Specific Leaf Area, and Crown Closure

The LAI, SLA, and CC are important structural parameters for quantifying the energy and mass exchange characteristics of terrestrial ecosystems such as photosynthesis, respiration, transpiration, the carbon and nutrient cycle, and rainfall interception. The LAI parameter quantifies the amount of live green leaf material present in the canopy per unit ground area, whereas SLA describes the amount of leaf dry mass present in the plant canopy. The CC parameter can only quantify the percentage of area covered by the vertical projection of live green leaf material present in the canopy. The physiological and structural characteristics of plant leaves determine their typically low visible-light reflectance, except in green light. The high NIR reflectance of vegetation allows optical remote sensing to capture detailed information about the live, photosynthetically active forest canopy structure, and thus help understand the mass exchange between the atmosphere and the plant ecosystem.

As LAI and CC increase, many absorption features become significant due to changes in their amplitude, width, or location. The absorption features, including those caused by pigments in the visible region and by water content and other biochemicals in the shortwave infrared (SWIR) region, are useful in extracting and mapping LAI and CC. Different from LAI and CC, the spectral properties of SLA are not directly related to water absorption bands in the full range of a vegetation spectrum. However, SLA has a leaf structural property linked to the entire constellation of foliar chemicals and photosynthetic processes. It is related to the NIR spectral reflectance that is dominated by the amount of leaf water content and leaf thickness. Thus, at the leaf level, SLA is highly correlated with leaf spectral reflectance.

Optical remote sensing, especially hyperspectral remote sensing, is aimed at retrieving the spectral characteristics of leaves, quantified by LAI, SLA, and CC, which are determined by the internal biochemical structure and pigments content of leaves. Currently, many spectral analysis techniques and methods are available for extracting and assessing the biophysical parameters LAI, SLA, and CC from various hyperspectral sensors, especially imaging spectrometers, such as spectral derivatives, spectral position variables, spectral indices, and physically based models.

Species and Composition

Foliage spectral variability among individual species, or even within a single crown, is attributed not only to differences in internal leaf structure and biochemicals but also to difference and variation in the phenology/physiology of plant species. In addition, the relative importance of these biochemical and structural properties among individual species is also dependent on measured wavelength, pixel size, and ecosystem type. Few studies have been systematically carried out to determine the best wavelengths suitable for species recognition in the field. This obviously depends on species-specific biochemical characteristics that are related to foliar chemistry. Martin and Aber used AVIRIS data to estimate the N and lignin content in forest canopy foliage. Although either of the two by itself is insufficient to identify species, combined information can differentiate between species. For example, red pine and hemlock were reported to have very similar N concentration, but very different levels of lignin. Pu used 30 selected spectral variables evaluated by analysis of variance (ANOVA) from in situ hyperspectral data to identify 11 broadleaf species in an urban environment. Among the 30 selected spectral variables, most of the spectral variables are directly related to leaf chemistry. For example, some selected spectral variables are related to water absorption bands around 0.97, 1.20, and 1.75 μm, and the others are related to spectral absorption features of Chls, red-edge optical parameters, simple ratio (SR), vegetation index (VI), and reflectance at 680 nm, and other biochemicals such as lignin (near 1.20 and 1.42 μm), cellulose (near 1.20 and 1.49 μm), and N. In identifying invasive species in Hawaiian forests from native and other introduced species by remote sensing, Asner et al. confirmed the viewpoint that the observed differences in canopy spectral signatures are linked to relative differences in measured leaf pigments (Chls and Cars), nutrients (N and P), and structural (SLA) properties, as well as to canopy LAI.

Biomass

Leaf canopy biomass is calculated as the product of the leaf dry mass per area (LMA; unit: g/m^2, or the inverse of SLA) and LAI. Therefore, based on the spectral responses to LAI and LMA, both biophysical parameters can be estimated from hyperspectral data; thus, the leaf mass of the entire canopy is estimated. Many VIs, such as the normalized difference VI (NDVI) and the SR constructed with NIR and red bands have been developed and directly applied to estimate leaf or canopy biomass. It has been recommended that VIs remove variability caused by canopy geometry, soil background, sun view angles, and atmospheric conditions when measuring biophysical properties. Broadband VIs use, in principle, average spec- tral information over a wide range, resulting in the loss of critical spectral information available in specific narrow (hyperspectral) bands. Since many narrow bands are available for constructing VIs, selection of the correct wavelengths and bandwidths is important. When some VIs derived from hyperspectral data are used to estimate some biophysical parameters, narrow bands (10 nm) perform better than broadband (e.g., TM bands) using standard red/NIR and green/NIR. For example, $NDVI_{SWIR}$ constructed with reflectances at wavelengths 1540 and 2160 nm is the best index for leaf mass estimation; many hyperspectral bands in the SWIR region and some in the NIR region have the greatest potential to form spectral indices for LAI estimation.

Pigments: Chlorophylls, Carotenoids, and Anthocyanins

The Chls (Chl-a and Chl-b) are Earth’s most important organic molecules, as they are the most important pigments necessary for photosynthesis. The second major group of plant pigments, composed of carotene and xanthophylls, is Cars, whereas Anths are water-soluble flavonoids, which form the third major group of pigments in leaves, but there is no unified explanation for their presence and function. Published spectral absorption wavelengths of isolated pigments show that Chl-a absorption features are around 430 and 660 nm and Chl-b absorption features are around 450 and 650 nm in vivo. But it is known that in situ Chl-a absorbs at both 450 and 670 nm. Cars absorption feature in the blue region is at 445 nm in vivo and β-carotene at 470 nm in vivo. But it is also known that *in situ* Cars absorb at 500 nm and even at wavelengths that are a little bit longer. The absorption feature of Anths in the green region is at 530 nm in vivo, but *in situ* Anths absorb around 550 nm.

Based on the spectral properties of the pigments, some researchers have used red edge optical parameters to estimate plant leaf and canopy Chls content and concentration. However, most of them have developed and used various VIs, constructed in either ratios or normalized difference ratios of two narrow bands in the visible and NIR regions, to estimate the major plant pigments Chls, Cars, and Anths at leaf or canopy levels. In addition, many researchers also employ physically based models at leaf or canopy levels to retrieve the pigments and use data transform approaches like wavelet analysis to retrieve Chl concentration from leaf reflectance.

Nutrients: Nitrogen, Phosphorous, and Potassium

The foliage and canopy N is related to a variety of ecological and biochemical processes. It is the most important nutrient element needed by plants for growth. The second and third most limiting nutrient constituents, P and K, are essential in all phases of plant growth; they are used in cell division, fat formation, energy transfer, seed germination, and flowering and fruiting. Among the three basic nutrient elements, N has significant absorption features that have been found in the visible, NIR, and SWIR regions. According to Curran, N absorption features in their isolated form are located around 1.51, 2.06, 2.18, 2.30, and 2.35 μm. Since many biochemical compounds comprise N, such as Chls and protein, their spectral properties are also characterized by N concentration in plant leaves. It seems that P has no direct and significant absorption features across the visible, NIR, and SWIR regions, but it does indirectly affect the spectral characteristics of other biochemical com- pounds. The documented spectral changes include a higher reflectance in the green and yellow portions of the electromagnetic spectrum in P-deficient plants and a difference in the position of the long-wavelength edge (the red edge) of Chl absorption band centered around 0.68 μm. Foliar K concentration has only a slight effect on needle morphology, thereby affecting NIR reflectance. This is because the sclerenchyma cell walls are thicker, with a high K concentration, which leads to higher NIR reflectance of leaves.

To estimate nutrient concentrations from hyperspectral data, including in situ spectral measurements and imaging data, many analysis techniques and methods have been developed. They include spectral derivatives, spectral indices, spectral position variables, continuum-removal method, statistical regression, and inversion of physically based models.

Leaf or Canopy Water Content

The evaluation of water status in vegetation is an important component of hyperspectral remote sensing. Previous work on assessing the plant water status mainly depended on water spectral absorption features in the 0.40–2.50 μm region. According to Curran, the central wavelengths of the absorption features are around 0.97, 1.20, 1.40, and 1.94 μm. In addition, the reflectance of dry vegetation shows an absorption feature centered at 1.78 μm by other chemicals rather than by water, because pure water does not cause such an absorption feature. In general, the reflectance spectra of green and yellow leaves in those absorption bands are quickly saturated and solely dominated by changes in the leaf water content.

To extract these spectral absorption features, one of the most important techniques is to make use of VIs. Other analysis techniques include spectral derivatives, spectral position variables, continuum-removal method, statistical regression, and inversion of physically based models.

Other Biochemicals: Lignin, Cellulose, and Protein

The spectral absorption features of other biochemicals are mostly located in the SWIR region (1.00–2.50 μm). According to Curran, the central wavelengths of lignin absorption features are around 1.12, 1.42, 1.69, and 1.94 μm; the central wavelengths of cellulose absorption features are around 1.20, 1.49, 1.78, 1.82, 2.27, 2.34, and 2.35 μm; and the central wavelengths of protein absorption features are around 0.91, 1.02, 1.51, 1.98, 2.06, 2.18, 2.24, and 2.30 μm. So far, most techniques for estimating the concentrations of lignin, cellulose, and protein from hyperspectral data use derivative spectra, logarithmspectra, spectral indices, and/or statistical regression.

Analysis Techniques and Methods

There are many analysis techniques and methods that currently are available to be used for extracting and assessing bioparameters from various hyperspectral data. A total of nine types or categories of the techniques and methods are reviewed in following Sections.

Derivative Analysis

In situ data or imaging hyperspectral data obtained in the field are rarely from a single object. They are contaminated by illumination variations caused by terrain relief, cloud, and viewing geometry. The spectral reflectance of a target of interest could also be affected by radiometric contributions from background materials like soil spectra. Derivative analysis has been considered a desirable tool in removing or compressing the effect of illumination variations. It has also proven effective in reducing background effects when the spectral pattern of background materials has a lower frequency of variation. For derivative analysis of hyperspectral data, a finite approximation can be applied to calculate the first- and second-order derivative spectra as follows:

$$\rho'(\lambda_i) \approx [\rho(\lambda_{i+1}) - \rho(\lambda_{i-1})]/\Delta\lambda \tag{5.1}$$

and

$$\begin{aligned}\rho''(\lambda_i) &\approx [\rho'(\lambda_{i+1}) - \rho'(\lambda_{i-1})]/\Delta\lambda \\ &\approx [\rho(\lambda_{i+1}) - 2\rho(\lambda_i) + \rho(\lambda_{i-1})]/\Delta\lambda^2\end{aligned} \tag{5.2}$$

where $\rho'(\lambda_i)$ and $\rho''(\lambda_i)$ are the first and second derivatives, respectively, $\rho(\lambda_i)$ is reflectance at a wavelength (band) i, and $\Delta\lambda$ is the wavelength interval between λ_{i+1} and λ_{i-1} equal to twice the bandwidth in this case.

Derivative spectra have been successfully employed in hyperspectral data analysis for biophysical and biochemical parameter extraction. It is believed that the accuracy of derivative analysis is sensitive to the signal-to-noise ratio of hyperspectral data and higher-order spectral derivative processing is susceptible to noise. Lower- order derivatives (e.g., the first-order derivative) are less sensitive to noise and hence more effective in operational remote sensing. For example, Gong, Pu, and Yu report that the first derivative of tree spectra could considerably improve the accuracy of recognizing six conifer species commonly found in northern California.

Spectral Matching

Researchers van der Meer and Bakker developed a cross-correlogram spectral matching (CCSM) technique, taking into consideration the correlation coefficient between a target spectrum and a reference spectrum, the skewness of the spectra, and criterion of correlation significance. A cross-correlogram (i.e., CCSM) is constructed by calculating the cross-correlation at different match positions between a test (target) spectrum and a reference (a laboratory or pixel spectrum known to characterize a target of interest) spectrum, and is suitable for processing hyperspectral data. Further, van der Meer compared spectral angle mapper (SAM) with the vector CCSM between a known reference and an unknown target spectrum and the spectral information divergence in differentiating the minerals alunite, kaolinite, montmorillonite, and quartz using both synthetic and real (i.e., AVIRIS) hyperspectral data of a (artificial or real) hydrothermal alteration system. The SID measures the discrepancy in probability distributions between two pixel vectors. His results suggest that SID and CCSM outperform SAM, and that SID is more effective in mapping the four minerals.

Given two spectral signature curves, $\rho_r = (\rho_{r1}, \rho_{r2}, \ldots, \rho_{rL})^T$ and $\rho_t = (\rho_{t1}, \rho_{t2}, \ldots, \rho_{tL})^T$, these measures are defined as follows:

$$\text{Cross-correlation } r_m = \frac{n\sum\rho_r\rho_t - \sum\rho_r\sum\rho_t}{\sqrt{\left[n\sum\rho_r^2 - \left(\sum\rho_r\right)^2\right]\left[n\sum\rho_t^2 - \left(\sum\rho_t\right)^2\right]}} \tag{5.3}$$

where the cross-correlation r_m, at each match position m, is equivalent to the linear correlation coefficient and is defined as the ratio of covariance to the product of the sum of standard deviations; n is the effective number of bands when calculating the CCSM; and L is total number of bands ($n < L$).

SID is given by

$$\mathrm{SID}_{(\rho_r,\rho_t)} = D(\rho_r \| \rho_t) + D(\rho_t \| \rho_r) \tag{5.4}$$

where

$$D(\rho_t \parallel \rho_r) = \sum_{l=1}^{L} q_l D_l(\rho_t \parallel \rho_r) = \sum_{l=1}^{L} q_l [I_l(\rho_r) - I_l(\rho_t)] \tag{5.5}$$

and

$$D(\rho_r \parallel \rho_t) = \sum_{l=1}^{L} p_l D_l(\rho_r \parallel \rho_t) = \sum_{l=1}^{L} p_l [I_l(\rho_t) - I_l(\rho_r)] \tag{5.6}$$

Equations 5.5 and 5.6 are derived from the probability vectors $p = (p_1, p_2, \ldots, p_L)^T$ and $q = (q_1, q_2, \ldots, q_L)^T$ for the spectral signatures of vectors ρ_r and ρ_t, where $p_k = \rho_{rk} / \sum_{l=1}^{L} \rho_{rl}$, $q_k = \rho_{tk} / \sum_{l=1}^{L} \rho_{tl}$, $I_l(\rho_t) = -\log q_l$, and similarly $I_l(\rho_r) = -\log p_l$. Measures $I_l(\rho_t)$ and $I_l(\rho_r)$ are referred to as the "self-information" of ρ_t for band l. Note that Equations 5.5 and 5.6 represent the relative entropy of ρ_t with respect to ρ_r (indicated by the ‖ symbol).

In the study of the spectroscopic determination of two health levels of the coast live oak leaves, Pu, Kelly et al. used the CCSM algorithm to discriminate between healthy and infected leaves by matching unknown leaf spectra with known infected leaf spectra in association with water stress. Wang et al. also classified land-cover types with the CCRM spectral matching technique. In spectral matching, it should be noted that the accuracy of spectral matching techniques (e.g., CCSM) is directly affected by geometry of sensors' observations and target size. This effect can be minimized by performing spectral normalization before conducting spectral matching. In general, such matching techniques are more useful for change detection of scene components than for identification of the unknown scene components.

Spectral Index Analysis

When multispectral data is used to construct various spectral VIs, the advantage of VIs is their ease of use. When using hyperspectral data to conduct spectral VI analysis, hyperspectral remote sensing has the added advantage of increased chance and flexibility to choose spectral bands. With multispectral data, one may have only the choice to use the red and NIR bands. However, with hyperspectral data, one can choose many such red and NIR narrowband combination. Accordingly, spectral VIs applied to hyperspectral data are called "narrowband VIs". Table 5.2 lists a set of 66 VIs that are developed for hyperspectral data. These VIs frequently appear in the literature on extracting and evaluating plant biophysical and biochemical parameters from hyperspectral data. The 66 VIs are grouped into five categories so that readers can conveniently locate a VI (or a group of VIs), based on the characteristics and functions of the VIs: (1) multiple bioparameters, (2) pigments (Chls, Cars, and Anths), (3) foliar chemistry, (4) water, and (5) stress. Within individual categories, the VIs are arranged in alphabetical order. A brief review of these VIs is given in this section.

Specifically, the use of VIs for extracting and assessing vegetation LAI, SLA, and CC includes the use of enhanced VI (EVI), two-band enhanced VI (EVI2), greenness index (GI), LAI determining index (LAIDI), modified Chl absorption ratio index 1 (MCARI1), modified Chl absorption ratio index 2 (MCARI2), modified SR (MSR), modified triangular VI 1 (MTVI1), modified triangular VI 2 (MTVI2), normalized difference infrared index

TABLE 5.2

Summary of 66 Spectral Indices Extracted from Hyperspectral Data, Collected from the Literature

Spectral Index	Characteristics and Functions	Definition	Reference
Multiple Bioparameters			
ATSAVI	Less affected by soil background and better for estimating homogeneous canopy.	$a(R_{800} - aR_{670} - b)/[(aR_{800} + R_{670} - ab + X(1 + a^2)]$, where $X = 0.08$, $a = 1.22$, and $b = 0.03$	Baret and Guyot 1991
EVI	Estimate vegetation LAI, biomass, and water content, and improve sensitivity in high-biomass regions.	$2.5(R_{NIR} - R_{red})/(R_{NIR} + 6R_{red} - 7.5R_{blue} + 1)$	Huete et al. 2002
EVI2	Similar to EVI, but without blue band and good for atmospherically corrected data.	$2.5(R_{NIR} - R_{red})/(R_{NIR} + 2.4R_{red} + 1)$	Jiang et al. 2008
GI	Estimate biochemical constituents and LAI at leaf and canopy levels.	R_{554}/R_{677}	Zarco-Tejada, Berjon et al. 2005
LAIDI	Sensitive to LAI variation at canopy level with a saturation point >8.	R_{1250}/R_{1050}	Delalieux et al. 2008
Improved Soil Adjusted Vegetation Index (MSAVI)	A more sensitive indicator of vegetation amount than SAVI at canopy level.	$0.5[2R_{800} + 1 - ((2R_{800} + 1)^2 - 8(R_{800} - R_{670}))^{1/2}]$	Qi et al. 1994
MSR	More linearly related to vegetation parameters than RDVI.	$(R_{800}/R_{670} - 1)/(R_{800}/R_{670} + 1)^{1/2}$	Chen 1996; Haboudane et al. 2004
MTVI1	More suitable for LAI estimation than TVI.	$1.2[1.2(R_{800} - R_{550}) - 2.5(R_{670} - R_{550})]$	Haboudane et al. 2004
MTVI2	Preserves sensitivity to LAI and resistance to Chl influence.	$\{1.5[1.2(R_{800} - R_{550}) - 2.5(R_{670} - R_{550})]\}/\{(2R_{800} + 1)^2 - [6R_{800} - 5(R_{670})^{1/2}] - 0.5\}^{1/2}$	Haboudane et al. 2004
NDVI	Responds to change in the amount of green biomass and more efficiently in vegetation with low to moderate density.	$(R_{NIR} - R_R)/(R_{NIR} + R_R)$	Rouse et al. 1973
Optimized soil-adjusted VI (OSAVI)	Similar to MSAVI, but more applicable in agricultural applications, whereas MSAVI is recommended for more general purposes.	$1.16(R_{800} - R_{670})/(R_{800} + R_{670} + 0.16)$	Rondeaux et al. 1996
PSND	Estimate LAI and Cars at leaf or canopy level.	$(R_{800} - R_{470})/(R_{800} + R_{470})$	Blackburn 1998

PVI_{hyp}	More efficiently quantify the low amount of vegetation by minimizing soil background influence on vegetation spectrum.	$(R_{1148} - aR_{807} - b)/(1 + a^2)^{1/2}$, where $a = 1.17$ and $b = 3.37$	Schlerf et al. 2005
RDVI	Suitable for low to high LAI values.	$(R_{800} - R_{670})/(R_{800} + R_{670})^{1/2}$	Reujean and Breon 1995; Haboudane et al. 2004
sLAIDI	Sensitive to LAI variation at canopy level with a saturation point >8.	$S(R_{1050} - R_{1250})/(R_{1050} + R_{1250})$, where $S = 5$	Delalieux et al. 2008
SPVI	Estimate LAI and canopy Chls.	$0.4[3.7(R_{800} - R_{670}) - 1.2 \mid R_{530} - R_{670} \mid]$	Vincini et al. 2006
TCARI	Similar to OSAVI, but very sensitive to Chls content variations and very resistant to the variations of LAI and solar zenith angle.	$3[(R_{700} - R_{670}) - 0.2(R_{700} - R_{550})(R_{700}/R_{670})]$	Haboudane et al. 2002
SR	Same as NDVI.	R_{NIR}/R_R	Jordan, 1969
Visible atmospherically resistant index for green ref. ($VARI_{green}$)	Estimate green vegetation fraction (VF) with minimally sensitive to atmospheric effects with an error of <10%; better than NDVI for moderate to high VF values of VF.	$(R_{green} - R_{red})/(R_{green} + R_{red})$	Gitelson, Kaufman et al. 2002
VARI for red edge ref. ($VARI_{red\text{-}edge}$)	Same as $VARI_{green}$.	$(R_{red\text{-}edge} - R_{red})/(R_{red\text{-}edge} + R_{red})$	Gitelson, Kaufman et al. 2002
WDRVI	Estimate LAI, vegetation cover, biomass; better than NDVI.	$(0.1R_{NIR} - R_{red})/(0.1R_{NIR} + R_{red})$	Gitelson 2004
Pigments (Chls, Cars, and Anths)			
ARI	Estimate Anths content from reflectance changes in the green region at leaf level.	$ARI = (R_{550})^{-1} - (R_{700})^{-1}$	Gitelson, Merzlyak, and Chivkunova 2001
BGI	Estimate Chls and Cars content at leaf and canopy levels.	R_{450}/R_{550}	Zarco-Tejada, Berjon et al. 2005
BRI	Estimate Chls and Cars content at leaf and canopy levels.	R_{450}/R_{690}	Zarco-Tejada, Berjon et al. 2005
CARI	Quantify Chls concentration at leaf level.	$(\mid (a670 + R_{670} + b) \mid / (a^2 + 1)^{1/2}) \times (R_{700}/R_{670})$ $a = (R_{700} - R_{550})/150,\ b = R_{550} - (a \times 550)$	Kim et al. 1994
Chl_{green}	Estimate Chls content in anthocyanin-free leaves if NIR is set.	$(R_{760-800}/R_{540-560})^{-1}$	Gitelson, Keydan, and Merzlyak 2006

TABLE 5.2 (*Continued*)

Summary of 66 Spectral Indices Extracted from Hyperspectral Data, Collected from the Literature

Spectral Index	Characteristics and Functions	Definition	Reference
$\text{Chl}_{\text{red-edge}}$	Estimate Chls content in anthocyanin-free leaves if NIR is set.	$(R_{760-800}/R_{690-720})^{-1}$	Gitelson, Keydan, and Merzlyak 2006
CRI	Sufficient to estimate total Cars content in plant leaves.	$\text{CRI}_{550} = (R_{510})^{-1} - (R_{550})^{-1}$, $\text{CRI}_{700} = (R_{510})^{-1} - (R_{700})^{-1}$	Gitelson et al. 2002
DD	Estimate total Cars content in plant leaves.	$(R_{750} - R_{720}) - (R_{700} - R_{670})$	le Maire, Francois, and Dufrene 2004
DmSR	Quantify Chls content at leaf level.	$(DR_{720} - DR_{500})/(DR_{720} + DR_{500})$, where DR_{λ} is first derivative of ref. at wavelength λ	le Maire, Francois, and Dufrene 2004
EPI	Correlate best with Chl-a, Chls, and total Car contents.	$a \times R_{672}/(R_{550} \times R_{708})^{\beta}$	Datt 1998
LCI	Estimate Chl content in higher plants, sensitive to variation in reflectance caused by Chl absorption.	$(R_{850} - R_{710})/(R_{850} + R_{680})$	Datt 1999
mARI	Estimate anthocyanin content from reflectance changes in the green region at leaf level.	$\text{mARI} = ((R_{530-570})^{-1} - (R_{690-710})^{-1}) \times R_{NIR}$	Gitelson, Keydan, and Merzlyak 2006
MCARI	Respond to Chl variation and estimate Chl absorption.	$[(R_{701} - R_{671}) - 0.2(R_{701} - R_{549})]/(R_{701}/R_{671})$	Daughtry et al. 2000
MCARI1	Less sensitive to Chl effects; more responsive to green LAI variation.	$1.2[2.5(R_{800} - R_{670}) - 1.3(R_{800} - R_{550})]$	Haboudane et al. 2004
MCARI2	Preserves sensitivity to LAI and resistance to Chl influence.	$\{1.5[2.5(R_{800} - R_{670}) - 1.3(R_{800} - R_{550})]\}/\{(2R_{800} + 1)^2 - [6R_{800} - 5(R_{670})^{1/2}] - 0.5\}^{1/2}$	Haboudane et al. 2004
mCRI	Estimate Car pigment contents in foliage.	$\text{mCRI}_G = ((R_{510-520})^{-1} - (R_{560-570})^{-1}) \times R_{NIR}$, $\text{mCRI}_{RE} = ((R_{510-520})^{-1} - (R_{690-700})^{-1}) \times R_{NIR}$	Gitelson, Keydan, and Merzlyak 2006
mND_{680}	Quantify Chl content and sensitive to low content at leaf level.	$(R_{800} - R_{680})/(R_{800} + R_{680} - 2R_{445})$	Sims and Gamon 2002

mND$_{705}$	Quantify Chl content and sensitive to low content at leaf level; mND$_{705}$ performance better than mND$_{680}$.	$(R_{750} - R_{705})/(R_{750} + R_{705} - 2R_{445})$	Sims and Gamon 2002
mSR$_{705}$	Quantify Chl content and sensitive to low content at leaf level.	$(R_{750} - R_{445})/(R_{705} - R_{445})$	Sims and Gamon 2002
NPCI	Assess Cars/Chl ratio at leaf level.	$(R_{680} - R_{430})/(R_{680} + R_{430})$	Peñuelas et al. 1994
NPQI	Detect variation of Chl concentration and Cars/Chl ratio at a leaf level.	$(R_{415} - R_{435})/(R_{415} + R_{435})$	Barnes et al. 1992 Peñuelas, Filella et al. 1995
PBI	Retrieve leaf total Chl and N concentrations from satellite hyperspectral data.	R_{810}/R_{560}	Rama Rao et al. 2008
PRI	Estimate Car pigment contents in foliage.	$(R_{531} - R_{570})/(R_{531} + R_{570})$	Gamon et al. 1992
PSSR	Estimate Car pigment contents in foliage.	R_{800}/R_{500}	Blackburn 1998
RARS	Estimate Car pigment contents in foliage.	R_{760}/R_{500}	Chappelle et al. 1992
RGR	Estimate anthocyanin content with a green and a red band.	R_{Red}/R_{Green}	Gamon and Surfus 1999; Sims and Gomon 2002
SIPI	Estimate Car pigment content change in foliage; related to a ratio, Cars:Chls.	$(R_{800} - R_{445})/(R_{800} - R_{680})$	Peñuelas, Baret et al. 1995
TVI	Characterize the radiant energy absorbed by leaf pigments (Chls); note that the increase of Chls concentration also results in the decrease of the green reflectance.	$0.5[120(R_{750} - R_{550}) - 200(R_{670} - R_{550})]$	Broge and Leblanc 2000; Haboudane et al. 2004
Foliar Chemistry			
CAI	Cellulose and lignin absorption features, discriminates plant litter from soils.	$0.5(R_{2020} + R_{2220}) - R_{2100}$	Nagler et al. 2000
NDLI	Quantify variation of canopy lignin concentration in native shrub vegetation.	$[\log(1/R_{1754}) - \log(1/R_{1680})] / [\log(1/R_{1754}) + \log(1/R_{1680})]$	Serrano et al. 2002
NDNI	Quantify variation of canopy N concentration in native shrub vegetation.	$[\log(1/R_{1510}) - \log(1/R_{1680})] / [\log(1/R_{1510}) + \log(1/R_{1680})]$	Serrano et al. 2002

(Continued)

TABLE 5.2 (*Continued*)

Summary of 66 Spectral Indices Extracted from Hyperspectral Data, Collected from the Literature

Spectral Index	Characteristics and Functions	Definition	Reference
Water			
DSWI	Detect water-stressed crops at a canopy level.	$(R_{802} + R_{547})/(R_{1657} + R_{682})$	Galvão et al. 2005
LWVI-1	Estimate leaf water content, an NDWI variant.	$(R_{1094} - R_{893})/(R_{1094} + R_{893})$	Galvão et al. 2005
LWVI-2	Estimate leaf water content, an NDWI variant.	$(R_{1094} - R_{1205})/(R_{1094} + R_{1205})$	Galvão et al. 2005
MSI	Detect variation of leaf water content.	R_{1600}/R_{819}	Hunt and rock 1989; Ceccato et al. 2001
NDII	Detect variation of leaf water content.	$(R_{819} - R_{1600})/(R_{819} + R_{1600})$	Hardinsky et al. 1983
NDWI	Improve the accuracy in retrieving the vegetation water content at both leaf and canopy levels.	$(R_{860} - R_{1240})/(R_{860} + R_{1240})$	Datt et al. 2003; Gao 1996
$RATIO_{1200}$	Estimate relative water content <60% at leaf level.	$2 \times R_{1180-1220}/(R_{1090-1110} + R_{1265-1285})$	Pu, Ge et al. 2003
$RATIO_{975}$	Estimate relative water content <60% at leaf level.	$2 \times R_{960-990}/(R_{920-940} + R_{1090-1110})$	Pu, Ge et al. 2003
RVI_{hyp}	Quantify LAI and water content at canopy level.	R_{1088}/R_{1148}	Schlerf et al. 2005
SIWSI	Estimate leaf or canopy water stress, especially in the semiarid environment.	$(R_{860} - R_{1640})/(R_{860} + R_{1640})$	Fensholt and Sandholt 2003
SRWI	Detect vegetation water content at leaf or canopy level.	R_{860}/R_{1240}	Zarco-Tejada et al. 2003
WI	Quantify relative water content at leaf level.	R_{900}/R_{970}	Peñuelas et al. 1997
Stress			
Plant senescence reflectance index (PSRI)	Sensitive to theCar/Chl ratio and used as a quantitative measure of leaf senescence and fruit ripening.	$(R_{680} - R_{500})/R_{750}$	Merzlyak et al. 1999
RVSI	Assess vegetation community stress at canopy level.	$[(R_{712} + R_{752})/2] - R_{732}$	Merton and Huntington 1999

(NDII), normalized difference VI (NDVI), pigment-specific normalized difference (PSND), hyperspectral perpendicular VI (PVI_{hyp}), renormalized difference VI (RDVI), hyperspectral ratio VI (RVI_{hyp}), standard of LAIDI (sLAIDI), spectral polygon VI (SPVI), SR, and wide dynamic range VI (WDRVI). For example, Gong et al. and Weihs et al. used PVI_{hyp}, SR, NDVI, RDVI, and RVI_{hyp}, constructed from hyperspectral image data Hyperion and HyMap, to estimate forest LAI. He, Guo, and Wilmshurst and Darvishzadeh, Skidmore et al. (2008) estimated LAI of grassland ecosystems with VIs: RDVI, MCARI2, and NDVI. With LAIDI and sLAIDI VIs, Delalieux et al. determined LAI in orchards. And Li et al. used MTVI2 to map LAI over an agricultural area from CASI hyper- spectral image data.

Some VIs, including adjusted transformed soil-adjusted VI (ATSAVI), leaf water VI 1(LWVI-1), leaf water VI 2 (LWVI-2), NDVI, SR, triangular VI (TVI), and modified SR (mSR_{705}), can be used for identifying and mapping plant species and composition. For example, Galvão, Formaggio, and Tisot developed and used VIs, LWVI-1, LWVI-2, and NDVI to discriminate five sugarcane varieties in southern Brazil with EO-1 Hyperion data. Hestir et al. used mSR_{705} VI to map invasive species with airborne hyperspectral data (HyMap). Further, Lucas and Carter assessed vascular plant species richness on Horn Island, Mississippi, with various SR VIs constructed from HyMap hyper- spectral image data. For estimating biomass from hyperspectral data, some VIs, such as EVI, modified normalized difference (mND_{705}), mSR_{705}, NDVI, SR, and WDRVI, are very useful. For example, Hansena and Schjoerring and le Maire et al. used various narrowband NDVIs and SRs to estimate wheat crop and broadleaf forest biomass, respectively.

With hyperspectral data, many VIs were developed for estimating plant pigments, especially for Chls (Chl-a and Chl-b). They are blue green pigment index (BGI), blue red pigment index (BRI), Chl absorption ratio index (CARI), Chl index using green reflectance (Chl_{green}), Chl index using red edge reflectance ($Chl_{red\text{-}edge}$), modified SR of derivatives (DmSR), leaf Chl index (LCI), modified Chl absorption in reflectance index (MCARI), mND_{705}, mSR_{705}, normalized total pigment to Chl index (NPCI), normalized phaeophytinization index (NPQI), plant biochemical index (PBI), photochemical/physiological reflectance index (PRI), PSND, red edge vegetation stress index (RVSI), structural independent pigment index (SIPI), TVI, NDVI, and SR. The VIs specifically developed for estimating Cars contents at leaf level include Car reflectance index (CRI), double difference (DD), eucalyptus pigment indexes (EPIs), modified Car reflectance index (mCRI), PRI, pigment-specific SR (PSSR), ratio analysis of reflectance spectra (RARS), and SIPI. A few VIs were designed for estimating Anths contents in foliage. They are anthocyanin reflectance index (ARI), modified ARI (mARI), and red-green ratio (RGR). These VIs were developed from various hyperspectral data and have been applied for estimating plant pigments by researchers. For instance, Blackburn used various narrowband SR, PSND, and SIPI VIs to quantify Chls and Cars of *Pteridium aquilinum* grass at leaf and canopy scales. Gitelson et al. developed mCRI, ARI, and mARI VIs with in situ spectral measurements taken from tree leaves to estimate Chls, Cars, and Anths contents. Rama Rao et al. developed a new VI, named PBI, for improved estimation of plant biochemicals from spaceborne hyperspectral data. The VI PBI is an SR of reflectances at 810 and 560 nm. It has the potential to retrieve leaf total Chls and N concentrations of various crops and at different geographical locations. Hatfield et al. used PSND and PRI to determine the pigments of agricultural crops. A study by le Maire et al. estimated leaf Chls content of broadleaf forest with NDVI and SR VIs derived from in situ and Hyperion hyperspectral data. Chappelle, Kim, and McMurtrey recommended the use of R_{760}/R_{500} as a quantitative measure of Cars. Peñuelas, Baret, and Filella proposed the use of SIPI for estimating Cars. For Anths estimation, Gamon and Surfus used a ratio of red-green reflectances $R_{600–700}/R_{500–600}$, and Gitelson, Merzlyak, and Chivkunova, Gitelson, Keydan, and Merzlyak used an ARI and an mARI to estimate Anths content at the plant leaf level. However, Sims and Gamon concluded, "estimation of Cars and Anths contents remains more difficult than estimation of Chls content."

Many narrowband VIs were designed for estimating water content at the leaf and canopy levels. These VIs include disease water stress index (DSWI), LWVI-1, LWVI-2, moisture stress index (MSI), NDII, normalized difference water index (NDWI), PVI_{hyp}, 3-band ratio at 1200 nm ($RATIO_{1200}$), 3-band ratio at 975 nm ($RATIO_{975}$), RVI_{hyp}, RVSI, SWIR water stress index (SIWSI), SR water index (SRWI), and water index (WI). For example, Peñuelas et al. studied the reflectances of gerbera, pepper, bean plants, and wheat in the 950–970 nm region as an indicator of water status. Their results showed that the ratio of the reflectance at 970 nm, one of the water absorption bands, to the reflectance at 900 nm as the reference wavelength (R_{970}/R_{900} or WI) closely tracked changes in relative water content (RWC), leaf water potential, stomatal conductance, and cell wall elasticity. Cheng et al. and Clevers, Kooistra, and Schaepman used NDWI, WI, and SIWSI to estimate vegetation water content for different canopy scenarios with hyperspectral AVIRIS data. Colombo et al. estimated leaf and canopy water content in a poplar plantation using SRWI, NDII, and MSI derived from airborne hyperspectral image data. Pu, Ge et al. determined water status in coastal live oak leaves with $RATIO_{1200}$ and $RATIO_{975}$ indices derived from hyperspectral measurements.

A few VIs are designed for estimating nutrient constituents and concentrations of other biochemicals, such as lignin and cellulose. They are cellulose absorption index (CAI), normalized difference N index (NDNI), normalized difference lignin index (NDLI), NDVI, PBI, and SR. For example, Serrano, Peñuelas, and Ustin proposed NDNI and NDLI to assess N and lignin concentrations in chaparral vegetation using AVIRIS hyperspectral image data. Gong, Pu, and Heald and Hansena and Schjoerring used narrow- band NDVI and SR indices to assess nutrient constituent concentrations (N, P, and K) in a conifer species and N status in wheat crops from hyperspectral data. Further, Rama Rao et al. estimated leaf N concentration of cotton and rice crops with PBI derived from Hyperion hyperspectral data.

Analysis of Absorption Features and Spectral Position Variables

Analysis of spectral absorption features is one step further toward the recognition of some essential properties of a target of interest. Quantitative characterization of absorption features allows for abundance estimation from hyperspectral data. Spectral absorption features are caused by a combination of factors inside and outside the matter surface, including electronic processes, molecular vibrations, abundance of chemical constituents, granular size and physical structure, and surface roughness relative to electromagnetic wavelength. Figure 5.1 shows the major absorption and reflectance features for vegetation. In order to analyze the absorption features of a spectral reflectance curve, one needs to normalize the spectral curve so that only the spectral values inside the absorption features will be less than 1(100%). This can be done using a continuum-removal technique proposed by Clark and Roush. As shown in Figure 5.2, a continuum is defined for each spectral curve by finding the high points (local maxima) along the curve and fitting straight

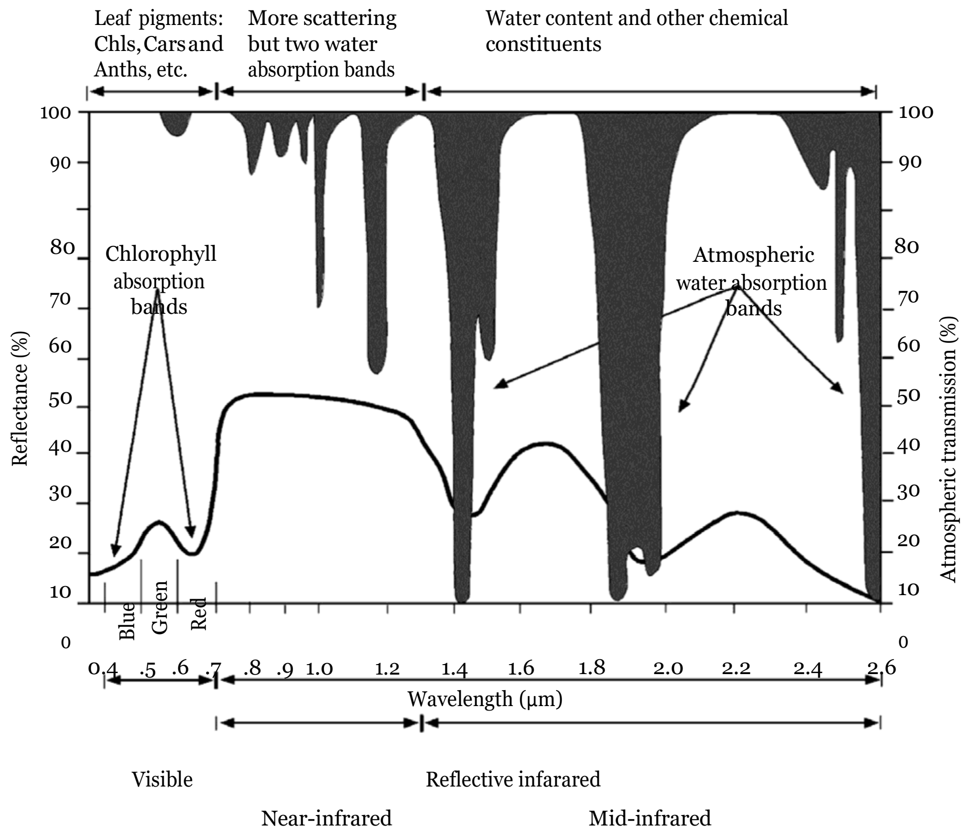

FIGURE 5.1

Major absorption features of vegetation. Leaves from different species may have different strengths of absorption.

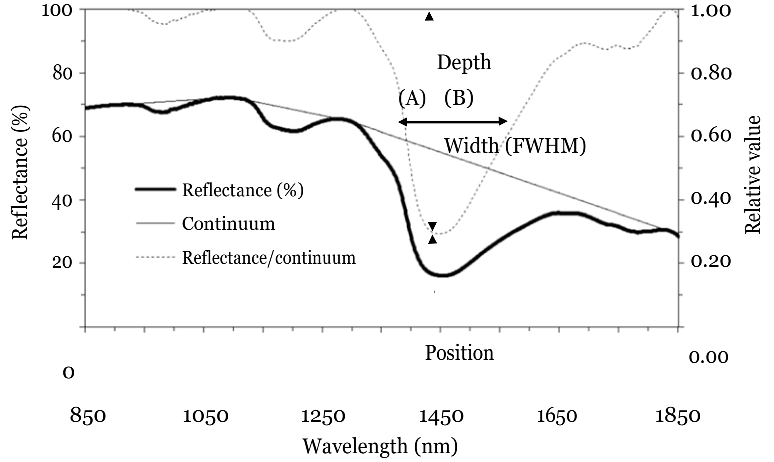

FIGURE 5.2

A part of the coastal live oak leaf spectrum adjusted by a continuum-removal technique (Data from Clark, R. N., and T. L. Roush. 1984. *J Geophys Res* 89:6329–40.) and the definitions of three absorption features. Depth measures the deepest absorption. Width measures full width half maximum (FWHM) absorption. Position marks the wavelength at the deepest absorption and areas (A or B) on each side of the deepest absorption are used for calculating asymmetry.

line segments between these points. This can be done either manually or automatically. The normalized curve is obtained by dividing the original spectral value at each band location with the value on the straight line segments at the corresponding wavelength location. Quantitative measures can be determined from each absorption peak after normalization of the raw spectral reflectance curve. An asymmetric term can also be defined by subtracting area A from area B. The quantitative measures shown in Figure 5.2 can be used to determine the abundances of certain compounds in a pixel. For example, Pu, Ge et al. explored the effectiveness of these absorption parameters in correlation with the leaf water content of oak trees at various stages of disease infection. Galvão, Formaggio, and Tisot successfully used some absorption features extracted with this technique and other spectral indices from EO-1 Hyperion data to discriminate the five sugarcane varieties in southeastern Brazil. Huber et al. also estimated foliar biochemistry (the concentrations of N and carbon, and the content of water) from hyperspectral HyMap data in mixed forest canopy using such a continuum-removal technique.

Some absorption features or spectral position variables can also be modeled. For example, the red edge of vegetation between 670 and 780 nm has been widely modeled by a number of researchers. Based on the spectral properties of the pigments, some researchers have used red edge optical parameters to estimate plant leaf and canopy Chls content and concentration. Guyot, Baret, and Jacquemond proposed a four- point interpolation method to find the wavelength position of the inflection point on the red edge position and the red well position. Other methods include polynomial fitting, Lagrangian interpolation, inverted Gaussian model fitting, and linear extrapolation techniques. The red edge optical parameters can be used for estimating Chls concentrations, nutrient constituent concentrations, leaf relative water content, and forest LAI. In addition, Pu, Foschi, and Gong proposed to extract 20 spectral variables (10 maximum-first derivatives plus 10 corresponding wavelength- position variables) from 10 slopes defined across a reflectance curve from 0.4 to 2.5 μm for estimating oak leaf relative water content. All these efforts can help extract absorption feature measures and other spectral features from original hyperspectral data for estimating vegetation parameters.

Hyperspectral Transformation

The principal component (PC) analysis (PCA) technique has been applied to reduce the data dimension and feature extraction from hyperspectral data for assessing leaf or canopy biophysical and biochemical parameters. With a covariance (or correlation) matrix calculated from vegetated pixels only, it is commonly believed that the eigenvalues and corresponding eigenvectors computed from the covariance (or correlation) matrix are able to enhance vegetation variation information in the first several PCs. Because the PCA does not always produce images that show steadily decreasing image quality with increasing component number, Green et al. developed one transform method called "maximum noise fraction" (MNF) transform to maximize the signal-to-noise ratio when choosing PCs with increasing component number. Then, several MNFs to maximize the signal-to-noise ratio are selected for further analysis of hyperspectral data, such as for determining endmember spectra for spectral mixture analysis and hyperspectral mosaic.

"Canonical discriminant analysis" (CDA) also is a dimension-reduction technique equivalent to canonical correlation analysis that can be used to determine the relation- ship between the quantitative variables and a set of dummy variables coded from the class variable in a low-dimensional discriminant space. Given a classification variable and several quantitative variables, CDA derives canonical variables, linear combinations of the quantitative variables that summarize between-class variation in much the same way that PCA summarizes most variation in the first several PCs. In other words, CDA involves human effort and knowledge derived from training samples, whereas PCA performs a relatively automatic data transformation and tries to concentrate the majority of data variance in the first several PCs. However, unlike PCA, CDA is only occasionally analyzed and tested as a data transformation technique by researchers in the remote-sensing community for dimensional reduction and feature extraction.

The wavelet transform (WT) is a relatively new signal-processing tool that provides a systematic means for analyzing signals at various scales or resolutions and shifts. In the past two decades, WT has been successfully applied to image processing, data compression, pattern recognition, image texture feature analysis, and feature extraction. Wavelets have proven to be quite powerful in these remote-sensing application areas. This is attributed to the facts that the WT can decompose a spectral signal into a series of shifted and scaled versions of the mother wavelet function, and that the local energy variation (represented as peaks and valleys) of a spectral signal in different bands at each scale can be detected automatically and provide some useful information for further analysis of hyperspectral data. With continuous WT (CWT), one can analyze both single-dimensional and multidimensional signals, such as hyperspectral image cubes, across a continuum of scales. With discrete WT (DWT), signals are analyzed over a discrete set of scales, typically dyadic ($2j, j = 1, 2, 3, \ldots$), and the transforms can be realized using a variety of fast algorithms and customized hardware. The WT can decompose signals over dilated (scaled) and translated (shifted) wavelets. There are many different types of mother wavelets and wavelet bases to be selected for use. In practice, researchers need to test most of the wavelet families to find the most useful wavelet family in a particular project. After a set of DWT coefficients for each level or scale of a pixel-based spectrum is calculated, the energy feature of the wavelet decomposition coefficients is computed at each scale for both approximation and details and is used to form an energy feature vector. This can become a feature extraction through a dimension reduction. With hyperspectral data of vegetation and the WT technique, several studies already demonstrate the benefits of wavelet analysis. For example, Pu and Gong used the mother wavelet function db3 in MATLAB® to transform Hyperion data (167 available bands in their analysis) for extracting features through a dimension reduction for mapping forest LAI and CC. By using the wavelet analysis method, Blackburn and Blackburn and Ferwerda retrieved plant pigments (Chls and Cars) concentration from leaf and canopy spectra, although further work is needed to refine this approach. Hsu and Tseng and Henry et al. used the wavelet analysis method (multiscale transform) to extract useful spectral features from hyperspectral data (AVIRIS and in situ spectral measurements) for plant/crop-type classification. They concluded that using spectral features extracted with the wavelet analysis method from hyperspectral data resulted in higher classification accuracy than using features with other methods (e.g., PCA and multiple VIs).

Spectral Unmixing Analysis

Unlike laboratory and in situ spectral reflectances, which are usually measured from "pure materials," a large portion of remotely sensed data is spectrally mixed. In order to identify various pure materials and to determine their spatial proportions from the remotely sensed data, the spectral mixing process has to be properly modeled. Once the spectral mixing process is modeled, the model can be inverted to derive the spatial proportions and spectral properties of pure materials. There are two types of spectral mixing: (1) linear spectral mixing and (2) nonlinear spectral mixing. Both linear and nonlinear spectral mixing models are simple tools used to describe spectral mixing processes. A real spectral mixing process could be complicated and can be more explicitly dealt with using radiative transfer (RT) models; also their solutions are often difficult to obtain. Linear spectral mixing model (LSM) and its inversion have been widely used since the late 1980s. An LSM has been extensively applied to extract the abundance of various components within mixed pixels. The nonlinear spectral mixture model can be found detailed in the works of Sasaki et al. and Zhang et al. In addition, an artificial neural network (ANN) algorithm has been tested to unmix mixed pixels into fractional abundances of endmembers in some studies.

In the spectral mixture analysis, a typical LSM at pixel (i, j) can be expressed as follows:

$$\mathbf{R}_{ij} = \mathbf{M}\mathbf{F}_{ij} + \boldsymbol{\varepsilon}_{ij} \tag{5.7}$$

where $\mathbf{R}_{ij}$ is a K-dimension reflectance (or digital number) vector, $\mathbf{F}_{ij}$ is an L-dimension fraction vector, $\mathbf{M}$ is a $K \times L$ endmember spectral matrix, and $\boldsymbol{\varepsilon}_{ij}$ is a K-dimension error vector representing residual error. The goal of spectral unmixing is to solve for $\mathbf{F}_{ij}$, with $\mathbf{R}_{ij}$ and $\mathbf{M}$ known. When the number of endmembers in pixel (i, j) are appropriately accounted for, $\mathbf{F}_{ij}$ should satisfy the following conditions:

$$\sum_{l=1}^{L} \mathbf{F}_l = 1, \text{ and } \mathbf{F}_l \geq 0 \tag{5.8}$$

It is well known that the inversion of Equation 5.7 (i.e., spectral unmixing) can be achieved with a least-squares solution (LSS) when $K > L$.

A feed-forward ANN algorithm is a nonlinear solution to the LSM, used for unmixing mixed pixels. The network training mechanism is an error-propagation algorithm. In a layered structure, the input to each node is the sum of the weighted outputs of the nodes in the prior layer, except for the nodes in the input layer, which are connected to the feature values. The nodes in the last layer output a vector that corresponds to similarities in each class, or fractions of endmembers within a mixed pixel. One layer between the input and output layers is usually sufficient for most learning purposes. The learning procedure is controlled by a learning rate and a momentum coefficient, which need to be specified empirically based on the results of a limited number of tests. Network training is done by repeatedly presenting training samples (pixels) with the known fractions of endmembers. Training is terminated when the network output meets a minimum error criterion or optimal test accuracy is achieved. The trained network can then be used to estimate the fraction of each endmember in a mixed pixel.

This simple mixing model (LSM) has an advantage in that it is relatively simple and provides a physically meaningful measure of abundance in mixed pixels. However, there are a number of limitations to the simple mixing concept: The endmembers used in LSM are the same for each pixel, regardless of whether the materials represented by the endmembers are present in the pixel; it fails to account for the fact that the spectral contrast between those materials is variable; the LSM cannot account for subtle spectral differences among materials efficiently; and the maximum number of components that an LSM can map is limited by the number of bands in the image data. Therefore, Roberts et al. introduced multiple endmember spectral mixture analysis (MESMA), a technique for identifying materials in a hyperspectral image using endmembers from a spectral library. The MESMA technique overcomes the limitations of the simple mixing model. Using the MESMA, the number of endmembers and their types are allowe to vary for each pixel in the image. The general MESMA procedure starts with a series of two-endmember candidate models, evaluates each model based on selection criteria and then, if required, constructs candidate models that incorporate more endmembers.

The key to successful spectral mixture analysis is the selection of appropriate endmembers. Determination of endmembers involves identifying the number of endmembers and extracting their corresponding spectral signatures. The pixel purity index (PPI), according to Boardman, can be combined with the use and interpretation of scatter plots of MNF to characterize the relative abundance of endmembers across a scene to help determine endmember spectra. The ability to detect different surface materials in the endmember analysis of remotely sensed data is a function of spectral contrast among endmembers, noise, and spectral resolution. Sufficient spectral information from hyperspectral data ensures the successful unmixing of mixed pixels. To select endmembers during the processing of MESMA, three selection criteria are fraction, root mean square error (RMSE), and the residuals of contiguous bands. The minimum RMSE model is assigned to each pixel, and it can be used to map materials and fractions within the image with the MESMA approach.

A number of researchers have applied LSM to hyperspectral data to estimate the abundance of general vegetation cover or specific vegetation species. A neural network (NN)–based nonlinear solution also was applied tohyperspectral data to estimate the abundance of specific vegetation species. Several researchers have applied the MESMA approach in a variety of environ- ments for vegetation mapping. For example, Roberts et al. used MESMA and AVIRIS hyperspectral image data to map vegetation species and land-cover types in south- ern California chaparral. Using AVIRIS image data and the MESMA approach, Li, Ustin, and Lay and Rosso, Ustin, and Hastings mapped coastal salt marsh vegetation in China and the marshland vegetation of San Francisco Bay, California, respectively. In addition, Fitzgerald et al. successfully mapped multiple shadow fractions in a cotton canopy with MESMA approach and hyperspectral imagery.

Hyperspectral Image Classification

Traditional multispectral classifiers can be used, but they may have a less than expected effect as they face difficulties caused by the high dimensionality of hyperspectral data and the high correlation of adjacent bands with a limited number of training samples. In order to overcome these problems, a feature extraction preprocessing before classification is necessary. Feature extraction schemes such as PCA (or its noise-adjusted version, MNF), Fisher's linear discriminant analysis (LDA), or CDA) have been applied in transforming and reducing the data dimension by maximizing the ordered variance of the whole data set or the ratio of between-class variance and within-class variance of the training samples. Jia and Richards proposed a segmented PC transformation (i.e., segmented PCA or segPCA) to reduce the computation cost by selecting subsets of the covariance matrix in a lower segmented dimension. Penalized discriminant analysis (PDA) was suggested to deal with the high correlation among the bands more efficiently by penalizing the high within-class variance and to improve the performance of LDA. Jia and Richards first segmented the whole spectral space into several sub- spaces using a spectral correlation matrix and then used the maximum likelihood classifier, called "simplified maximum likelihood classification," to classify an image scene. Jimenez and Landgrebe segmented and transformed the whole spectrum into several subspectra, estimated training statistics at the subspaces, and iteratively updated an orthogonal projection matrix until a minimum Bhattacharyya distance (BD) was obtained among the classes.

Fisher's LDA and CDA search for successive linear combinations of data to maximize the ratio of between-class variance and within-class variance of training samples in an expectation of spreading the means or the cluster centers of different classes as much as possible while keeping the within-class variation at a similar level for all classes. It is based on an assumption of reliable estimation of training statistics. Segmented LDA (segLDA) first divides the whole spectrum into subblocks, with each block containing a set of continuous highly correlated spectral bands.

Denote the dimension of the kth subblock as I_k, and $I_1 + \cdots + I_k + \cdots + I_K = I$. For each subblock of spectral bands, estimate the between-class covariance matrix and the within-class covariance matrix in a subspace that has a dimension equal to the number of bands in the subblock. Then, apply LDA to each subblock to generate new component images (features) with a number of $min(C-1, I_k)$, where C is the number of classes and k is the kth subblock. This projection is supposed to spread the means of the classes as much as possible. With the newly projected images for each subblock, we could either select the first few feature images from each subblock to generate a combined pool of new features that can be subsequently used for classification, or select more feature images less than $min(C-1, I_k)$ from the kth subblock for $k = 1, \ldots, K$ to form a new subspace. The LDA approach can be applied multiple times to reduce the data dimension in the search for an optimal set of orthogonal subspaces for use in final classification. The PDA introduces a penalty matrix Ω to the within-class covariance matrix to penalize and limit the effect that a band with high within-class variation may have in the case of LDA, while reserving the low within-class variation band. The function of the penalty matrix was geometrically interpreted by Yu et al. The matrix unequally smooths within-class variation for all the classes in the hyperspectral space. The realization of segmented PDA (segPDA) and segmented CDA (segCDA) is similar to that of segLDA in the sense that segmentation is done before applying PDA, except that PDA adds a penalty term to the estimation of the within-class covariance matrix. Similar to segPCA, segLDA, segCDA, and segPDA all save significant computation time.

Xu and Gong (2007) compared several feature extraction algorithms used for band reduction of Hyperion data. These include PCA, segPCA, LDA, segLDA, PDA, and segPDA. Feature reductions were all followed by classification of Hyperion images using a minimum distance (MD) classifier. With segPDA, segLDA, PDA, and LDA, similar accuracies were achieved, whereas the segPDA and segLDA newly proposed by Xu and Gong greatly improved computation efficiency. They also outperformed segPCA and PCA in classification accuracy due to the use of specific intra- and interclass covariance information. Similar to the conclusion drawn by Xu and Gong, Pu and Liu also concluded that segCDA outperformed segPCA and segmented stepwise discriminant analysis (SDA) when 13 tree species were discriminated using in situ hyperspectral data and segCDA. Based on the study by Pu and Liu, CDA or segCDA (under the condition of limited training samples) should be applied broadly in mapping forest-cover types, species identification, and other land use/land-cover classification practices with multi/ hyperspectral remote sensing data, because it is superior to PCA and SDA for selection of features that are used for image classification.

Support vector machines (SVMs) as a new type of classifiers have been successfully applied to the classification of hyperspectral remote-sensing data. Traditionally, classifiers first model the density of various classes and then find a separating surface for classification. However, the estimation of density for various classes with hyperspectral data suffers from the Hughes phenomenon: For a limited number of training samples, the classification rate decreases as the dimension increases. The SVM approach does not suffer from this limitation because it directly seeks a separating surface through an optimization procedure that finds so-called support vectors that form the boundaries of the classes. This is an interesting property of hyperspectral image processing because usually there is only a set of limited training samples available to define the separating surface for classification. Further, the properties of SVMs make them well suited to hyperspectral image classification since they can handle data efficiently in high dimensionality, deal with noisy samples in a robust way, and make use of only those most characteristic samples as support vectors in the construction of classification models. Melgani and Bruzzone provided a detailed introduction of SVMs for the classification of hyperspectral imagery. SVMs are considered to be kernel-based classifiers that are based on mapping data from the original input feature space to a kernel feature space of higher dimensionality and then solving a linear problem in that space. Camps-Valls and Bruzzone introduced several other kernel-based classifiers, including kernel Fisher discriminant analysis, regularized radial basis function NN, and a regularized boosting algorithm. They compared them with the SVMs and reported comparable accuracies in classifying the same agricultural AVIRIS scene as used by Melgani and Bruzzone.

The SVM approach can significantly improve classification accuracy with hyperspectral data. For example, Melgani and Bruzzone tested four SVM strategies for multiclass discrimination including the “one against all,” “one against one,” “binary hierarchical tree balanced branches,” and “binary hierarchical tree one against all” algorithms. They applied these algorithms to an AVIRIS image acquired over an agricultural area with nine classes and compared their performances with radial basis function NNs and K-nearest neighbor (K-NN) algorithms. They reported overall accuracies greater than 90% with an accuracy improvement of 7–12% over the NN and K-NN algorithms. Pal and Mather used a multiclass SVM for land-cover classification of Digital Airborne Imaging Spectrometer (DAIS) hyperspectral image data. Results showed that SVM outperforms maximum likelihood, univariate decision tree, and back propagation NN classifiers. For classification purposes with hyperspectral HyMap data, Camps-Valls et al. used SVMs for a six-class crop classification and analyzed their performance in terms of efficiency and robustness as compared to extensively used NNs and fuzzy methods. They concluded that SVMs yield better outcomes than NNs and fuzzy methods in terms of classification accuracy, simplicity, and robustness.

Empirical/Statistical Analysis Methods

Most researchers have employed statistical analysis methods to correlate biophysical or biochemical parameters with spectral reflectance, VIs, or derivative spectra in the visible, NIR, and SWIR wavelengths of hyperspectral data at leaf, canopy, or plant community level. Johnson, Hlavka, and Peterson determined predictive relationships for biochemical concentrations using regressions between the chemical composition of forest canopy and the AVIRIS reflectance. Using data from AVIRIS and a CASI, Matson et al. demonstrated that canopy biochemicals carried information about forest ecosystem processes and suggested that some of this chemical information might be estimated remotely using hyperspectral data collected by airborne sensors. They found that the first differences were in the range of 1525–1564 nm, which figured prominently in all N equations. After correlating VIs of R_{NIR}/R_{700} and R_{NIR}/R_{550} with Chl content, Gitelson and Merzlyak demonstrated that the indices for Chl assessment were important for two deciduous species, maple and chestnut. In spectral feature analysis associated with N, P, and K deficiencies in *Eucalyptus saligna* seedling leaves, Ponzoni and Goncalves proved that spectral reflectance can be better estimated using a combination of nutrient constituents (N, P, and K) as independent variables with the results from simple and multiple regression. Martin et al. determined forest species composition using high spectral resolution remote-sensing data with an approach that combined forest species–specific chemical characteristics and pre- viously derived relationships between hyperspectral data (AVIRIS) and foliar chemistry. They classified 11 forest-cover types, including pure and mixed stands of deciduous and conifer species, with an overall accuracy of 75%. With EO-1 Hyperion hyperspectral image data, Galvão, Formaggio, and Tisot successfully discriminated five sugarcane varieties in southeastern Brazil using a multiple discriminant analysis method that produced a classification accuracy of 87.5%. With multiple linear regression models, continuum- removal technique, and normalized HyMap spectra, Huber et al. estimated foliar concentrations of N and carbon, and content of water in a mixed forest canopy.

Partial least-squares regression (PLSR) is a technique that reduces the large number of measured collinear spectral variables to a few noncorrelated latent variables or PCs. The PCs represent the relevant structural information present in the measured reflectance spectra and are used to predict the dependent variables. The PLSR approach is different from PC regression (PCR) in the methods used in extracting factors (also called “components,” “latent vectors,” or “latent variables”). In short, PCR produces the weight (coefficient) matrix reflecting the covariance structure between the predictor variables, whereas PLSR produces the weight (coefficient) matrix reflecting the covariance structure between the predictor and response variables. In other words, PCR extracts factors to explain as much predictor sample variation as possible, whereas PLSR balances the two objectives of explaining both response variation and predictor variation as much as possible. Recently, there has been increasing interest in applying the PLSR approach to calibrate relationships between spectral variables, often derived from hyperspectral data and a set of bioparameters. For example, using spectral measurements taken from leaves and bioparameter data (Chl-a, Chl-b, Cars, Anths, water, N, P, and SLA) collected from 162 Australian tropical forest species, along with PLSR approach and canopy RT modeling, Asner and Martin concluded that a suite of leaf properties among tropical forest species can be estimated using full-range leaf spectra of fresh foliage collected in the field. Hansena and Schjoerring used two-band combinations in the normalized difference VIs constructed from in situ spectral measurements taken from wheat crop canopy and PLSR approach to estimate canopy green biomass and N status. They concluded that PLSR analysis may be a useful exploratory and predictive tool when applied to hyperspectral reflectance data analysis. The optimal number of PCs was determined by the guidelines described by Esbensen. The basic PLSR algorithm will not be introduced here, but further information on the PLSR model can be found in the work of Ehsani et al.

Although univariate and multiple regression analysis methods are relatively simple and their modeling results frequently have higher estimation accuracy, empirical or statistical relationships are often site, species, and sensor specific, and thus cannot be directly applied to other study areas since the plant canopy structure and sensors' viewing geometry may vary among different sites and species. Therefore, during the last two decades, physically based modeling approaches have attracted the attention of many researchers, who have retrieved biophysical and biochemical parameters by inversing various physically based models from simulated spectra or real imaging data.

Physically Based Modeling

The theoretical basis of physically based models consists of developing a leaf or canopy scattering and absorption model that involves biochemistry and biophysics. These models, including RT and geometric–optical (GO) models, consider the underlying physics and complexity of the leaf internal structure and therefore are robust and have the potential to replace statistically based approaches. In the context of the remote sensing of bioparameters, such models have been used in the forward mode to calculate leaf or canopy reflectance and transmittance and in the inversion mode to estimate leaf or canopy chemical and physical properties. For example, many researchers employ physically based models at leaf or canopy level to retrieve biochemical parameters, including leaf pigments from either simulated spectra or hyperspectral image data.

A number of RT models have been developed at leaf and canopy levels. They mostly simulate leaf reflectance and transmittance spectra between 0.4 and 2.50 μm. Among models focusing on leaf optical properties, the most important RT models may include the Propriétés Spectrales (PROSPECT) model, the leaf incorporating biochemistry exhibiting reflectance and transmittance yields (LIBERTY) model, and the leaf experimental absorptivity feasibility model. Among those focusing on canopy optical properties, the most popular RT models are the scattering by arbitrary inclined leaves model and its improved versions that have been adapted to account for some heterogeneity within the vegetation canopy, for example, GeoSAIL, 2M-SAIL, and 4SAIL2. The other important canopy reflectance models include fast canopy reflectance, the new advanced discrete model, the Markov chain canopy reflectance model adapted for row crops, and the four models used for simulating discontinuous forest canopies, including discrete anisotropic RT, spreading of photons for radiation interception, forest light interaction model, and three-dimensional forest light interaction. In addition, during the last two decades, researchers have developed some leaf-canopy-coupled models, including PROSAIL, LEAFMOD +CANMOD, LIBERTY+FLIGHT, and LIBERTY+SAIL. Among the RT models, based on the literature searched and analyzed by Jacquemoud et al., the most popular and important RT models on leaf, canopy, and leaf-canopy-coupled optical properties are PROSPECT, SAIL, and PROSAIL, as well as their modified versions.

The PROSPECT models, including the latest versions PROSPECT-4 and -5, can provide specific absorption and scattering coefficients of leaf components. The model is widely used and well validated. The SAIL model is a four- stream RT model developed by Verhoef. It was later modified by Kuusk to take the hot spot feature into account. Linking the two models into PROSAIL allowed description of both the spectral and directional variation of canopy reflectance as a function of leaf biochemistry (mainly Chls, water, and dry matter contents) and canopy architecture. The coupled leaf-canopy and other RT models are used to understand the way in which leaf reflectance properties are influenced by the larger number of controlling factors at canopy scale. Coupled models have enabled the development and refinement of spectral indices that are insensitive to factors such as canopy structure, illumination geometry, and soil/litter reflectance. Such approaches have also been used in defining predictive relationships that have been applied to hyperspectral imagery to generate maps of Chl.

The GO models belong to one type of RT models developed to capture the variation of remote sensing signals on the Earth’s surface with illumination and observation angles. Since GO models emphasize the effect of canopy architecture, they are very effective in capturing the angular distribution pattern of the reflected radiance, and are thus used widely in remote-sensing applications as aforementioned RT models. There are a lot of different types of GO models. For example, a model developed by Li and Strahler described the vegetation canopy using opaque geometric shapes (cones or cylinders), which cast shadows on the ground. Consequently, crown transparency is assumed to be zero. These GO models are mainly used to describe (sparse) forests or shrublands, where shadowing plays an important role.

Physically based models must be inverted to retrieve vegetation characteristics from the observed reflectance data. So far, different inversion techniques for physically based models mainly include iterative optimization methods, lookup table (LUT) approaches, and ANNs. In the iterative optimization approach, a stable and optimum inversion is not guaranteed. Moreover, the traditional iterative method is time-consuming and often requires a simplification of the models when processing large datasets. This may result in a decrease of the inversion accuracy and makes the retrieval of biophysical and biochemical variables unfeasible for large geographic areas. Methods employing LUTs can partially overcome this drawback. They operate using a database of simulated canopy reflectance variables in structural and radiometric properties. However, LUT creation can be complicated and requires an extensive set of reliable field measurements. The ANN technique, proposed in the forward and inverse modeling of RT models for retrieving bioparameters, is expected to reduce such complexity of inversion. For proper training (ANN) and representation (LUT), the techniques basically rely on a large database of simulated canopy reflectance spectra to achieve a high degree of accuracy. This increases the computational time for identifying the most appropriate LUT entry and the time required for training the ANN.

Summary and Future Directions

Hyperspectral remote sensing, or imaging spectroscopy, is a cutting-edge technology that can be utilized in ecological studies for extracting and assessing vegetation characterization. In this chapter, the spectral characteristics, properties, and/or responses of a set of plant biophysical and biochemical parameters were reviewed. These bioparameters mainly include typical biophysical parameters (LAI, SLA, CC, species/composition, biomass, NPP, and fPAR) and biochemical parameters (plant pigments such as Chl-a and Chl-b, Cars, and Anths, plant nutrients such as N, P, and K, leaf or canopy water content, and other chemicals such as lignin and cellulose; and protein concentration). To extract and assess typical bioparameters from various hyperspectral data, including laboratory and in situ hyperspectral measurements, spectra synthesized and/or simulated from physically based models, and airborne and spaceborne hyperspectral image data, relatively speaking, a wide range of analysis techniques and approaches that have already been developed and demonstrated are extensively reviewed in this chapter. The spectral analysis techniques cover spectral derivative analysis, spectral matching, spectral index analysis, spectral absorption features and spectral position variables, hyperspectral transformation, spectral unmixing analysis, and hyperspectral classifications; and the two general categories of analysis methods include empirical/statistical methods and physically based models. Advantages and disadvantages, or merits and drawbacks, for some specific analysis techniques and approaches were also discussed here. Data from imaging spectroscopy have repeatedly been shown to produce accurate estimates of many biochemical parameters and physical characteristics related to key ecological processes. Imaging spectroscopy is the only technology available to measure many important environmental properties over large regions, particularly canopy water content, dry plant residues, and soil biochemical properties.

In the future, the richness of information available in the continuous spectral coverage afforded by both airborne and spaceborne imaging spectrometers will make it possible to address questions regarding vegetation bioparameters more correctly and accurately. Since hyperspectral data can provide richer and more delicate spectral information than multispectral data, spectral unmixing and automatic target detection remain important information extraction tasks in hyperspectral data analysis, and the use of PCA, mathematical programming, and factor analysis need to be further assessed in solving the linear mixing problem. Inversion of physically based RT models with hyperspectral data assisted by analysis of multiangular data will be useful in solving nonlinear spectral mixing problems because the angular data can be used to retrieve the structural information of vegetation. When using various spectral VIs to estimate different bioparameters, the use of optimized VIs should be considered because there are many potential narrow bands ready to be used for developing various VIs from hyperspectral data. Experience has proven that with some optimized VIs for estimating some bioparameters, the estimation accuracy can be significantly increased. When attempting to identify a robust, generic solution, there is currently only limited evidence available with which one can rank the performance of the range of existing hyperspectral analysis approaches in quantifying plant bioparameters. Therefore, it is necessary to conduct intercomparison of hyperspectral approaches across a large number of bioparameters using a large number of different analysis techniques. A sensitivity study is needed to determine the set of variables that can be retrieved with a reasonable accuracy for available imaging spectroscopy systems. Finally, although many analysis techniques have been developed and are available in some applications for estimating biochemicals from hyperspectral data at the leaf scale, in order to exploit the opportunities offered by imaging spectrometry for synoptic, consistent, and spatially continuous information, it is important to develop suitable methods that can also derive estimates of foliar biochemical concentrations from canopy-scale reflectance spectra. For this case, several strategies are available for the analysis of canopy spectra. This is a scaling issue, a problem encountered frequently in ecological studies.

Chapter 2

Object Based Image Analysis for Vegetation Mapping and Monitoring

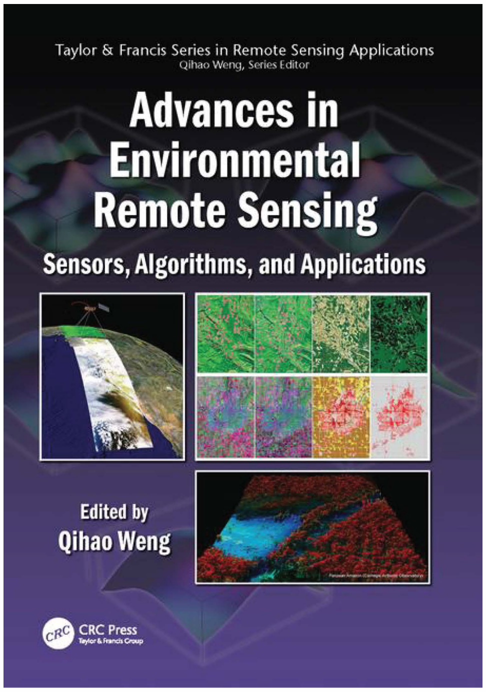

Advances in Environmental Remote Sensing: Sensors, Algorithms, and Applications

By Qihao Weng

© 2011 Taylor & Francis Group. All rights reserved.

To purchase a copy, click here.

Object-Based Image Analysis for Remotely Sensed Vegetation Mapping

The objective of OBIA is to develop and apply theory, methods, and tools for replicating and improving human interpretation of remotely sensed image data in an automated manner. OBIA consists of image segmentation, that is, clustering of pixels into homogenous objects, and subsequent classification or labeling of the objects, and modelling based on the characteristics of objects.

Object-Based Image Analysis

Having identified an increasing dissatisfaction with pixel-by-pixel image analysis, Blaschke and Strobl raised the provocative question "What's wrong with pixels?" Although this critique was not new, they observed a hype in applications "beyond pixels." A common denominator of these applications was, and still is, that they are built on image segmentation, that is, the partitioning of an image into meaningful geographically based objects. Image segmentation is not at all a new concept; it has its roots in industrial image processing and was not used extensively in geospatial applications during the 1980s and 1990s.

It is widely agreed that OBIA builds on older segmentation, edge-detection, feature extraction, and classification concepts that have been used in remote sensing image analysis for decades. Its emergence has nevertheless provided a bridge between the spatial concepts applied in multiscale landscape analysis, geographic information systems (GISs), and the synergy between image-objects and their radiometric characteristics and analyses in Earth observation satellite data.

Uses for segmentation methods outside remote sensing are legion. Within remote sensing applications, segmentation algorithms are numerous, and the number has been rapidly increasing over the past few years. Image segmentation from an algorithmic perspective is generally divided into four categories: (1) point based, (2) edge based, (3) region based, and (4) combined (for technical details of segmentation techniques, readers are referred to the study by Pal and Pal). As known to most readers, image segmentation is not a remote sensing–specific concept. Rather, many algorithms originate from industrial image processing. Blaschke, Burnett, and Pekkarinen specifically reviewed various segmentation algorithms for remote sensing applications. Segmentation provides the building blocks of OBIA. Segments are regions that are generated by one or more criteria of homogeneity in one or more dimensions (of a feature space), respectively. Thus, segments have additional spectral information compared to single pixels (e.g., mean values per band, median values, minimum and maximum values, mean ratios, variance); but of even greater advantage than the diversification of spectral value descriptions of objects is the additional spatial information for objects. It has been frequently claimed that this spatial dimension (distances, neighborhood, topologies, etc.) is crucial to OBIA methods, and that this is a major reason for the marked increase in the use of segmentation-based methods in recent times compared to the use of image segmentation in remote sensing during the 1980s and 1990s. It is this additional information and the reduction of feature reflectance variation at the object level that makes object-based feature extraction and conversion of image data sets into thematic map products so unique.

Object-Based Image Analysis and Increasing Spatial Resolution

The OBIA approach is tied in with high spatial resolution situations. In an image, such a situation may occur if the pixels are significantly smaller than the objects under consideration. Only then is regionalization of the pixels into groups of the pixels and finally objects useful and needed. In a high spatial resolution image, the specific advantages of the OBIA approach can be deployed, although regionalization approaches have also been applied to other situations, for example, to Landsat images. Recent studies have also utilized OBIA methods for medium or coarse spatial resolution data.

A central task of image segmentation is the production of a set of nonoverlapping segments (polygons). Before performing OBIA, this step is separated from the classification process. The problem, though, is scale. Scale is a “window of perception”, and we typically end up with several scales in imagery, if the spatial resolution is finer than the size of the objects of interest (Figure 10.1). A segmentation algorithm is used with the expectation that it will divide the image into relatively homogeneous and semantically significant groups of pixels. Burnett and Blaschke called these groups “object candidates,” which must be recognized by further processing steps and must be transformed into meaningful objects. It is well known that semantically significant regions are found in an image at different spatial scales of analysis, and OBIA is inextricably linked to multiscale analysis concepts, even if single levels are targeted for specific applications. Burnett and Blaschke called this OBIA concept “multiscale segmentation/object relationship modeling” (MSS/ORM). Lang and Langanke developed an iterative one-level representation (OLR), and Tiede, Lang, and Hoffmann applied the OLR concept convincingly to airborne lidar data for tree crown segmentation. Weinke, Lang, and Preiner empirically applied and evaluated both these OBIA concepts, and found pros and cons for each approach. For high spatial resolution image data (pixels <5 m), we can discriminate fields or forest stands at coarse scales, whereas at finer spatial scales, we can discriminate individual trees or plants (Figure 10.1). Parameters and thresholds in a typical single-scale segmentation algorithm must therefore be tuned to the correct scale for analysis. It is, however, often not possible

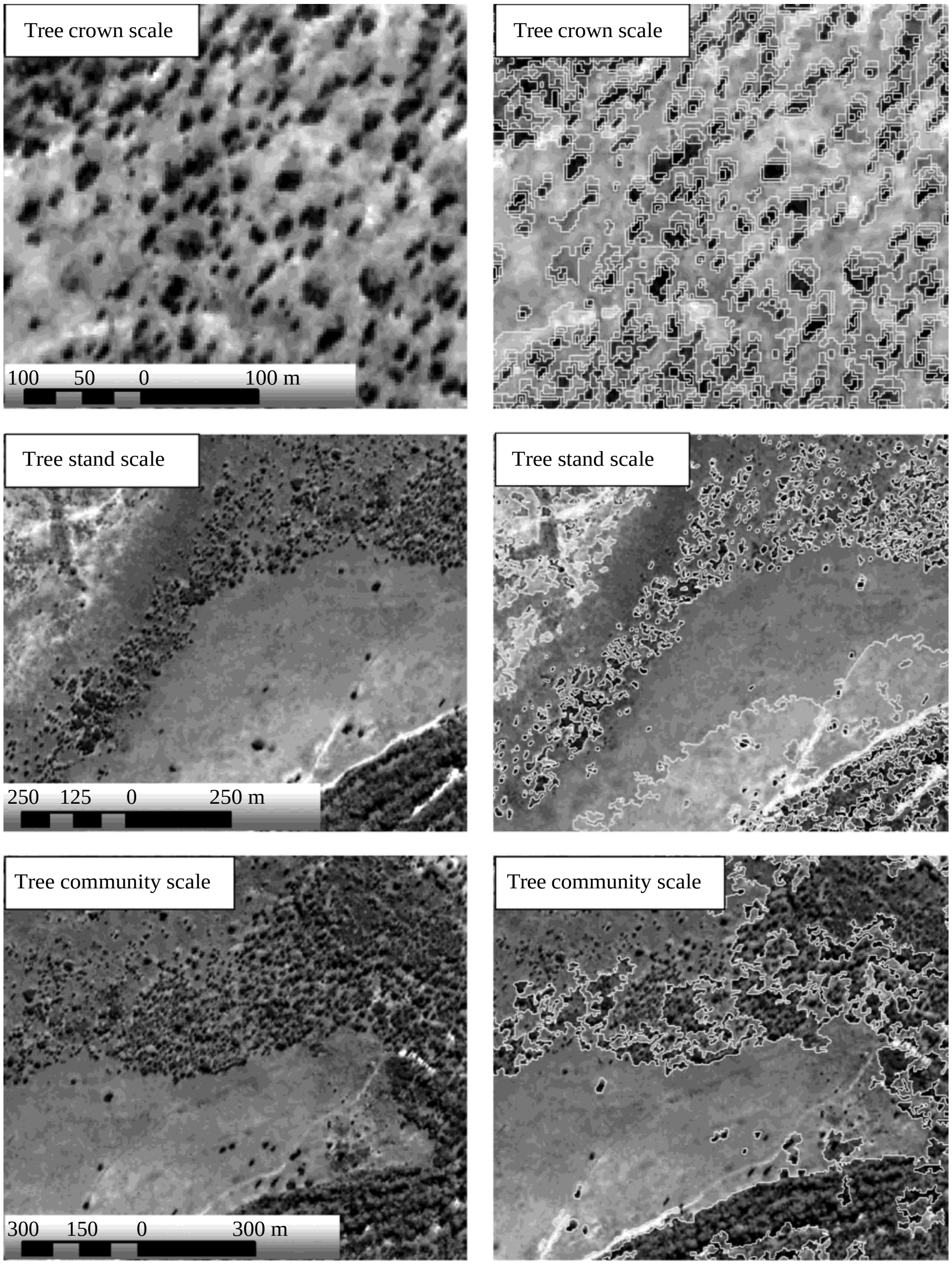

FIGURE 10.1

(See color insert following page 426.) Different spatial scales of observations in high spatial resolution QuickBird image data shown as a false-color composite. The three spatial scales show individual tree crowns and stands and associated feature segmentation within an Australian tropical savanna landscape as well as a tree community segmentation level showing riparian vegetation, savanna woodlands, and rangelands. This figure illustrates the multiscale concept by creating multiple scales of segmentation through successive grouping of image pixels into homogeneous image objects, providing a more intuitive and hierarchical partitioning of the image results, which cannot effectively be achieved in per-pixel approaches.

to determine the correct spatial scale of analysis in advance, as different kinds of images require different scales of analysis. Further, significant objects may appear at different spatial scales of analysis in the same image.

It should be clearly stated that much of the work referred to as OBIA originated around the software known as "eCognition". Further, only few "early" OBIA developers used the term "object based." Some authors used "object oriented", and some of these later switched to object based (with or without a hyphen), whereas some authors still use the term object oriented. It has so far been assumed that most authors prefer to use the term "based" since "oriented" may be too closely related to the object-oriented programming paradigm. Interestingly, there is not much critique on OBIA. In order to avoid potential flaws or too much optimism in this chapter, we performed a systematic search in the ISI Web of Knowledge and by using Google Scholar. Although hardly any critique was found, Blaschke identified a "'technopositivistic' tendency" in the early OBIA literature. The only article we found that attests a poor performance in a comparison study is a recent publication by Mas, Gao, and Pacheco. These authors analyzed the sensitivities of 85 landscape metrics to different classification methods and parameters for a Landsat image. Images classified based on pixel-based methods were smoothed using different methods (majority fitering, sieving, and clumping). Not surprisingly, for the spatial resolution of Landsat, this study found a poor performance of the OBIA method.

The idea of incorporating contextual information in the classification of remote sensing images can be traced back to the 1970s, although the importance of incorporating texture increases with increasing spatial resolution. What might have been considered a relatively homogeneous forest patch using Landsat imagery may be differentiated further to include structural aspects and density or biomass estimations using QuickBird imagery. With increasing spatial resolution comes the ability to map in more detail vegetation cover, forest structure, forest function, species composition, crown closure, stand height, stem density, vegetation age and volume, and other structural biophysical parameters.

Remote Sensing of Vegetation

The mapping and monitoring of vegetation conditions has been one of the most important objectives of remote sensing since the advent of remote sensing technology. Aerial photography was the sole source of information for vegetation mapping prior to 1972, when the first Landsat satellite was launched. The map- ping and monitoring of vegetation properties has been revolutionized by satellite remote sensing and multispectral imaging systems, which became commercially available during the 1970s. The number of methods used in image analysis and classification is legion. These methods may be grouped roughly into an investigation of vegetation classes and ecosystems with a focus on classification and delineation of extents of units classified as homogeneous concerning a given property, and biophysical parameter studies. For example, Wulder summarized some potential image processing methods that may be useful for the estimation of forest structural biomass estimation parameters. Treitz and Howarth reviewed hyperspectral remote sensing for biophysical para- meter estimation in the forest ecosystem. Asner, Hicke, and Lobell summarized the per-pixel analysis of forest structure using vegetation indices, spectral mixture analysis, and canopy-reflectance modeling. Regarding remote sensing applications, we may summarize that in addition to the experimental, hypothetical, and case study styles of investigations, we witness more and more the use of remote sensing within vegetation studies with increasing modes of operational usage. Vegetation mapping and monitoring has benefited significantly from the more readily available high spatial resolution image data, which have proven essential for vegetation and forest inventories at local to regional spatial scales. Higher spatial resolution may not necessarily result in improved mapping accuracies, as the accuracy also depends on the size of the features to be mapped. Although increased spatial resolution pro- vides opportunities for detecting small features and for mapping objects of interest in great detail, it also creates a variety of challenges in image analysis due to the variability of reflectance values within features of interest, for example, sunlit and shaded parts within one tree crown. The suitability of high spatial resolution image data for detailed vegetation mapping and monitoring in various environments is supported by the ability to scale-up mapping results derived at high spatial resolutions.

Most optical sensors are only capable of providing detailed information on the horizontal distribution and not the vertical distribution of woody vegetation and forests. In many areas of the world, active microwave sensing is the only operational option. Radar data are routinely used for acquiring remotely sensed data within given time frameworks because radar systems can collect Earth feature data irrespective of weather and light conditions. Due to this unique feature of radar data compared with optical sensor data, radar data have been used extensively in many fields, including forest-cover identification and mapping, discrimination of forest compartments and forest types, and estimation of forest stand parameters. A large number of research papers have proven the potential of radar data for ecological applications, including aboveground biomass estimation.

Airborne lidar sensors derive information on the elevation and reflectance of terrain and vegetation from a pulse or continuous-wave laser fired from an airborne transmitter, for which the transmitter's position is precisely and accurately measured. Processing of the reflected lidar signal provides an accurate measure of the distance between the transmitter and the reflecting surfaces based on the time of travel of the pulse and the position of the sensor. Since 2004, full-waveform lidar has become commercially available, allowing the complete waveform of the backscattered signal echo to be recorded. Both discrete-return and full-waveform lidar data can provide detailed information on the heights of canopy and understory surfaces with vertical and horizontal accuracies within a few centimeters. There are several published studies that suggest lidar data can be accurately employed for mapping and monitoring vegetation condition. Some of them have focused on the detection of individual tree crowns and the estimation of tree heights, crown dimensions, and vertical structure.

With the improvement of analysis techniques and OBIA software capacity along with the increasing amount of commercially available high spatial resolution image and lidar data, mapping capabilities are expected to grow rapidly in the future in terms of both accuracy and the amount of biophysical vegetation properties that can be successfully mapped. A number of remotely sensed data studies of vegetation have used OBIA.

State-of-the-Art Object-Based Image Analysis of Vegetation

In general, the number of OBIA publications is growing rapidly as is—more specifically—the utilization of OBIA for vegetation analysis and classification. Over the last few years, the number of empirical studies published in peer-reviewed journals reflects the improvements that OBIA offers over per-pixel analyses. Whereas per-pixel image analysis takes into account only spectral reflectance and texture calculated through the use of moving square windows, OBIA includes information on feature shape, context, neighborhood, and multiple spatial scales.

Vegetation Inventory and Classification

Yu et al. carried out a comprehensive vegetation inventory for protected seashore areas in northern California using high spatial resolution airborne image data and ancillary topographic data, and found object-based approaches more suitable than pixel-based approaches for vegetation mapping, as they overcame the problem of the salt-and-pepper effects found in pixel-based classification. Dorren, Maier, and Seijmonsbergen favored an OBIA approach rather than a pixel-based analysis to discriminate broad- scale forest-cover types from Landsat image and digital elevation model (DEM) data of a mountainous area in Austria. Yan et al. compared per-pixel and OBIA classifications for land-cover mapping in a coal fire area in Inner Mongolia, and found the differences in accuracy, expressed in terms of proportions of correctly allocated pixels, to be statistically significant. They concluded that the thematic mapping result using an OBIA approach gave a much higher accuracy than that obtained using the per-pixel approach.

Change Detection

Im, Jensen, and Tullis compared three different change detection techniques, based on object/neighborhood correlation, image analysis, and image segmentation, with two different per-pixel approaches, and found that object-based change classifications were superior (kappa up to 90%) compared to the other change detection results (kappa from 80% to 85%). Johansen et al. compared QuickBird-based change detection maps of different vegetation types derived from object-based and per-pixel inputs used in three change detection techniques (postclassification comparison, image differencing, and tasseled cap transformation) and found the object-based inputs to provide more accurate change detection results in all cases. Desclée, Bogaert, and Defourny proved the effectiveness of object-based change detection by detecting forestland-cover changes in deciduous and coniferous stands (>90% detection accuracy) from three System Pour l'Observation de la Terre (SPOT) images covering an 1800-km^2 study area in east Belgium over a 10-year period. Duveiller et al. investigated land-cover change by combining a systematic regional sampling scheme based on high spatial resolution imagery with object-based, unsupervised, classification techniques for a multidate segmentation, to obtain objects with similar land-cover change trajectories, which were then classified by unsupervised procedures. This approach was applied to the Congo River basin to accurately estimate deforestation at regional, national, and landscape levels. Krause et al. integrated Landsat and ASTER data, aerial photographs, and point data obtained by fieldwork. They assessed temporal–spatial changes on a mangrove peninsula in northern Brazil and the adjacent rural socioeconomic impact area, as well as the nature of the mangrove structure.

Structural change was analyzed, and the authors were able to differentiate between strong and weak patterns in the mangrove ecosystem, suggesting different management measures and monitoring at hierarchical scales. For mangroves on the Caribbean coast of Panama, Wang, Sousa, and Gong were able to enhance spectral separability among mangrove species by using objects as the basic spatial units, as opposed to pixels. Another example of an efficient OBIA-based analysis of a mangrove ecosystem is described by Conchedda, Durieux and Mayaux.

High Spatial Resolution Optical Data

Chubey, Franklin, and Wulder used OBIA to derive forest inventory parameters from IKONOS image data of a 77-km^2 study area in Alberta, Canada, and achieved the best relationships between field- and image-derived discrete land-cover types, species composition, and crown closure. Radoux and Defourny used high spatial resolution satellite images and OBIA methods to produce large-scale maps and quantitative information about the accuracy and precision of delineated boundaries for forest management using IKONOS and SPOT-5 image data. They found that tree shade and the interaction of stand patterns and sensor viewing angles produced a positive bias along forest/nonforest boundaries. For a highly fragmented forest landscape on southern Vancouver Island, Canada, Hay et al. proved how segments corresponded cognitively to individual tree crowns, ranging up to forest stands, using segmentation, object-specific analysis, and object-specific upscaling. Gergel et al. distinguished forest structural classes in riparian forests in British Columbia, Canada, for riparian restoration planning using QuickBird image data, and achieved accuracies ranging from 70% to 90% for most classes. Bunting and Lucas delineated tree crowns using seed identification and a region-growing algorithm within mixed-species forests of complex structure in central-east Queensland, Australia, based on 1-m airborne Compact Airborne Spectrographic Imager (CASI) hyperspectral data, and achieved mapping accuracies of greater than 70%. Mallinis et al. performed a multiscale, object-based analysis of a QuickBird satellite image to delineate forest vegetation polygons in a natural forest in northern Greece and found the inclusion of texture important; they also found that the use of classification trees yielded better results than the nearest-neighbor algorithm. Johansen et al. mapped the vegetation structure of Vancouver Island and discriminated structural stages in vegetation for riparian and adjacent forested ecosystems, using various texture parameters for a QuickBird image including co-occurrence contrast, dissimilarity, and homogeneity texture measures. An OBIA classification resulted in a very detailed map of vegetation structural classes, with an overall accuracy of 79%.

Light Detection and Ranging Data

Due to the high spatial resolution of lidar data, OBIA is increasingly used for both urban applications and delineating artificial objects, as well as for natural or near-natural objects. For instance, Xie, Roberts, and Johnson used an object-based geographic image retrieval approach for detecting invasive, exotic Australian pine in southern Florida using high spatial resolution orthophotos and lidar data. A moderate retrieval performance was achieved, with the lidar data proving to be most useful. Maier, Tiede, and Dorren incorporated very detailed information from lidar-derived canopy surface models and found that single and multilayered stands could be correctly distinguished in 82% of the sample plots. Also, stands with many small gaps and few but large gaps could be discriminated. Pascual et al. presented a two-stage approach for characterizing the structure of *Pinus sylvestris* stands in forests of central Spain. Building on the delineation of forest stands and a digital canopy height model derived from lidar data, they investigated forest structure types.

Incorporating Nonspectral Information

Weiers et al., Bock et al., Lathrop, Montesano, and Haag, and Diaz-Varela et al. demonstrated the usefulness of OBIA methods for habitat mapping tasks. Whereas Weiers et al. and Bock et al. used time-series analysis of Landsat Thematic Mapper (TM)/Enhanced TM (ETM+) image data for parts of northern Germany, Lathrop, Montesano, and Haag assessed sea grass on New Jersey's Atlantic coast using high spatial resolution airborne image data. Diaz-Varela et al. mapped highly heterogeneous landscapes of northern Spain from Landsat TM image data. Wiseman, Kort, and Walker successfully identified and quantified 93 out of 97 shelterbelts across the Canadian Prairie provinces using multispectral reflectance, shape, texture, and other relational properties in comparison with 1:40,000 scale orthophoto interpretation. Spectral reflectance, variance, and shape parameters were combined to differentiate speicies compositions for six shelterbelts. Addink, de Jong, and Pebesma demonstrated with airborne hyperspectral image data, in a very detailed study with 243 field plots, that the accuracy of vegetation parameters, aboveground biomass, and leaf area index (LAI) in southern France was higher for object-based analysis than for per-pixel analysis and that object size affects prediction accuracy. Stow et al. could differentiate changes in "true shrubs" and "subshrubs" within coastal sage scrub vegetation communities in California with an overall accuracy of 83% using high spatial resolution airborne image data, and they proved that patterns of shrub distribution were more related to anthropo- genic disturbance than to a long drought. Su et al. used OBIA methods to improve texture analysis based on both segmented image objects and moving windows across a QuickBird image scene, and co-occurrence matrix (gray-level co-occurrence matrix [GLCM]) textural features (homogeneity, contrast, angular second moment, and entropy) were calculated. Single additional features, such as Moran's I, were able to improve the user's and producer's accuracies by up to 16% for shrub- and grasslands. A comparison of results between spectral and textural–spatial information indicated that textural and spatial information can be used to improve the object-based classification of vegetation in urban areas using high spatial resolution imagery. Luscier et al. precisely evaluated an OBIA method based on digital photographs of vegetation to objectively quantify the percentage ground cover of grasses, forbs, shrubs, litter, and bare ground within 90 plots of 2 × 2 m. The observed differences between true cover and OBIA results ranged from 1% to 4% for each category. Ivits et al. analyzed landscape patterns for 96 sampling plots in Switzerland, based on object-derived patch indices for land-use intensities ranging from old-growth forests to intensive agricultural landscapes. Landscape patterns could be quantified on the basis of merged Landsat ETM–Indian Remote Sensing (IRS), QuickBird, and aerial photographic data. Gitas, Mitri, and Ventura mapped burned areas on the Spanish Mediterranean coast from National Oceanic and Atmospheric Administration (NOAA) Advanced Very High Resolution Radiometer (AVHRR) image data using object-based classification and achieved 90% spatial agreement with a digital fire perimeter map. These are just some examples of an increasing body of peer-reviewed literature on OBIA. For the sake of completeness, we should mention that OBIA methods include ways to incorporate various kinds of auxiliary information such as elevation, cadastre, bioclimate data, soil information, road networks, and transportation networks, to name just a few. In information-rich societies, we may regard remote sensing as only one out of many sources of information. Within spatial data infrastructures (SDIs), many examples exist that prove the potential for joint remote sensing/GIS applications. This is one of the basic ideas of the theoretical framework described by Burnett and Blaschke, briefly outlined in Section 10.4.

Case Studies of Object-Based Image Analysis for Mapping Vegetation

To demonstrate how OBIA can be used to deliver environmental management–ready vegetation information, two case studies involving innovative approaches are presented in this section. The two case studies focus on automating the mapping process for vegetation feature extraction, integrating field and image data, and mapping small features, that is, individual tree crowns, over large spatial extents.

Case Study 1: Mapping Plant Projective Cover within Riparian Zones Using Object-Based Image Analysis and Light Detection and Ranging Data

The first case study focusing on the mapping of riparian plant projective cover (PPC) from LiDAR data using OBIA will first provide an introduction on riparian zone and PPC mapping and research objective. Subsequent sections will present the methods used and the OBIA results of riparian zone extent and PPC mapping.

Introduction

Riparian zones, or areas bordering streams, are found along rivers and creeks, and extend outward to the limits of historic flooding. Plant project cover (PPC) is an important parameter to map in riparian zones, as it provides information on a number of riparian zone functions. The PPC value affects the amount of light reaching the streams, which in turn regulates water temperature and the level of algal growth. The PPC measurements can also provide an estimate of riparian zone fragmentation. The PPC value has been linked to bank stability, as tree roots provide a stabilizing effect on stream banks. Finally, PPC can directly influence riparian zone and in-stream wildlife habitats, as riparian zones provide unique microclimatic conditions, refuge from fires, and in-stream woody debris for important habitats. The objective of this study was to use lidar data to map riparian zone extent, then estimate PPC within the riparian zone and validate the PPC results. The work was conducted in central Queensland, Australia. Whereas PPC was calculated at the pixel level, OBIA was used for mapping riparian zone extent and validating the PPC results.

Methods

This methods section will first present the study area followed by methods used to produce the LiDAR derived products and the OBIA of riparian zone extent and PPC with riparian zones. Finally the validation approach based on field data will be explained.

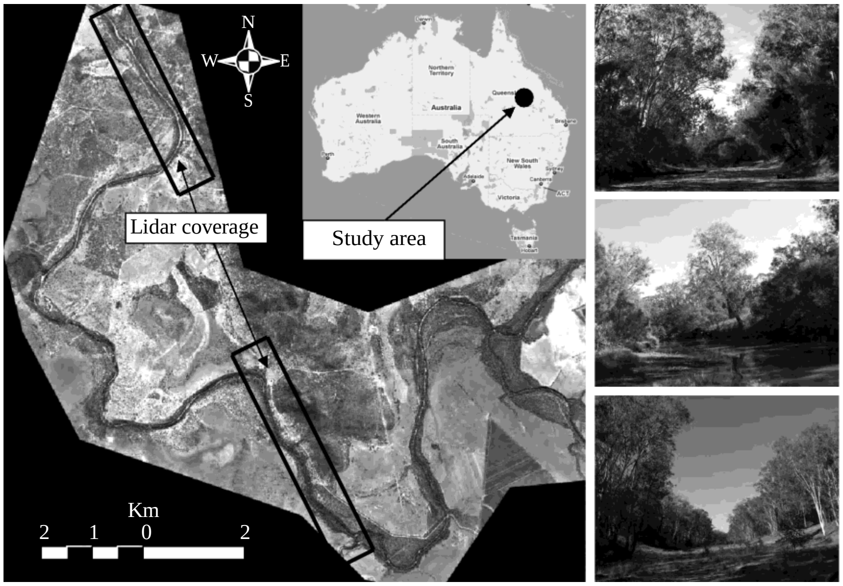

FIGURE 10.2
(See color insert following page 426.) Location and field photos of the Mimosa Creek savanna woodland riparian study site in central Queensland.

Study Area

The study area was located in central Queensland along Mimosa Creek in a subtropical savanna woodland area (24°31.S; 149°46.E; Figure 10.2). Although the riparian zone remains relatively intact, the surrounding woody vegetation has been extensively cleared for agriculture and grazing. However, patches of remnant woodland vegetation remain, and regrowth is common. The study area receives 600–700 mm of rain, mainly between October and March. The stream and riparian zone widths of Mimosa Creek were in most cases between 10 and 30 m and 15 and 80 m, respectively. Riparian vegetation ranged from open to very dense canopy with varying amounts of subcanopy vegetation.

Production of Standard Light Detection and Ranging Products

Lidar data were captured by the Leica ALS50-II sensor on July 15, 2007 along Mimosa Creek, 6 weeks after the field acquisition campaign. The lidar data were captured approximately 1000 m above terrain, and consisted of 4 returns and a point density of 4 points/m^2. The lidar returns were classified as ground or nonground by the data provider using proprietary software.

The following four lidar products were produced for use in OBIA: (1) digital terrain model (DTM), (2) terrain slope, (3) fractional cover count, and (4) canopy height model (Figure 10.3). The DTM was produced at a pixel size of 0.5 m using an inverse distance-weighted interpolation of returns classified as ground hits. From this DTM, the rate of change in horizontal and vertical directions was calculated to produce a terrain slope layer. Fractional cover count, defined as 1 minus the gap fraction probability, was calculated from the proportion of counts from first returns 2 m above the ground level

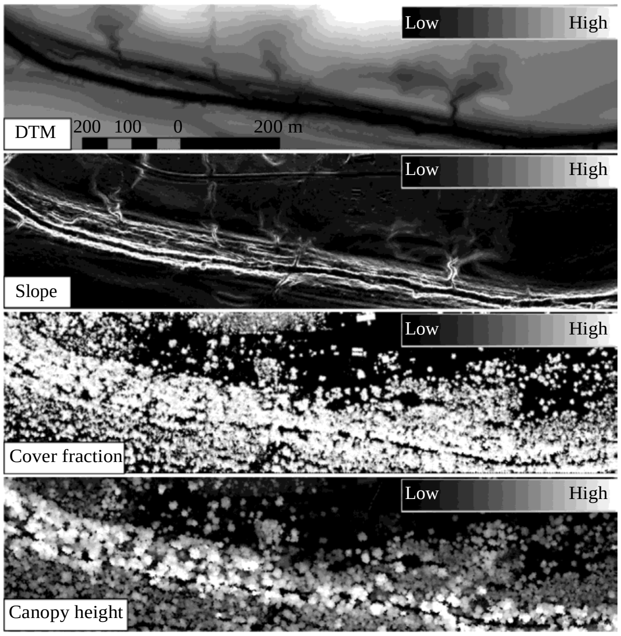

FIGURE 10.3
Light detection and ranging–derived raster products, including a digital terrain model, terrain slope, fractional cover counts, and a layer showing the maximum height of first returns within each pixel, used as input bands for object-based image analysis.

within 2.4 × 2.4 m bins. The height threshold of 2 m above the ground was also used in the field for measuring PPC. A detailed explanation of calculating PPC from fractional cover counts can be found in the study by Armston et al. The height of all first returns above the ground was calculated by subtracting the ground elevation from the first return elevation to obtain a representation of the top of the canopy. These lidar-derived raster products were used for OBIA to derive maps of riparian zone extent and PPC.

Mapping Riparian Zone Extent

To map PPC within the riparian zone, the riparian zone extent had to be mapped. As the streambed defines the interior edge of the riparian zone, the streambed extent was first classified. The external perimeter of the riparian zone was mapped from a combination of geomorphic and vegetation characteristics. The Definiens Developer 7 software was used for mapping the streambed and the riparian zone extent.

The segmentation process first split the image up into small square objects using chessboard segmentation. As streambeds are normally located at the lowest elevation in the landscape, the small square objects with the lowest minimum DTM values were first identified. As streambeds are generally flat and surrounded by steep stream banks, objects in contact with the minimum-value DTM object were continuously fused as long as they did not exceed a terrain slope of 8° and a DTM height difference of more than 1.5 m compared to the minimum DTM values. This produced one large object, with the majority of the area belonging to the streambed. This area was segmented once again using chessboard segmentation, and context, slope, and elevation information was used to refine the area belonging to the streambed to establish the internal borders of the riparian zone.

The mapping of the riparian zone extent was carried out using both vegetation and geomorphic information from the lidar-derived PPC, canopy height model, DTM, and terrain slope layers (Figure 10.4a). The segmentation and classification processes required some prior knowledge, which in this case was obtained through fieldwork measurements to ensure accurate mapping. A chessboard segmentation producing small square objects was initially used to set conditions for mapping potential riparian vegetation if the objects were within 100 m from the streambed and had a PPC value >40% and a tree height >8 m (Figure 10.4b). The thresholds were based on field measurements. Then, areas next to the streambed with steep slopes of >10° were classified as banks. The stream banks can be considered part of the riparian zone even without the presence of vegetation (Figure 10.4c). Objects enclosed by potential riparian vegetation and stream banks were classified as gaps and included as potential riparian vegetation (Figure 10.4d and e). After merging potential riparian vegetation, banks, and gaps, those objects that did not border the streambed were omitted (Figure 10.4e and f). Elevation differences between the streambed and the external perimeter of the riparian zone provided very useful information for mapping the riparian zone extent to ensure the riparian zones do

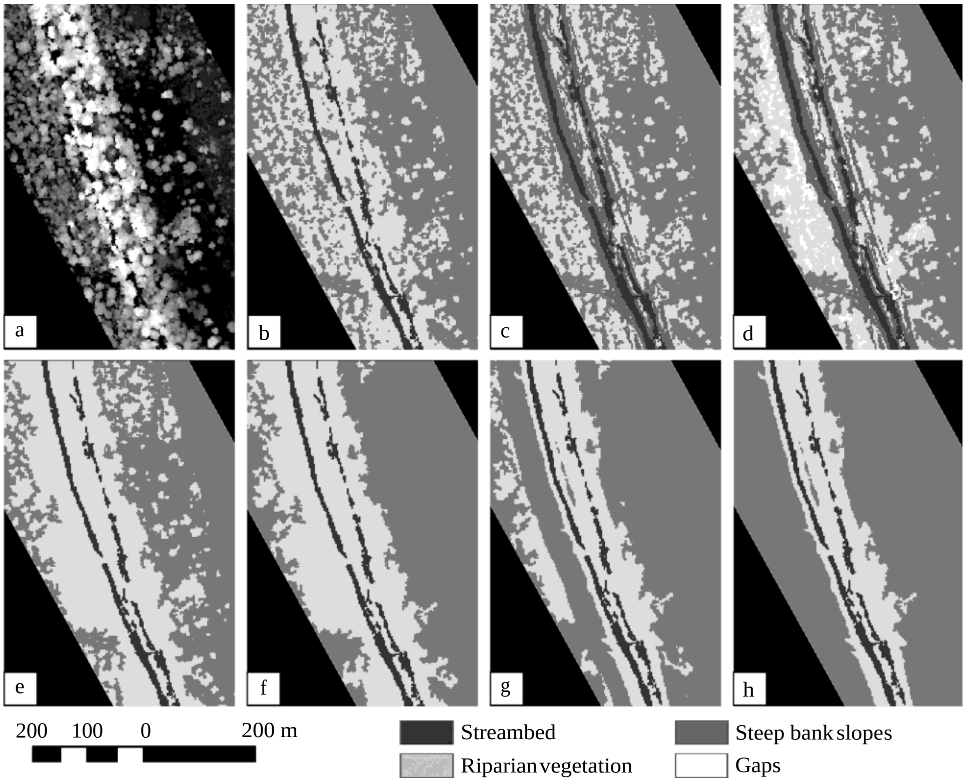

FIGURE 10.4
(See color insert following page 426.) Object-based image analysis steps for mapping the extent of the riparian zone from light detection and ranging data ((a) through (h)).

not extend into nonriparian areas in hilly landscapes. Based on field observations, a DTM value of 5 m above the streambed was set as the maximum elevation for riparian zones within a distance of 100 m from the streambed (Figure 10.4g). Potential riparian zone objects were then merged and omitted if they were not in contact with the streambed. As the external riparian zone perimeter is often defined based on the vegetation and canopy extent, a region-growing algorithm was applied to grow the extent of the riparian zone if PPC >70%, the distance to the streambed was <100 m, and the elevation difference between the streambed and the riparian zone perimeter was <7 m (Figure 10.4h).

Plant Projective Cover Mapping

The PPC was mapped at the pixel level using the lidar-derived fractional cover count layer and an existing power function:

$$\mathrm{PPC} = 1 - \mathrm{P_{gap}}^{0.6447}$$

where P_{gap} is 1 minus the lidar cover fraction. The riparian zone extent map was used to mask the PPC layer.

Field Data Acquisition and Validation

Field data were obtained at 11 sites within the area covered by the lidar data. At each site, the widths of the riparian zone and the streambed were measured with a tape measure. Digital vertical photos were taken of the canopy cover using a lens with a focal length of 35 mm, at 5-m intervals along 5 parallel transects at each site located perpendicular to the stream. These transects started at the edge of the streambed and ended at least 10 m beyond the external perimeter of the riparian zone. The field photos were analyzed and converted to a measure of PPC using the approach by van Gardingen et al. The global positioning system (GPS) readings averaged for 20 minutes at the start and end of each transect line, and were used for georeferencing.

As the field photos covered slightly different areas of the canopy because of the varying heights of the lower parts of the canopy and in order to take into account slight geometric offsets between field and lidar data, a pixel-based validation approach was deemed inappropriate. An object-based approach was found most suitable for the integration of field and lidar data. To keep objects homogenous and thereby avoid the averaging out of variance of pixel values, the PPC layer was used for a multiresolution segmentation with a maximum focus on color as opposed to shape. The object sizes were approximated to single tree crowns, clusters of tree crowns, and individual gaps. This preserved extreme values from areas with very dense and sparse canopy cover. The PPC values derived from field photos taken within the corresponding objects were averaged and related to the mean PPC value of the respective object. Field-derived photo points located within 2 m of an object edge were omitted to take into account geometric offsets between field and lidar data and the uncertainty of the areal coverage of the canopy within the field photos.

Results and Discussion

The width of the riparian zone, and hence the riparian zone extent, was accurately mapped from the lidar data as PPC; tree height and geomorphic characteristics such as bank slope and elevation differences provided useful information in addition to contextual

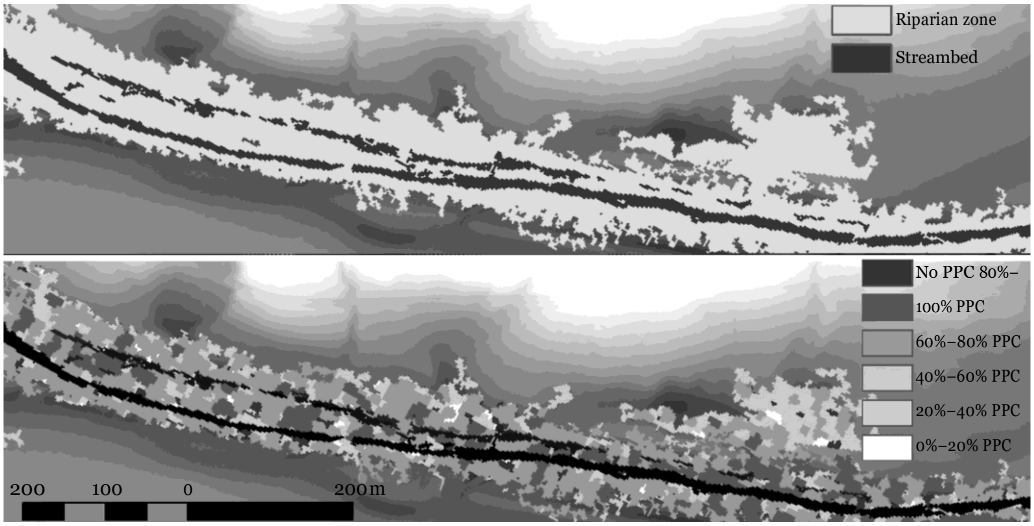

FIGURE 10.5
(See color insert following page 426.) Mapped riparian zone extent and plant project cover overlaying the digital terrain model.

class-related information ($R^2 = 0.99$, root-mean-square error (RMSE) = 3.2 m, and $n = 10$; Figure 10.5). However, knowledge from fieldwork regarding the maximum riparian zone width, stream bank slope, and elevation differences between the streambed and the external perimeter of the riparian zone enabled calibration of the parameters of the developed rule set. The PPC within the riparian zone could be mapped using the OBIA-derived riparian zone extent as a mask and the algorithm developed by Armston et al. for the conversion of lidar-derived fractional cover counts to PPC (Figure 10.5). A major advantage of the OBIA approach was the use of contextual information in relation to the mapped streambed. Knowing the location and the extent of the streambed enabled the use of features such as distance to the streambed, relative border of the streambed, and elevation difference in relation to the streambed for mapping the riparian zone extent. The initial segmentation into small square objects and the subsequent merging and region-growing algorithms were useful and enabled the integration of context information. The object-based approach using lidar data for mapping riparian zone extent and validating predicted PPC within the riparian zone was robust for the study area examined and reduced the effects of slight misregistrations between field and image data, which often complicate the integration of pixel-based analysis of high spatial resolution image and field data.

The matchup of single photo points with single pixels or windows of pixels, for example, 3 × 3 pixels, within imaged areas exhibiting large PPC variations resulted in a relationship with larger RMSE values between field and lidar data. The validation of PPC using independent PPC measurements showed a better relationship between field and lidar-derived PPC when assessed at the object level (Figure 10.6). This was because of the averaging of field measurements and pixels into homogenous objects rather than using square windows of pixels not taking into account PPC homogeneity. The use of windows of 15 × 15 m averaged out many of the extreme PPC values, as no consideration was given to the PPC homogeneity within the windows. As a small-scale parameter of 10 was used

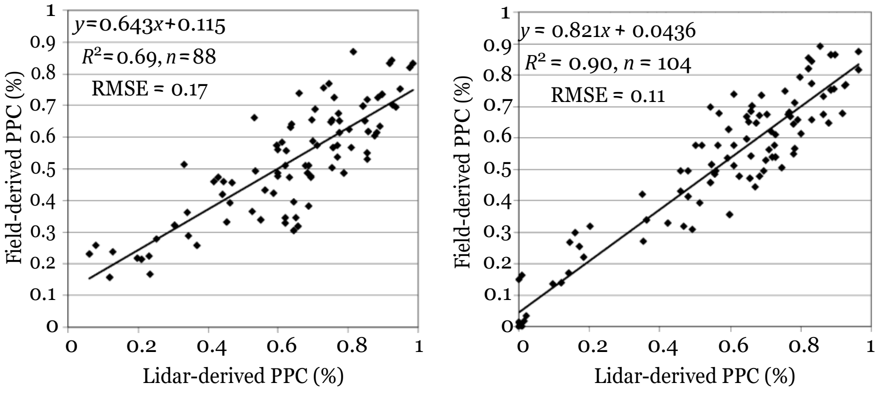

(a) (b)

FIGURE 10.6
Relationship between field and light detection and ranging–derived plant projective cover assessed at (a) 225-m^2 square plots and (b) object-derived plots. (From Johansen, K. et al. 2010b. *Ecol Indic* 10(4). With permission.)

for the multiresolution segmentation of the PPC layer with emphasis on color, that is, PPC values, areas with similar PPC values were merged. The integration of field data (averaged within each object) and PPC objects reduced issues related to slight geometric offsets between field and image data. Also, as the canopy photos corresponded to areas of different sizes of the canopy, because of the varying heights of the lower parts of the photographed canopy cover, the object-based approach was found to be more suitable. These results indicate that object-based techniques may be used for model inversion for extracting key riparian biophysical parameters from high spatial resolution image and field data.

Summary

Object-based image analysis proved to be a powerful tool for mapping riparian zone extent and integrating high spatial resolution image and field data. Contextual information proved to be essential for mapping riparian zone extent from lidar-derived raster products. The fine detail of high spatial resolution lidar and field data was more appropriately integrated at the object level to preserve the full range of image layer values and to account for potential geometric offsets between the data sets. The developed approach may be used in other woodland riparian areas having similar contextual landscape and stream characteristics with minor adjustments required for slope, elevation, PPC, and riparian zone width input parameters based on field measurements.

Case Study 2: Tree Crown Extraction in a Low Mountain Range Area from UltraCamX-Derived Surface Models Using Object-Based Image Analysis and Grid Computing Techniques

The second case study focuses on the identification of single trees and the delineation of tree crowns, based on UltraCamX-derived surface models and the application of grid computing techniques for specific high data volume–processing.

Introduction

The second case study focuses on the identification of single trees. In the last decade, several algorithms were developed to extract individual tree parameters from high spatial resolution data supporting forest inventories. Through the availability of high spatial resolution digital surface models (DSMs)—at the moment primarily captured by airborne laser scanning (lidar)—forest inventories of the future will be increasingly based on such data sets. Biophysical structural parameters such as tree density, tree height, crown width, and plant projective cover can be automatically extracted from high spatial resolution DSM data over large spatial extents. Various research applications already exist in this area, and especially the combination of multispectral imagery and DSM data is considered very promising for future forest inventories. An overview of applications for automated forest parameter extraction is given by Koch and Dees, and Mallet and Bretar. Since acquisition of laser-scanning data for DMS creation is still expensive and complex for short-term monitoring duties, for example, for yearly bark beetle monitoring, the aim of this study was to extract individual tree crowns from DSM data, which was calculated using airborne high spatial resolution UltraCamX stereo image data. In this study, trees that were taller than 2 m were considered, and their height and crown width were derived. Coniferous and deciduous species were differentiated based on the spectral reflectance information of the imagery. Moreover, grid computing techniques were applied to cope with the large amount of data and, in this case, the computationally intensive OBIA.

Methods

This methods section gives an overview about the study area and the data sets used followed by the description of the developed algorithm for single tree crown extraction and the field data based validation approach.

Study Area and Data

The study area comprises almost 14 km^2 of forested area in the federal state of Upper Austria, Austria (Figure 10.7a). It is a low mountain forest area dominated by spruce (*Picea abies*) and beech (*Fagus sylvatica*) stands. Other tree species such as firs, sycamores, Douglas firs, and alders cover less than 7% of the area.

In this case study, data from different sources were combined: airborne multispectral UltraCamX stereo image data, a DSM derived from these data, representing the Earth's surface including features such as vegetation, buildings, and bridges, and an already existing DEM, representing ground surface topography, derived from lidar data (Figure 10.7c). Because of limited ground surface topographic variation, the DEM was deemed suitable to use for several monitoring cycles to normalize the DSM (nDSM) derived from the UltraCamX stereo data, by subtracting the DEM from the DSM. This means that the time frame between different airborne lidar acquisitions can be expanded for our study area and compensated by UltraCamX data, with the benefit of capturing not only up-to-date DSM data but also current optical imagery.

The UltraCamX frames were acquired with 80%/60% overlap in October 2008, resulting in digital infrared orthophotos with a pixel size of 0.125 m. From these data, a DSM was produced by Forest Mapping Management (FMM) of Austria, with the same spatial resolution. Additionally, a DEM based on lidar data from April 2007 with a pixel size of 1 m was provided by the federal state of Upper Austria, which was used to normalize

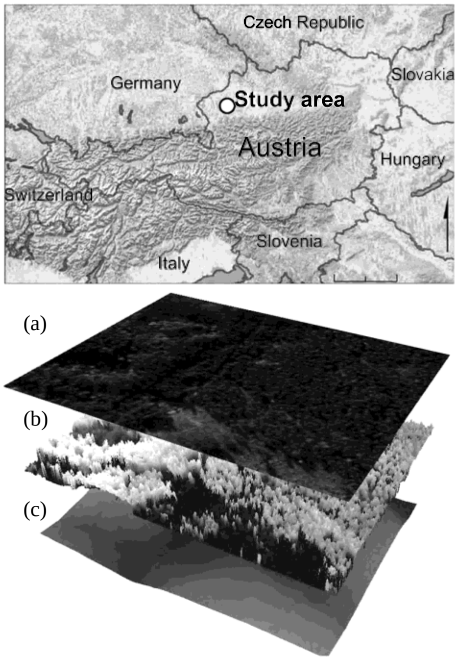

FIGURE 10.7
(See color insert following page 426.) Location of the study area in the Austrian state of Upper Austria. Data sets used in the case study are (a) UltraCamX digital infrared orthophotos, (b) normalized digital surface model derived from the UltraCamX stereo imagery, and (c) an existing light detection and ranging–based digital elevation model.

the surface model (nDSM), that is, to get real vegetation heights. The height accuracy of the lidar data in the forested area was between ±20 and ±50 cm, positional accuracy was ±30 cm, and point density was 1.7 points/m^2 (DORIS 2009).

Algorithm Development

For individual tree crown extraction, an object-based algorithm written in Cognition Network Language (CNL; in the Definiens developer software) by Tiede and Hoffmann was adapted to the very high spatial resolution nDSM data set. The algorithm starts from local nDSM maxima as seed points and delineates individual tree crowns based on underlying height values and height-value changes. This innovative approach uses a region-controlled extraction of local maxima as well as region-controlled parameters in the rule set. Regions were initially delineated at a coarser spatial scale to represent stand-like units with similar height and vegetation structure. In this case, four different regions representing different average stand heights were distinguished. This a priori information controlled the tree crown extraction rule sets for every region, aiming to adapt the algorithm to the regional forest structure types. The core delineation process was performed in two steps: (1) The regions were broken down into pixels ("pixel-sized objects") within a region's boundary. (2) From these pixel-sized objects, tree crowns were built in a region-growing manner using local maxima as seed points, that is, the following parameters were automatically adapted depending on the particular region: The search radius for the local-maximum method was automatically adapted for each region depending on the average height; a stopping criterion for the region-growing process depending on the underlying nDSM data was adapted, if the candidate objects that were taken into account exceeded a certain height difference, assuming that in this case the crown edge has been reached; and a maximum crown width to avoid uncontrolled growth of tree crowns in case a local maximum was not detected correctly, preventing a merging of objects with other potential tree crowns. This last parameter was also dependent on the height information given by the initially delineated regions. In the last step, the resulting tree crowns were separated into coniferous or deciduous trees, based on their spectral reflectance properties represented in the orthophoto data.

Because of the large data volume (nDSM >10 GB; approximately 900 million pixels), there was a need for specific high data volume–processing techniques to be applied. Grid computing techniques were applied within the eCognition Server (developed by Definiens) environment to automatically split the data set into 65 tiles, which were then distributed for processing among different computers (Figure 10.8a). The same rule set was applied to each tile, and the tiled results were subsequently merged. This process allowed the processing of large data sets and significantly decreased the processing time. However, stitching of the tiles required postprocessing of the results in order to remove errors introduced at the boundaries of the different tiles. Examples of these errors include double crowns because of biased local-maxima calculations or half-delineated crowns due to the breaking off of the region-growing algorithm, which can occur at the border of the tiles if a crown is divided. Although the crown representation in nDSM data yields only one local maximum, the division of the crown due to the tiling process can potentially bias the local-maximum search. For each of the divided crown representations, a maximum is found, and the region-growing algorithm uses each maximum as a seed point but breaks off at the image tile border (Figure 10.8b). A Visual Basic for Applications (VBA) routine in ArcGIS

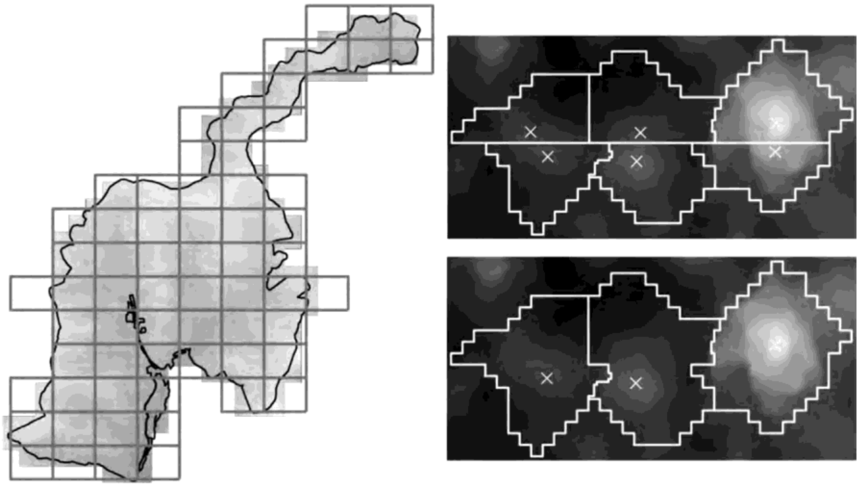
(a) (b)

FIGURE 10.8
Tiling of normalized digital surface model (nDSM) using the eCognition Server: (a) Tiling of the nDSM into 65 parts for applying grid computing techniques, and (b) automated postprocessing of extracted tree crowns and crown maxima at the border of the tiles. Double crowns were merged and double local maxima were removed.

was programmed to postprocess the results, that is, by removing multiple local maxima within the same tree crown by keeping the tallest point, and subsequently merging split tree crowns that were originally delineated as two separate crowns in two different tiles.

Validation

Quantitative validation of the tree crown extraction results was conducted by a forest expert using field measurements and classical forest inventories in the study area (Austrian Forest Inventory), which is one of the most intensive national forest-monitoring systems in Europe. From circular plots of 100 m^2, relevant tree parameters, such as tree height, tree species, and forest stand structure, were measured. The position of each plot was measured with a GPS receiver from the center of the circular plots.

Results

A total of approximately 380,000 tree crowns with heights above 2 m were automatically extracted, and almost the same amount of tree crowns were delineated (Figure 10.9). The relatively few exceptions were mainly dead trees or trees with no distinct crown. Calculation time, without pre- and postprocessing, comprised 20 hours by usage of three standard personal computers. The required processing time can be reduced further if the number of computers used is increased. The development of the rule set was more time consuming, but through the use of normalized surface height data, the transferability of the rule set to other images or areas was improved. Rule sets relying on spectral information generally require modification of thresholds and membership functions between different images, because of differences in seasonality, time of image acquisition, and atmospheric effects. The only part of the algorithm relying on spectral information was the differentiation of different species after the tree crown extraction process.

Single Tree Extraction

Field validation showed that the automated tree crown extraction results depended on the height of the individual tree crown. In Table 10.1, the validation results for different stand height classes are visualized together with the number of GPS-measured validation plots and the average tree detection rate per stand height class. In stands with average tree heights of 14–18 m, the average detection rate was 64%, whereas stands with an average height >26 m had detection rates over 90%. Problems were encountered in stands with complex structures, where several individual tree crowns were counted as one tree. The opposite situation, that is, identification of more crowns than the number of trees present, occurred for some deciduous trees and trees with distinct within-canopy foliage clumping (double crowns), where two or more local maxima per tree were detected. The latter case can be considered a general methodological problem utilizing local-maximum-based algorithms.

In coniferous stands with an average height >18 m, comparison with on-ground forest inventories revealed results that are suitable for use in operational mapping environments without postclassification corrections. In mixed stands, results depended on the proportion of different species, type of species, and vertical structure of the stands.

Tree Height Derivation

The extracted heights of the trees showed a higher accuracy than measurements for classical forest inventories. Comparisons between automated and manual height estimations

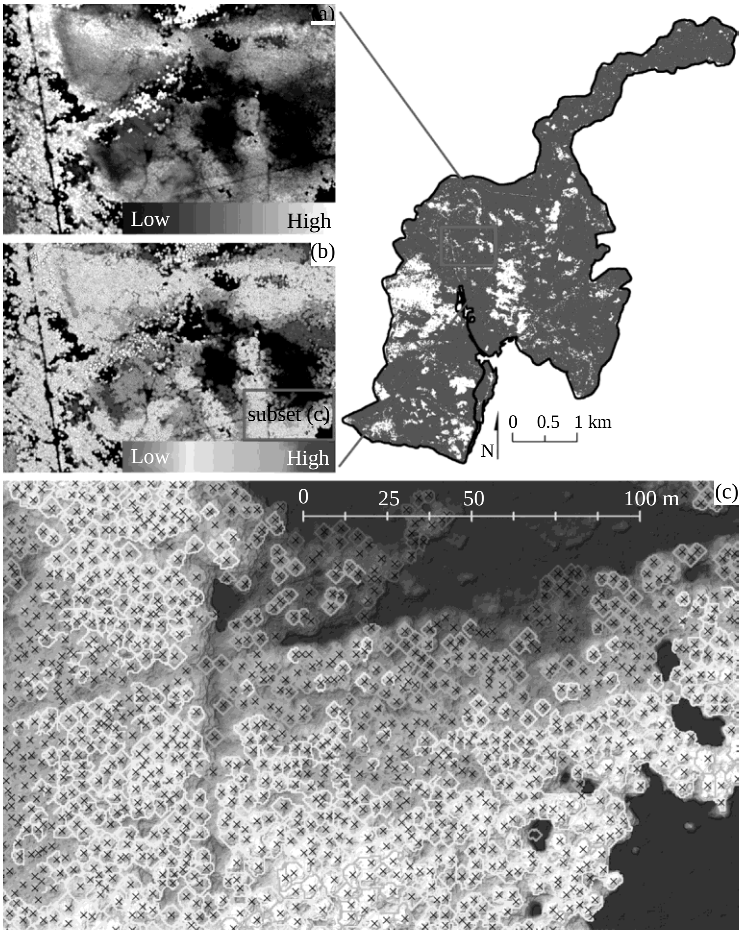

FIGURE 10.9
(See color insert following page 426.) Results of individual tree crown extraction and delineation for the whole study area (right) and subsets showing (a) the normalized digital surface model, (b) the overlaid tree crowns, and (c) the tree crowns with the extracted local maxima (color coded according to the extracted height values).

TABLE 10.1
Sample-Based Validation of Individual Tree Crown Extraction

Average Stand Height (m)	Number of GPS Sample Points	Tree Detection Rate (%)[a]
<14	3	52
14–18	11	64
18–22	14	77
22–26	12	86
26–30	9	94

[a] Percentage of all correctly extracted trees within a radius of 5.64 m around each GPS sample point.

in the field revealed much better results for the automated derivation of mean tree crown height and tree height (local-maximum extraction) values.

Tree Species

The differentiation of different tree species was hampered by the low solar illumination angle at the time of acquiring the UltraCamX data in October 2008. Therefore only a differentiation between coniferous and deciduous trees was performed, based on the normalized difference vegetation index (NDVI) of the imagery. In the sample plots, no errors were observed for this differentiation.

Discussion and Outlook

Individual tree crown parameters extracted from the UltraCamX data and the derived DSM could be obtained in a fast and accurate manner using automated OBIA methods. The results offer possibilities for more cost-efficient forest-monitoring tasks in the future. The available data sets were acquired in October 2008, and yielded a high degree of shadows. It is likely that the results could be improved using data acquired between May and August. It turned out that the acquisition date did not influence the part of the workflow that used lidar data, although it hampered a species differentiation based on optical data.

For even-aged forests, the proposed method is able to deliver relevant stand and tree crown parameters. Although the tree crown detection in evenly structured stands is troubled, the delineation of stand structures based on individual trees is another advantage compared to the manual estimations used in forest inventories. Also, an automated derivation of growing stock under the consideration of the respective tree crown size could lead to more objective or comprehensible growing stock estimations than forest taxation in the field.

Compared to classical forest inventories (in western and central Europe), this approach reveals a possibility to produce faster and more accurate results, mainly through the reduction of manual measurement expenditure. Object-based approaches are in this case bridging the gap between remote sensing and GIS. The results are GIS-ready and parameterized information about single trees and can directly be fed into forest inventory databases and GISs. Future research will focus on the transferability of the approach to areas that are dominated by deciduous trees, and also on a more general comparison of parameters derived from airborne lidar data–based DSMs and high-resolution optical data. It should be emphasized that the comparisons of lidar data and UltraCamX data in this context address only the derived products (DSM and DEM), not the sensors, generally. Lidar data with multiple returns allow measurements of vertical structural parameters from a single data set, whereas the calculation of a DSM from stereo UltraCamX data, as used in this case study, offers continuous optical data at very high spatial resolutions. On the contrary, achieving a similarly high spatial resolution and vertical accuracy with lidar data, would require a very high point density during lidar data acquisition.

Summary and Discussion

The case studies described in this chapter demonstrate how OBIA can be used to improve vegetation mapping through the use of not only spectral and textural information but also geometric (width or size of an object) and contextual information. These capabilities significantly improve the ability to accurately map vegetation biophysical parameters. For high spatial resolution vegetation mapping applications, OBIA can improve the integration of field and image data for validation and potentially also for calibration and model development. The case studies also demonstrate the suitability of OBIA for feature extraction. Feature extraction from high spatial resolution image data has previously been hampered by the large spectral reflectance variability of individual features at the pixel level, for example, for the extraction of individual tree crowns. Through the use of objects, we may overcome this limitation by reducing the reflectance variability of single pixels. The case studies prove that there is great potential for automating the feature extraction process for vegetation studies over large spatial extents, which will undoubtedly be a major focus of future research.

Applications of OBIA are developing rapidly. Several books on OBIA/GEOBIA have been published, and several special issues of scientific journals were recently devoted to this topic. One of the most recent trends is for OBIA methods to become part of dedicated workflows and converge with mainstream GIS applications. Blaschke concludes that this rapidly increasing body of scientific literature conveys a sense of optimism that OBIA methods generate multiscale geospatial information, which is tempered by some disquiet that the increasingly complex classification rule sets and workflows raise at least as many research questions as they resolve.

There is a realization that the higher spatial resolution and detection detail available using improved optical instruments, such as radar, lidar, and even sonar, create problems with the "traditional" approach to land-use/land- cover mapping. The OBIA approach supports attempts to overcome a purely descriptive categorization of the spectral characteristics of pixels, and paves the way for a combined use of spectral and spatial (contextual) information toward developing conditioned information.

Recently, OBIA research has been directed more toward the automation of image processing. As a consequence of the rapidly increasing proliferation of high spatial resolution imagery and the improved access to this type of imagery, more and more research is now concerned with automatic object delineation. Automated object recognition is certainly an end goal, but at present, it is mainly achieved in a stepwise manner, either with strongly interlinked procedures building workflows or with clear breaks in these workflows. In both cases, the necessary steps involve addressing various multiscale instances of related objects within a single image (e.g., individual tree crowns, tree clusters, stands, and forests). An increasing number of research articles deal with object and feature recognition and feature extraction. Still, although intrinsically tied to OBIA, for the majority of applications we can note that they are not an end in themselves.

We pointed to the fact that when dealing with high spatial resolution imagery, the question of scale or addressing the right scale gains importance. As mentioned in Section 10.2.2, Burnett and Blaschke have developed a methodology to derive objects at several levels simultaneously and to utilize this information in a classification. They called it MSS/ORM. One of the underlying ideas is to provide a methodological basis for a seamlessly integrated GIS/remote sensing analysis environment. In this respect, the multiscale approach is powerful when addressing area metrics, shape metrics, topological relationships ("borders to," "is embedded in," "is surrounded by"), and hierarchical relationships ("is subobject of," "is super object of"). Lang and Langanke have, however, convincingly shown that for specific cases, an OLR might be sufficient and more straightforward than MSS/ORM. In either case, the delineation of relatively homogeneous areas is the basic method, and the common denominator of various realizations of OBIA is the objective to derive "meaningful objects." Since the appropriate scale of observation is a function of the type of environment and the type of information that is being sought, the selection of scale is very important and is a hot research topic of OBIA. Recently, Dragut, Tiede, and Levick (in press) developed a tool called "estimation of scale parameter" (ESP), which builds on the idea of local variance (LV) of object heterogeneity within a scene and allows one to iteratively generate image-objects at multiple scale levels in a bottom-up approach, while calculating the LV for each scale. Variation in heterogeneity is explored by evaluating LV plotted against the corresponding scale. It is hoped that one of the major obstacles of OBIA, namely, the selection of the right scale, may be overcome with such tools. In this case, thresholds in the rates of change of LV may indicate scale levels at which the image can be segmented in an appropriate manner, relative to the data proper- ties at the scene level.

Future Research

Today, the bottleneck of large data volume throughput can be overcome by the use of server technologies. As this technology has become accessible for government departments and private agencies only within the last few years, it is likely to have major future implications on the OBIA of vegetation for large-area mapping relative to spatial resolution. In this chapter, we described two case studies with large data volumes. The Austrian study area was spread over 14 km^2 with a pixel size of 12.5 cm. This resulted in 900 million pixels. Such large amounts of data were impossible to process a few years ago. Despite the enormous progress in processing power, we point out that as the spatial extent, and hence the data volume, for OBIA increases, more conditions will need to be fulfilled in order to accurately map vegetation parameters over large areas. We conclude that more complex rule sets with increasing transferability are required, and multiscale analyses are often mandatory, which require (multi-)scale concepts. The transferability of rule sets may be improved through the use and integration of existing geographic information from spatial data infrastructures. The integration of the temporal domain through the time-series analysis of vegetation dynamics may also provide additional information for integration into rule sets, but the ontological and epistemological foundation of OBIA is still in its infancy.

An increasing number of OBIA subdisciplines are likely to develop in the future through further developments in software, available image and spatial data, and increasing research in this area. From this review of OBIA and the two case studies, we conclude that OBIA has major advantages for vegetation mapping because of the high levels of reflectance variability within individual vegetation features. The addition of shape and contextual information improves the capability to map vegetation features and structural parameters. However, because of the complexity of vegetation reflectance characteristics and vegetation dynamics, many challenges still remain for OBIA-based vegetation studies. We believe that with the continuing human impact on vegetation and predicted climate change, there is an urgent need to explore this new mapping discipline in order to take full advantage of its potential and to build up further capacities for detailed operational mapping and monitoring of vegetation through the use of OBIA.

Chapter 3

Remote Sensing Image Classification

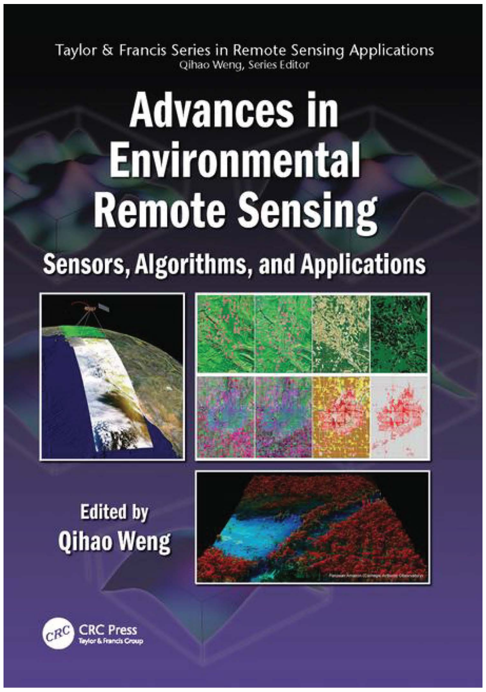

Advances in Environmental Remote Sensing: Sensors, Algorithms, and Applications

By Qihao Weng

© 2011 Taylor & Francis Group. All rights reserved.

To purchase a copy, click here.

Overview of Image Classification Procedure

Classification of remotely sensed imagery is a complex process and requires the consideration of many factors. Figure 9.1 illustrates the major steps of an image classification proce- dure. Sections 9.2.1 through 9.2.8 provide brief descriptions for each step.

Nature of Remote Sensing Image Classification

Before implementing image classification for a specific study area, it is very important to clearly define the research problems that need to be solved, the objectives, and the location and size of the study area. In particular, clearly understanding the needs of the end user is critical. It is helpful to list some questions, such as the following: What is the detailed classification system and what are the most interesting land covers? What is the accuracy for each land cover or overall accuracy? What is the minimum mapping unit? What previous research work has been done and how can one maintain compatibility with it? What data sources are available and what data are required? What are the time, cost, and labor constraints? These questions directly affect the selection of remotely sensed data, selection of classification algorithms, and design of a classification procedure for a specific purpose.

Determination of a Classification System and Selection of Training Samples

A suitable classification system is a prerequisite for successful classification. In general, a classification system is designed based on the user's needs, the spatial resolution of the remotely sensed data, compatibility with previous work, available image-processing

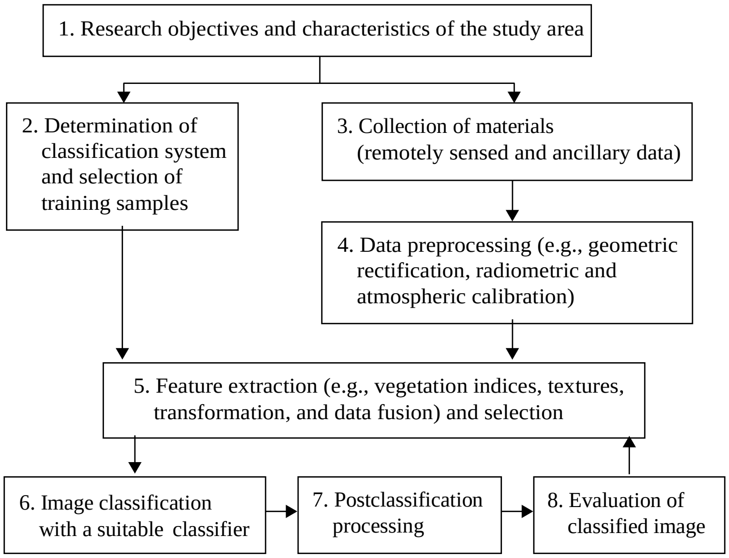

FIGURE 9.1
Major steps involved in the image classification procedure.

and classification algorithms, and time constraints. Such a system should be informative, exhaustive, and separable. In many cases, a hierarchical classification system is adopted to take different conditions into account.

A sufficient number of training samples and their representativeness are critical for image classifications. Training samples are usually collected from fieldwork or from fine spatial resolution aerial photographs and satellite images. Different collection strategies, such as single pixel, seed, and polygon, may be used, but they will influence classification results, especially for classifications with fine spatial resolution image data. When the landscape under investigation is complex and heterogeneous, selection of a sufficient number of training samples becomes difficult. This problem becomes complicated if medium or coarse spatial resolution data are used for classification, because a large volume of mixed pixels may occur. Therefore, selection of training samples must consider the spatial resolution of the remote sensing data being used, the availability of ground reference data, and the complexity of the landscapes under investigation.

Selection of Remotely Sensed Data

Remotely sensed data have different spatial, radiometric, spectral, and temporal resolutions. Understanding the strengths and weaknesses of different types of sensor data is essential for selecting suitable remotely sensed data for image classification. Some previous literature has reviewed the characteristics of major types of remote sensing data. The selection of suitable remotely sensed data requires considering such factors as the needs of the end user, the scale and characteristics of the study area, available image data and their characteristics, cost and time constraints, and the analyst’s experience in using the selected images. The end user’s need determines the nature of classification and the scale of the study area, thus affecting the selection of remotely sensed data. In general, at a local level, a fine-scale classification system is needed, thus high spatial resolution data such as IKONOS and QuickBird data are helpful. At a regional scale, medium spatial resolution data such as those from Landsat TM and Terra Advanced Spaceborne Thermal Emission and Reflection Radiometer (ASTER) are the most frequently used data. At a continental or global scale, coarse spatial resolution data such as Advanced Very High Resolution Radiometer (AVHRR), Moderate Resolution Imaging Spectroradiometer (MODIS), and System Pour l'Observation de la Terre (SPOT) vegetation data are preferable.

Atmospheric condition is another important factor that influences the selection of remote sensing data. The frequent cloudy conditions in moist tropical regions are often an obstacle for capturing high-quality optical sensor data. Therefore, different kinds of radar data may serve as an important supplementary data source. Since multiple sources of sensor data are now readily available, image analysts have more choices to select suitable remotely sensed data for a specific study. In this situation, monetary cost is often an important factor affecting the selection of remotely sensed data.

Image Preprocessing

Image preprocessing may include the examination of image quality, geometric rectification, and radiometric and atmospheric calibration. If different ancillary data are used, data conversions among different sources or formats and quality evaluation of these data are necessary before they can be incorporated into a classification procedure. The examination of original images to see any remote sensing system–induced radiometric errors is necessary before the data are used for further processing. Accurate geometric rectification or image registration of remotely sensed data is a prerequisite for combining different source data in a classification process.

If a single-date image is used for classification, atmospheric correction may not be required. However, when multitemporal or multisensor data are used, atmospheric calibration is mandatory. This is especially true when multisensor data, such as TM and SPOT or TM and radar are integrated for an image classification. A variety of methods, ranging from simple relative calibration to the dark-object subtraction (DOS) method and complex physically based models (e.g., second simulation of the satellite signal in the solar spectrum [6S]), have been developed for radiometric and atmospheric correction. Topographic correction is important if the study area is located in rugged or mountainous regions. A detailed description of atmospheric and topographic correction is beyond the scope of this chapter. Interested readers may check the references cited in this section to identify a suitable approach for a specific study.

Feature Extraction and Selection

Selecting suitable variables is a critical step for successfully performing an image classification. Many potential variables may be used in image classification, including spectral signatures, vegetation indices, transformed images, textural or contextual information, multitemporal images, multisensor images, and ancillary data. Because of the different capabilities of these variables in land-cover separability, the use of too many variables in a classification procedure may decrease classification accuracy. It is important to select only those variables that are most useful in separating land-cover or vegetation classes, especially when hyperspectral or multisource data are employed. Many approaches, such as principal component analysis, minimum noise fraction transform, discriminant analysis, decision boundary feature extraction, nonparametric weighted feature extraction, wavelet transform, and spectral mixture analysis, may be used for feature extraction, in order to reduce the data redundancy inherent in remotely sensed data or to extract specific land-cover information.

Optimal selection of spectral bands for image classification has been extensively discussed in the literature. Graphic analysis (e.g., bar graph spectral plots, cospectral mean vector plots, two-dimensional feature space plot, and ellipse plots) and statistical methods (e.g., average divergence, trans- formed divergence, Bhattacharyya distance, and Jeffreys–Matusita distance) have been used to identify optimal subsets of bands (Jensen 2005). In practice, divergence-related algorithms based on training samples are often used to evaluate class separability and select optimal bands.

Selection of a Suitable Classification Algorithm

In recent years, many advanced classification approaches, such as artificial neural networks, decision trees, fuzzy sets, and expert systems, have been widely applied in image classification. Cihlar discussed the status and research priorities of land-cover mapping for large areas. Franklin and Wulder assessed land-cover classification approaches with medium spatial resolution remotely sensed data. Published works by Tso and Mather and Landgrebe specifically focused on image-processing approaches and classification algorithms. In general, image classification approaches can be grouped into different categories, such as supervised versus unsupervised, parametric versus nonparametric, hard versus soft (fuzzy) classification, per-pixel, subpixel, and perfield. There are many different classification methods available. For the sake of convenience, Lu and Weng (2007) grouped classification approaches as perpixel, subpixel, per-field, contextual, and knowledge-based approaches, and a combination approach of multiple classifiers, and described the major advanced classification approaches that have appeared in the recent literature. In practice, many factors, such as the spatial resolution of the remotely sensed data, different data sources, classification systems, and the availability of classification software, must be taken into account when selecting a classification method for use. If the classification is based on spectral signatures, parametric classification algorithms such as maximum likelihood are often used; otherwise, if multisource data are used, nonparametric classification algorithms such as the decision tree and neural network are commonly used. Spatial resolution is an important factor affecting the selection of a suitable classification method. For example, high spectral variation within the same land-cover class in high spatial and radiometric resolution images such as those from QuickBird and IKONOS often results in poor classification accuracy when a traditional per-pixel classifier is used. In this circumstance, per-field or object-oriented classification algorithms outperform per-pixel classifiers.

For medium and coarse spatial resolution data, however, spectral information is a more important attribute than spatial information because of the loss of spatial information. Since mixed pixels create a problem in medium- and coarse-resolution imagery, per-pixel classifiers have repeated difficulties in dealing with them. Subpixel-based classification methods can provide better area estimation than per-pixel-based methods.

Postclassification Processing

Research has indicated that postclassification processing is an important step in improving the quality of classifications. Its roles include the recoding of land use/cover classes, removal of "salt-and-pepper" effects, and modification of the classified image using ancillary data or expert knowledge. Traditional per-pixel classifiers based on spectral signatures often lead to salt-and-pepper effects in classification maps due to the complexity of the landscape. Thus, a majority filter is often applied to reduce noise. Also, ancillary data are often used to modify the classification image based on established expert rules. For example, forest distribution in mountainous areas is related to elevation, slope, and aspects. Data describing terrain characteristics can be used to modify classification results based on the knowledge of specific vegetation classes and topographic factors. In urban areas, housing or population density is related to urban land-use distribution patterns, and such data can be used to correct some classification confusions between commercial and high-intensity residential areas or between recreational grass and crops. As more and more ancillary data, such as digital elevation models (DEMs) and soil, roads, population, and economic data become available, geographic information systems (GIS) techniques will play an important role in managing these ancillary data and in modifying the classification results using the established knowledge or relationships between land cover and these ancillary data.

Evaluation of Classification Performance

The evaluation of classification results is an important process in the classification procedure. Different approaches may be employed, ranging from a qualitative evaluation based on expert knowledge to a quantitative accuracy assessment based on sampling strategies. A classification accuracy assessment generally includes three basic components: (1) sampling design, (2) response design, and (3) estimation and analysis procedures. The error matrix approach is one of the most widely used in accuracy assessment. In order to properly generate an error matrix, one must consider the following factors: reference data collection, classification scheme, sampling scheme, spatial autocorrelation, and sample size and sample unit. After the generation of an error matrix, other important accuracy assessment elements, such as overall accuracy, omission error, commission error, and kappa coefficient, can be derived. In particular, kappa analysis is recognized as a powerful method for analyzing a single error matrix and for comparing the differences among various error matrices. Many authors, such as Congalton, Janssen and van der Wel, Smits, Dellepiane, and Schowengerdt, Foody, and Congalton and Green, have reviewed the methods for classification accuracy assessment.

Overview of Major Techniques for Improving Classification Performance

Different remotely sensed data will have variations in spatial, spectral, radiometric, and temporal resolutions, as well as differences in polarization. Making full use of these characteristics is an effective way of improving classification accuracy. Generally speaking, spectral response is the most important information used for land-cover classification. As high spatial resolution data become readily available, textural and contextual information become significant in image classification. This section discusses some major techniques used for improving the performance of land-cover classification.

Use of Spatial Information

The spatial resolution of an image determines the level of detail that can be observed on the Earth's surface, and spatial information plays an important part in improving land use/cover classification accuracy, especially when high spatial resolution images such as IKONOS and QuickBird images are employed. A major advantage of these fine spatial resolution images is that such data greatly reduce the mixed-pixel problem, and there is the potential to extract much more detailed information on land-cover structures from these data than from medium or coarse spatial resolution data. However, some new problems associated with fine spatial resolution image data emerge, notably the shadows caused by topography, tall buildings, or trees, and the high spectral variation within the same land-cover class. These challenges may lower classification accuracy if classifiers cannot effectively handle them. The huge amount of data storage capacity and severe shadow problems in fine spatial resolution images leads to challenges in selecting suitable image-processing approaches and classification algorithms. Spatial information may be used in different ways, such as in contextual-based or object-oriented classification approaches, or textural images.

Integration of Different Sensor Data

Images from different sensors may contain distinctive features in reflecting land-cover surfaces. Data fusion or integration of multisensor data takes advantage of the strengths of distinct image data for improving visual interpretation and quantitative analysis. Many methods have been developed to integrate spectral and spatial information. Solberg, Taxt, and Jain broadly divided data fusion methods into four categories: (1) statistical,

(2) fuzzy logic, (3) evidential reasoning, and (4) neural network. Pohl and van Genderen reviewed data fusion methods, including color-related techniques (e.g., color com- posite, intensity, hue, and saturation [IHS], and luminance and chrominance), statistical/ numerical methods (e.g., arithmetic combination, principal component analysis, high-pass filtering, regression variable substitution, canonical variable substitution, component substitution, and wavelets transforms), and various combinations of these methods. A recent review paper by Zhang further overviewed multisource data fusion techniques and discussed their trends. Li, Li, and Gong discussed the measures based on multivariate statistical analysis to evaluate the quality of data fusion results. In general, data fusion involves two major procedures: (1) geometric coregistration of two data sets and (2) mixture of spectral and spatial information contents to generate a new data set that contains the enhanced information from both data sets. Accurate registration between the two data sets is extremely important for precisely extracting information contents from both data sets, especially for line features such as roads and rivers. Radiometric and atmospheric calibrations are also needed before multisensor data are merged.

Use of Multitemporal Data

Temporal resolution refers to the time interval in which a satellite revisits the same location. A higher temporal resolution provides better opportunities to capture high-quality images. This is particularly useful for areas such as moist tropical regions, where adverse atmospheric conditions regularly occur. The use of remotely sensed data collected over different seasons has proven useful in improving classification accuracy, especially for crop and vegetation classification. For example, Lunetta and Balogh compared single- and two-date Landsat-5 TM images (spring leaf-on and fall leaf-off images) for wetland mapping in Maryland and Delaware, and found that multitemporal images provided better classification accuracies than single-date imagery by itself. An overall classification accuracy of 88% was achieved from multitemporal images, compared with 69% from single-date imagery.

Use of Ancillary Data

Ancillary data, such as topography, soils, roads, and census data, may be combined with remotely sensed data to improve classification performance. Harris and Ventura and Williams suggested that ancillary data may be used to enhance image classification in three ways: (1) preclassification stratification, (2) classifier modification, and (3) postclassification sorting. Since land-cover distribution is related to topography, topographic data have proven to be valuable in improving land-cover classification accuracy in mountainous regions, and topographic data are useful at all three stages of image classification as (1) a stratification tool in preclassification, (2) an additional channel during classification, and (3) a smoothing means in postclassification. In urban studies, DEM data are rarely used to aid image classification due to the fact that urban regions are often located in relatively flat areas. Instead, data related to human systems such as population distribution and road density are frequently incorporated in urban classifications. As discussed in Section 9.2.7, GIS techniques play an important role in the effective use of ancillary data in improving land use/cover classification performance.

Case Study for Land-Cover Classification with Landsat Thematic Mapper Imagery

The previous sections have briefly reviewed major steps for image classification and potential measures for improving classification accuracy. The following section provides a case study in the moist tropical region of Brazil for showing how combination of remote sensing-derived variables and original spectral bands improved classification performance.

Research Problem and Objective

Landsat TM imagery is the most common data source for land-cover classification, and much previous research has explored methods to improve classification performance, including the use of advanced classification options such as neural network, extraction and classification of homogeneous objects (ECHO), object-oriented classifiers, decision tree classifier, and subpixel-based methods. However, the role of vegetation indices and textural images in improving land-cover classification performance is still poorly understood, in particular in moist tropical regions such as the Brazilian Amazon. Therefore, we selected Altamira, Pará state, Brazil, as a case study to explore the role of vegetation indices and textural images in improving vegetation classification performance.

Study Area

Altamira is located along the Trans-Amazonian Highway (BR-230) in the northern Brazilian state of Pará. The city of Altamira lies on the Xingu River at the eastern edge of the study area (see Figure 9.2). In the 1950s, an effort was made to attract colonists from northeastern

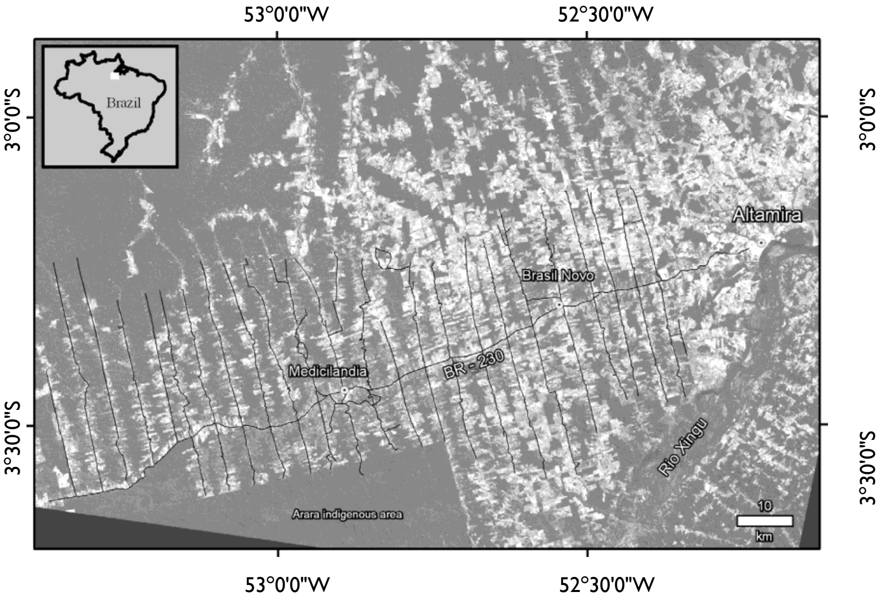

FIGURE 9.2
Altamira of Para state, Brazil, was selected as the area for the case study.

Brazil, who came and settled along streams as far as 20 km from the city center. With the construction of the Trans-Amazonian Highway in 1970, this population and older caboclo settlers from earlier rubber boom eras claimed land along the new highway and legalized their land claims. Early settlement was driven by geopolitical goals of settling in the northern region of Brazil and by political economic policies aimed at shifting production of staples like rice, corn, and beans from the southernmost Brazilian states to the northern region. The uplands have a somewhat rolling topography, with highest elevation measuring approximately 350 m. Floodplains along the Xingu are flat, with the lowest elevation measuring approximately 10 m. Nutrient-rich alfisols and infertile ultisols and oxisols are found in the uplands of this area. The overall soil quality of this area is above-average fertility for Amazonia. The dominant native types of vegetation are mature moist forest and liana forest. Major deforestation in the area, began in 1972, which was concurrent with the construction of the Trans-Amazonian Highway (Moran 1981). Deforestation has led to a complex composition of different vegetation types in this area, such as different secondary succession stages, pasture, and agroforestry. Annual rainfall in Altamira is approximately 2000 mm and is concentrated during the period from late October through early June; the dry period occurs between June and September. The average temperature is about 26°C.

Methods

After the research problems were clearly identified, research objectives were defined, and the study area was selected, the next step was to design a feasible classification procedure, which may include reference data collection for use as training samples, development of suitable variables from the selected remote sensing data, selection of a suitable classification algorithm, and evaluation of the classified image.

Data Collection and Preprocessing

Sample plots for different land covers, especially for different stages of secondary succession and pasture, were collected during the summer of 2009 in the Altamira study area. Prior to fieldwork, candidate sample locations of complex vegetation areas were identified in the laboratory. In each sample area, the locations of different vegetation-cover types were recorded using a global positioning system (GPS) device, and detailed written descriptions and photographs of vegetation stand structures (e.g., height, canopy cover, species composition) were recorded. Sketch-map forms were used in conjunction with small field maps showing the candidate sample locations on A4 paper to note the spatial extent and patch shape of vegetation-cover types in the area surrounding the GPS point. Following the fieldwork, GPS points and field data were edited and processed using GIS and remote sensing software to create representative area of interest (AOI) polygons to be used for image classification. The AOI polygons were created by identifying areas of uniform pixel reflectance in an approximate 3 × 3 pixel window size on the Landsat TM imagery. A land-cover classification system was designed based on our research objectives, compatibility with our previous research work and field surveys. The land-cover classification system included three forest classes (upland, flooding, and liana), three succession stages (initial, intermediate, and advanced stages, or SS1, SS2, and SS3), pasture, and four nonvegetated classes (water, wetland, urban, and burn scars).

A Landsat-5 TM image acquired on July 2, 2008 was geometrically registered to a previously corrected Landsat TM image with a geometric error of less than half a pixel. The nearest-neighbor resampling algorithm was used to resample the TM imagery to a pixel size of 30 × 30 m. An improved image-based DOS model was used to perform radiometric and atmospheric correction. The gain and offset for each band and solar elevation angle were obtained from the image header file. The path radiance was identified based on clear water for each band.

Selection of Suitable Vegetation Indices

Many vegetation indices have been used for different purposes, such as estimation of biophysical parameters. Lu et al. examined the relationships between vegetation indices and forest stand structure attributes such as biomass, volume, and average stand diameter in different biophysical conditions in the Brazilian Amazon. In this research, they found that vegetation indices with TM band 5 had higher correlation coefficients than those without band 5, such as normalized difference vegetation index (NDVI), in study areas like Altamira with complex forest stand structure. Therefore, in this research, different vegetation indices, including band 5, were designed, as well as other indices as summarized in Table 9.1. In order to identify suitable vegetation indices for improving vegetation classification performance, training sample plots for different vegetation types based on field surveys were selected for conducting separability analysis with the transformed divergence. Individual vegetation indices and a combination of two or more indices were explored. When different combinations of two or more indices

TABLE 9.1

Vegetation Indices Used in Research

Sl. No.	Vegetation Index	Equation
1	TC1	0.304TM1 + 0.279TM2 + 0.474TM3 + 0.559TM4 + 0.508TM5 + 0.186TM7
2	TC2	−0.285TM1 − 0.244TM2 − 0.544TM3 + 0.704TM4 + 0.084TM5 − 0.180TM7
3	TC3	0.151TM1 + 0.197TM2 + 0.328TM3 + 0.341TM4 − 0.711TM5 − 0.457TM7
4	ASVI	$((2NIR+1) - \sqrt{(2NIR+1)^2 - 8(NIR - 2RED+BLUE)})/2$
5	MSAVI	$((2NIR+1) - \sqrt{(2NIR+1)^2 - 8(NIR - 2RED)})/2$
6	ND4_2	(TM4 − TM2)/(TM4 + TM2)
7	ND4_25	(TM4 − TM2 − TM5)/(TM4 + TM2 + TM5)
8	ND42_53	(TM4 + TM2 − TM5 − TM3)/(TM4 + TM2 + TM5 + TM3)
9	ND42_57	(TM4 + TM2 − TM5 − TM7)/(TM4 + TM2 + TM5 + TM7)
10	ND4_35	(TM4 − TM3 − TM5)/(TM4 + TM3 + TM5)
11	ND45_23	(TM4 + TM5 − TM2 − TM3)/(TM4 + TM5 + TM2 + TM3)
12	ND4_57	(2 × TM4 − TM5 − TM7)/(TM4 + TM5 + TM7)
13	NDVI	(TM4 − TM3)/(TM4 + TM3)
14	NDWI	(TM4 − TM5)/TM4 + TM5)

Note: ND = normalized difference; ASVI = atmospheric and soil vegetation index; MSAVI = modified soil adjusted vegetation index; TC = tasseled-cap transform. NIR, RED, and BLUE represent near-infrared, red, and blue band in TM image, that is, TM bands 4, 3 and 1. The ND number represents the TM spectral band.

are tested, standard deviation and correlation coefficients are used to determine the best combination of vegetation indices according to the following equation:

$$\text{Best combination} = \sum_{i=1}^{n} \mathrm{STD}_i \Big/ \left| \sum_{j=1}^{n} R_{ij} \right| \tag{9.1}$$

where STD_i is the standard deviation of the vegetation index image i, R_{ij} is the correlation coefficient between two vegetation index images i and j, and n is the number of vegetation index images.

Selection of Suitable Textural Images

Many texture measures have been developed and textural images have proven useful in improving land-cover classification accuracy. Of the many texture measures, gray-level co-occurrence matrix (GLCM)-based textural images have been extensively used in image classification. Lu explored the roles of textural images in biomass estimation and found that textural images based on variance with TM band 2 and a window size of 9 × 9 had a significant relationship with biomass. In another study, Lu and his colleagues explored textural images in vegetation classification and found that textural images based on entropy, second moment, dissimilarity, and contrast, with window sizes of 7 × 7 or 9 × 9, exhibit better performance. Therefore, in our research, GLCM-based texture measures such as variance, homogeneity, contrast, dissimilarity, and entropy were explored with a window size of 9 × 9 and Landsat TM bands 2, 3, 4, 5, and 7. Separability analysis with transformed divergence based on selected training sample plots of different vegetation classes was used for the selection of a potential single textural image or a combination of two or more textural images. The analysis of correlation and standard deviation of each textural image was used to identify the best combination according to Equation 9.1.

Land-Cover Classification

Maximum likelihood classification (MLC) is the most common parametric classifier that assumes normal or near-normal spectral distribution for each feature of interest and an equal prior probability among the classes. This classifier is based on the probability that a pixel belongs to a particular class. It takes the variability of classes into account by using the covariance matrix. A detailed description of MLC can be found in many. In our research, MLC was used to conduct land-cover classification based on different scenarios, in order to explore the roles of vegetation indices and textural images in improving land-cover, especially vegetation classification in the moist tropical region. The scenarios included the consideration of six TM spectral bands, a combination of spectral and vegetation indices, a combination of spectral and textural images, and a combination of spectral indices, vegetation indices, and textural images. These classification results were analyzed based on accuracy assessment.

Accuracy Assessment

Accuracy assessment is often required for a land-cover classification. A common method for accuracy assessment involves the use of an error matrix, for which the literature has provided the meanings of and calculation methods for overall accuracy, producer's accuracy, user's accuracy, and kappa. In this study, a total of 338 test sample plots were used for accuracy assessment. An error matrix was developed for each classification scenario, and then producer's accuracy and user's accuracy for each class and overall accuracy and kappa coefficient for each scenario were calculated based on the corresponding error matrix.

Results

This section provides the analysis of the identified vegetation indices and textural images and compared the classified results with MLC based on different scenarios.

Identification of Vegetation Indices and Textural Images

Since the classification of vegetation is especially difficult in our research, the selection of vegetation indices or textural images is essential to enhance vegetation separability, especially for different types of forest and secondary succession stages. Therefore, three forest types (upland forest, flooding forest, and liana forest), three succession stages (initial, intermediate, and advanced succession stages, or SS1, SS2, and SS3), and pasture were selected. The separability analysis indicated that the best single vegetation index includes ND4-25, TC2 (TC stands for tasseled cap), ND42-53, ND4-35, and TC3, and the best single textural images are from the dissimilarity on TM bands 2 or 3 (TM2-DIS, TM3-DIS), contrast on TM band 2 (TM2-CON), and homogeneity on TM bands 2 or 3 (TM2-HOM or TM3-HOM). However, no single individual vegetation index or textural image could separate the vegetation types. According to the separability analysis and the best combination model, a combination of two vegetation indices or two textural images provided the best results for vegetation separability. Three or more vegetation indices or textural images did not significantly improve vegetation separability; a similar conclusion was reached in our previous research. Therefore, the best combination for two vegetation indices is TC2 and ND42-57, and the best combination for two best textural images is TM2-DIS and TM4-DIS (dissimilarity based on TM bands 2 and 4). Figure 9.3 provides the comparison of TM spectral bands, two selected vegetation indices, and two textural images, showing the different features for vegetation types, especially the textural images.

Comparison of Classification Results

The comparison of accuracy assessment among different scenarios (see Table 9.2) indicated that although the incorporation of vegetation indices into spectral bands has a limited role in improving vegetation classification performance, it is helpful in improving the extraction and separability of pasture, water, and urban land covers; in contrast, the incorporation of textural images into spectral bands was valuable for improving vegetation classification performance, especially for upland forest, flooding forest, and intermediate and advanced succession classes. This research indicates that the incorporation of both

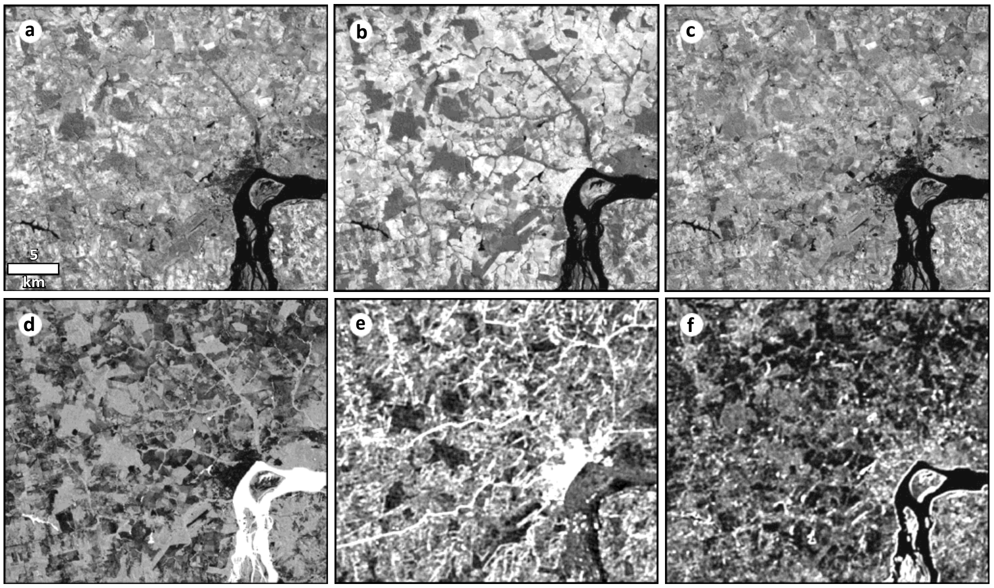

FIGURE 9.3
A comparison of thematic mapper (TM) bands 4 and 5, two vegetation indices, and two textural images. (a) and (b) TM bands 4 and 5; (c) and (d) the second component from tasseled cap transformation and the vegetation index based on bands 4, 2, 5, and 7; and (e) and (f) textural images based on dissimilarity on band 2 and band 4 and a window size of 9 × 9 pixels.

TABLE 9.2
Comparison of Accuracy Assessment Results with MLC among Different Scenarios

	6SB		6SB and 2VI		6SB and 2TX		6SB and 2VI and 2TX	
Land-Cover Types	**PA**	**UA**	**PA**	**UA**	**PA**	**UA**	**PA**	**UA**
Upland forest	37.04	95.24	24.07	92.86	66.67	78.26	66.67	78.26
Flooding forest	93.75	50.00	100.00	41.03	100.00	66.67	100.00	69.57
Liana forest	95.45	66.67	95.45	63.64	81.82	66.67	84.09	69.81
SS1	84.00	61.76	80.00	64.52	92.00	57.50	92.00	58.97
SS2	67.86	90.48	67.86	86.36	78.57	95.65	82.14	92.00
SS3	89.66	74.29	86.21	75.76	79.31	85.19	86.21	89.29
Pasture	83.33	94.83	86.36	95.00	75.76	96.15	77.27	98.08
Water	68.18	100.00	95.45	100.00	72.73	100.00	95.45	100.00
Nonvegetated wetland	53.85	100.00	69.23	90.00	69.23	100.00	53.85	87.50
Urban	100.00	71.05	100.00	100.00	100.00	79.41	100.00	100.00
Burn scars	100.00	87.50	92.86	86.67	92.86	100.00	100.00	87.50
Overall accuracy		77.22		77.51		80.18		82.84
Kappa coefficient		0.7446		0.7485		0.7770		0.8071

6SB represents TM six spectral bands; 6SB and 2VI represent the combination of six spectral bands and two vegetation indices; 6SB and 2TX represent the combination of six spectral bands and two textural images; and 6SB and 2VI and 2TX represent the combination of six spectral bands, two vegetation indices, and two textural images. PA and UA represent producer's accuracy and user's accuracy.

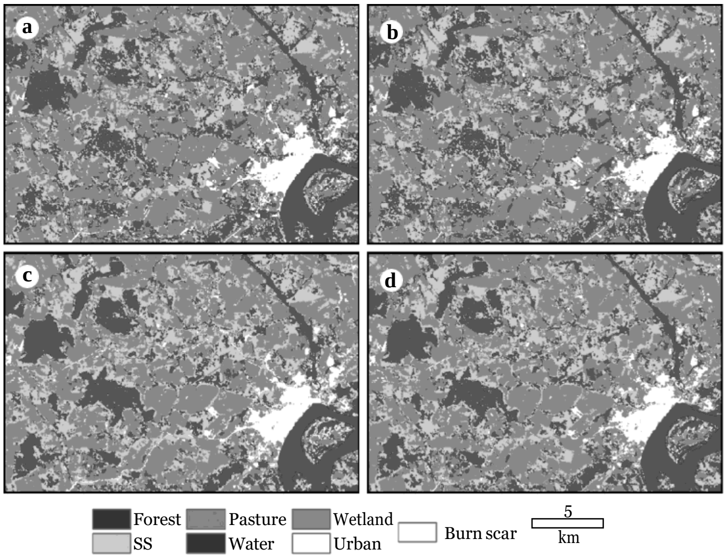

FIGURE 9.4
(See color insert following page 426.) Comparison of classification results among different scenarios with the maximum likelihood classifier: (a) six Thematic Mapper spectral bands, (b) combination of spectral bands and two vegetation indices, (c) combination of spectral bands and two textural images, and (d) combination of spectral bands, two vegetation indices, and two textural images.

vegetation indices and textural images into spectral bands provides the best classification performance. Figure 9.4 provides a comparison of classification results among the four scenarios. It indicates that the use of textural images can reduce the salt-and-pepper effect in the classification image, which is often produced with the per-pixel-based classification method.

Summary of the Case Study

This study indicates the importance of textural images in improving vegetation classification accuracies. A critical step is to identify suitable textural images that can provide the best separability for specified classes. For the selection of a single textural image, one can select the textural image with the highest separability, but for the selection of two or more textural images, a method based on comparing the standard deviation and correlation coefficients between the images provides an easy way to identify a suitable combination.

Final Remarks

Image classification has made great progress over the past decades in the following three areas: (1) development and use of advanced classification algorithms, such as subpixel, per-field, and knowledge-based classification algorithms; (2) use of multiple remote sensing features, including spectral, spatial, multitemporal, and multisensor information; and (3) incorporation of ancillary data into classification procedures, including such data as topographic, soils, roads, and census data. Spectral features are the most important information required for image classification. As spatial resolution increases, how to effectively use the spatial information inherent in the image becomes an important question to be considered. Thus, object-, texture-, or contextual-based methods have attracted increased attention. Classification approaches may vary with different types of remote sensing data. In high spatial resolution data such as those from IKONOS and QuickBird, the high spectral variation within the same land- cover class poses a challenge. A combination of spectral and textural information and the use of per-field or object-oriented classification algorithms can reduce this problem. For medium and coarse spatial resolution data, mixed pixels are a problem, resulting in poor area estimation for classified images when per-pixel classifiers are used. Thus, subpixel features from spectral mixture analysis or fuzzy membership have been used in image classification. Moreover, image data have been integrated with ancillary data as another means for enhancing image classification in which GIS plays an important role. When multisource data are used in a classification, parametric classification algorithms such as MLC are typically not appropriate. Advanced nonparametric classifiers, such as neural network, decision tree, and evidential reasoning, or the knowledge-based approach appear to be the most appropriate choices.

The success of an image classification depends on many factors. The availability of high-quality remotely sensed imagery and ancillary data, design of a proper classification procedure, and skills and experiences of the analyst are most important. For a particular study, it is often difficult to identify the best classifier due to a lack of guidelines for classifier selection and the unavailability of suitable classification algorithms at hand. Comparative studies of different classifiers are thus frequently conducted. Moreover, the combination of different classification approaches has been shown to be helpful for improving classification accuracy. Future research is necessary to develop guidelines for the applicability and capability of major classification algorithms.

Chapter 4

Thermal Remote Sensing of Urban Areas: Theoretical Backgrounds and Case Studies

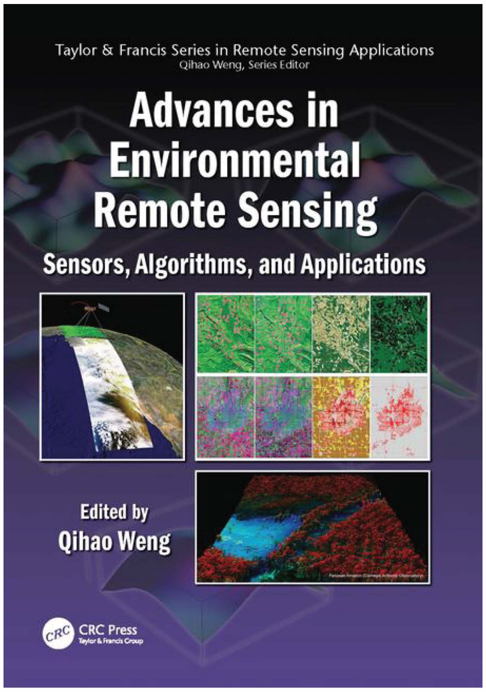

Advances in Environmental Remote Sensing: Sensors, Algorithms, and Applications

By Qihao Weng

© 2011 Taylor & Francis Group. All rights reserved.

To purchase a copy, click here.

Relationship between Land-Surface Temperature and Vegetation Abundance

The LST is an important parameter in urban thermal environment and dynamics studies. This parameter modulates the air temperature of the lower layer of the urban atmosphere, and is a primary factor in determining surface radiation and energy exchange, internal climate of buildings, and human comfort in cities. The physical properties of various types of urban surfaces, their color, the sky view factor, street geometry, traffic loads, and anthropogenic activities are important factors that determine LSTs in urban environments. The LST of urban surfaces corresponds closely to the distribution of land use and land-cover (LULC) characteristics. To study urban LSTs, some sophisticated numerical and physical models have been developed, including energy balance models, laboratory model, three-dimensional (3D) simulations, Gaussian models, and other numerical simulations. Among these models and simulations, statistical analysis plays an important role in linking LST to surface characteristics, especially at larger geographic scales. Previous studies have linked LST to biophysical and meteorological factors, such as built-up area and height, urban and street geometry, LULC, and vegetation, as well as population distribution and the intensity of human activities. However, it is the relationship between LST and various vegetation indices that has been the most extensively documented in the literature.

The LST–vegetation index relationship has been used by Carlson, Gillies, and Perry to retrieve surface biophysical parameters, by Kustas et al. to extract subpixel thermal variations, and by Lambin and Ehrlich and Sobrino and Raissouni to analyze land-cover dynamics. Many studies observe a negative relationship between LST and vegetation indices. This finding has pushed research in two major directions: (1) statistical analysis of LST–vegetation abundance relationship and (2) the thermal-vegetation index (TVX) approach. The latter by definition is a multispectral method of combining LST and a vegetation index in a scatter plot to observe their associations.

Statistical Analysis of the Land-Surface Temperature: Vegetation Abundance Relationship

To understand the statistical relationship between LST and vegetation cover, different vegetation indices have been employed in search of a representative index. Goward, Xue, and Czajkowski showed that different spectral vegetation indices, such as normalized difference vegetation index (NDVI) and simple ratio, were related to leaf area index (LAI) and green biomass. For a long time now, NDVI has been used to quantify vegetation patterns and dynamics within cities, and has been incorporated with LST to measure the impacts of urbanization. The relationship between NDVI and fractional vegetation cover (Fr) is not singular. Small suggested that NDVI did not provide areal estimates of the amount of vegetation. The NDVI measurements are a function of the visible and near- infrared reflectance from the plant canopy, reflectance of the same spectra from the soil, and atmospheric reflectance, and they are subject to the influence of errors related to observational and other errors. Plant species, leaf area, soil background, and shadow can all contribute to NDVI variability. The relationship between NDVI and other measures of vegetation abundance (e.g., LAI values greater than 3) is well known to be nonlinear. This nonlinearity and the platform dependency of NDVI suggest that this index may not be a good indicator for quantitative analyses of vegetation, and the relationship between NDVI and LST needs further calibration. More quantitative, physically based measures of vegetation abundance are called for, especially in applications that require biophysical measures. The importance of spatial resolution for detecting landscape patterns and changes should also be emphasized, and the relationship between NDVI variability and pixel size should be further investigated.

More recent investigations are directed at finding a surrogate to NDVI. Weng, Lu, and Schubring derived the vegetation fraction at different scales (pixel aggregation levels), made a comparison between NDVI and vegetation fraction in terms of their effectiveness as an indicator of urban thermal patterns, and found a stronger negative correlation between vegetation fraction and LST than between NDVI and LST. Yuan and Bauer made a similar correlation analysis between impervious surface area (ISA) and NDVI, suggested that ISA showed higher stability and lower seasonal variability, and recommended it as a complementary measure to NDVI. Xian and Crane sup- ported the aforementioned observations by suggesting that the combined use of ISA, NDVI, and LST can explain temporal thermal dynamics across cities.

Thermal-Vegetation Index Approach to the Land-Surface Temperature–Vegetation Relationship

The combination of LST and NDVI by a scatter plot results in a triangular shape. Several methods have been developed to interpret the LST–NDVI space, including the "triangle" method using a "soil–vegetation–atmosphere transfer" (SVAT) model, in situ measurement method, and remote sensing–based method. However, difficulties still exist in interpreting LST for sparse canopies because the measurements combine the temperature of the soil and that of vegetation, and the combinations are often nonlinear. Different versions of the TVX approach have been developed over the past decades. Price found that radiant surface temperature showed more variations in sparsely vegetated areas than in densely vegetated areas. This behavior results in the atypical triangular shape or, as observed by Moran et al., in a trapezoidal shape for large heterogeneous regions under conditions of strong sunlight. In Chapter 19, Carlson and Petropoulos provide a comprehensive review of the triangle method for estimating surface evapotranspiration and soil moisture. The slope of the LST–NDVI curve has been related to soil moisture conditions, the evapotranspiration of the surface, and other applications in shaping the TVX concept. Ridd and Carlson, Gillies, and Perry interpreted different sections of the triangle and related them to different LULC types. Lambin and Ehrlich presented a comprehensive interpretation of the TVX space. Carlson and Arthur gave a physical meaning to the TVX space. Further, Goward, Xue, and Czajkowski provided a detailed analysis of the underlying biophysics of the observed TVX relationship, and suggested that the relationship was the result of modulation of radiant surface temperature by vegetation cover. The TVX approach was the subject of studies focusing on the development of new applications, and the patterns and dynamics of different vegetation types at all scales from local to global. Researchers used the TVX concept to develop new indices and estimated parameters. Moran et al. used the TVX trapezoid to develop a new index called a "water-deficit index" (WDI) to estimate evapotranspiration in the absence of meteorological data using the difference between surface and air temperatures. Lambin and Ehrlich proposed radiant surface temperature—NDVI ratios in the TVX space—and showed its usefulness in land-cover mapping. Owen, Carlson, and Gillies used the same space and suggested a land-cover index (LCI) for assessing UHI. Carlson and Arthur extended the TVX approach to calculate ISA and surface runoff. Jiang and Islam, by linear decomposition of TVX scatter plot, estimated the "α" parameter of the Priestly– Taylor equation in the absence of ground meteorological data. Sandholt, Rasmussen, and Andersen proposed a "temperature-vegetation dryness index" (TVDI) based on the relationship between surface temperature and NDVI, and showed the effectiveness of TVDI by explaining larger spatial variations better than hydrologic models. Nishida et al. estimated evapotranspiration fraction (EF) using a new TVX algorithm to provide global time-series coverage of EF from MODIS data. Chen et al. investigated the relationship between temperature and various newly developed indices, and found that NDVI presented a limited range.

Apart from the introduction of new indices, much research has been carried out in the extraction of new TVX metrics. Several studies have focused on the slope of the LST–NDVI fit line. Variations in slope and intercept of the TVX space have been interpreted in relation to surface parameters. Nemani and Running related the slope of the TVX correlation to the stomatal resistance and evapotranspiration in a deciduous forest. Sandholt, Rasmussen, and Andersen linked TVX correlation slope to the evapotranspiration rate and used this relationship to estimate air temperature. The TVX concept has further been used to anaylze pixel trajectories. The idea emerged over the past decade that land- surface parameters associated with individual pixels can be visualized as vectors tracing out paths in a multiparameter space. Several studies verified that urbanization is the major cause of the observed migration of pixels within the TVX space. Owen, Carlson, and Gillies found that the initial location of the migrating pixels in the TVX triangle determined the magnitude and direction of the path. Carlson and Sanchez-Azofeifa used the TVX method to assess how surface climate was affected by rapid urbanization and deforestation in San Jose, Costa Rica. They found that urbanization was more effective in causing changes in surface climate than deforestation, and that different development styles followed different paths in the space. Carlson and Arthur compared average trajectories of different development styles, and showed that in the advanced stages of development, the paths come closer and indistinguishable from one another.

Finally, the TVX approach has been used in the so-called triangle inversion method to derive surface parameters. Carlson, Gillies, and Perry used an SVAT model to show the feasibility of extracting surface parameters such as soil moisture content and Fr from the analysis of the TVX space without ground data. This inversion method was used to impose physical limits on a solution of the SVAT model parameterized for a test site to remotely sense variables used in the model to derive surface biophysical variables. Gillies et al. verified that the borders of the triangle constrained the solutions for determining surface energy fluxes. Goward, Xue, and Czajkowski used the TVX approach as a means for assessing soil moisture conditions from satellite data. Owen, Carlson, and Gillies used this method to assess the impacts of urbanization on surface parameters. Some authors, however, have drawn attention to the problems presented by the TVX space. Goward, Xue, and Czajkowski showed that plant stomatal function confused the interpretation of the TVX space given by experimental studies to use TVX slope to assess soil moisture conditions. Nishida et al. discussed four main difficulties of the TVX method used for evapotranspiration (ET) estimation: (1) the method's dependency on meteorological data, (2) computational difficulties encountered in the inversion of numerical models on a global scale, (3) problems involved in accurate estimation in dense vegetation, and (4) estimation difficulties faced in complex landscapes. While trying to establish guidelines in order to overcome the aforementioned problems by a new model, they suggested their model was effective for urbanization monitoring since EF is able to capture variations in surface energy partitioning.

Case Study: TVX Space and Its Temporal Trajectory Analysis in Tabriz, Iran, Using Landsat TM/ETM+ Images

Amiri et al. examined the spatial and temporal dynamics of LST in relation to LULC change in the TVX space by using Landsat TIR and reflective data. A methodology was developed to detect and monitor urban expansion and to trace the changes in biophysical parameters such as NDVI and LST resulting from changes in LULC. The Tabriz metropolitan area (38°05′, 46°17′) in Iran was selected as the study area. Multitemporal images acquired by Landsat 4 TM, Landsat 5 TM, and Landsat 7 ETM+ sensors on June 30, 1989, August 18, 1998, and August 2, 2001, respectively, were processed to extract LULC classes and LST. The relationship between the temporal dynamics of LST and LULC was then examined. The TVX space was constructed in order to study the temporal variability of thermal data and vegetation cover.

Figure 6.1a shows the Fr/T^* scatter plot (TVX space) with sample LULC classes based on the Landsat TM image of August 18, 1998. To create the plot, the cloud-contaminated pixels were first excluded. The NDVI values were rescaled between bare soil ($NDVI_0$) and dense vegetation ($NDVI_S$), following a method suggested by Owen, Carlson, and Gillies. The Fr was then calculated as the square of the rescaled value N*. Areas with high and low temperatures (T_{max} and T_0) were selected from the bare and wet soils, respectively, and their data were used to calculate the normalized temperature values of T*. The resulting Fr/T^* scatter plot showed a typical triangular pattern, with a clear "warm edge" defined by the right side of the pixel envelope.

The temporal trajectory of pixels in the TVX space made it possible to observe most changes due to urbanization as the pixels migrated from the low-temperature dense

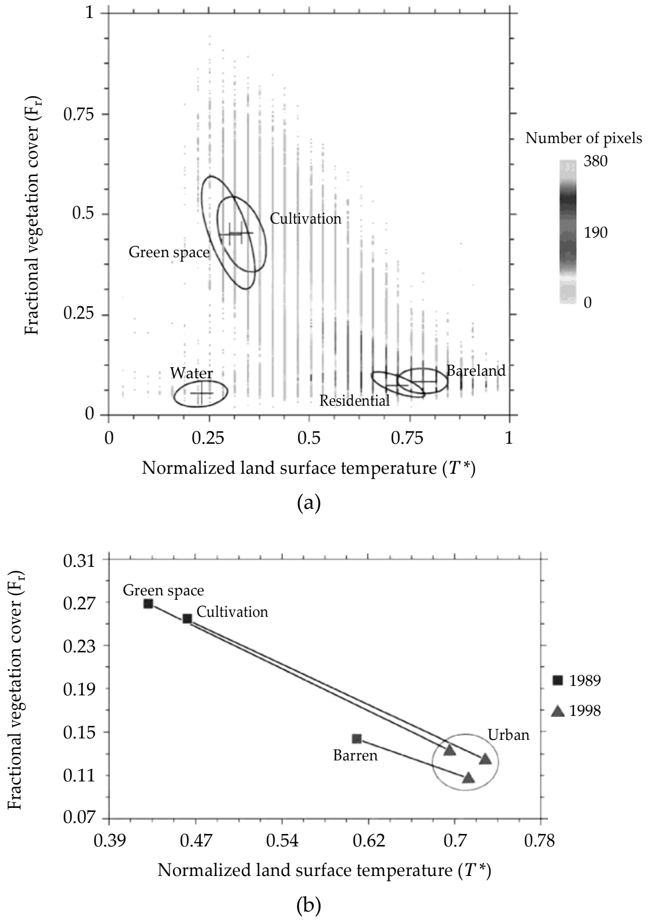

FIGURE 6.1

(See color insert following page 426.) Fractional vegetation cover (Fr)/*T** scatter plot (thermal-vegetation index [TVX] space) with sample land use and land-cover (LULC) classes from a Landsat thematic mapper (TM) image of the city of Tabriz and change trajectory in the TVX space for a specific period: (a) The scatter plot with sample LULC classes from a Landsat TM image of Tabriz (38°05′, 46°17′) in northwestern Iran, which was acquired on August 18, 1998; (b) change trajectory in the TVX space for a long (1989–1998) period (June 30, 1989–August 18, 1998). The vectors show the magnitude of change associated with LULC change from green space, cultivation, and barren pixels to urbanized pixels.

vegetation condition to the high-temperature sparse vegetation condition in the TVX space (Figure 6.1b). Our result further showed that in the late stages of urbanization, affected pixels tend to converge and entirely lose their initial characteristics in the TVX space. The uncertainty analysis revealed that trajectory analysis in the TVX space involved a class-dependant noise component. This uncertainty emphasized the need for multiple LULC control points in the TVX space. In addition, this case study suggests that the use of multitemporal satellite data together with the examination of changes in the TVX space is effective and useful in urban LULC change monitoring and analysis of urban surface temperature conditions as long as the uncertainty issue is addressed.

Use of Remotely Sensed Data to Characterize and Model Urban Heat Islands

Background

Remotely sensed TIR data is a unique source of information in defining surface heat islands, which are related to canopy layer heat islands. In situ data (in particular, permanent meteorological station data) offers a high temporal resolution and long-term coverage but lacks spatial details. Observations and measurements by moving vehicles overcome this limitation to some extent, but do not provide a synchronized view over a city. Only remotely sensed TIR data can provide a continuous and simultaneous view of the whole city, which is of prime importance in the detailed investigation of urban surface climate. Rao was the first to assess the possibility of detecting the thermal footprint of urban areas. Since then, a wide range of TIR sensors have been developed and employed to study LST and UHI; they offer several improvements over their ancestors. However, in many of the previous studies, there is confusion between LST patterns and UHIs. A "satellite-derived" heat island is largely an artifact of the low-spatial-resolution imagery used, and the term "surface temperature patterns" is more meaningful than surface heat island. It remains a valid scientific issue how satellite-derived LSTs can be utilized to derive UHI parameters, and to model and simulate the UHI over space and time.

Previous studies of urban thermal landscapes and UHIs have been conducted using National Oceanic and Atmospheric Administration (NOAA) AVHRR data. However, for all these studies, the 1.1-km spatial resolution AVHRR data were found suitable only for large-area urban temperature mapping and not for establishing accurate and meaningful relationships between image-derived values and those measured on the ground. The 120-m resolution Landsat TM (and later ETM+ data of 60-m resolution) TIR data have also been extensively utilized to derive LSTs and to study UHIs. Carnahan and Larson used the TM TIR data to observe mesoscale temperature differences between urban and rural areas in Indianapolis, Indiana, whereas Kim studied similar phenomena in Washington, DC. Nichol utilized TM TIR data to monitor microclimate for housing estates in Singapore, and further calculated LSTs of building walls based on a 3D geographic information system (GIS) model. Weng examined LST patterns and their relationships with land cover in Guangzhou and in the urban clusters in the Pearl River Delta of China. Weng, Lu, and Schubring utilized a Landsat ETM+ image to examine the LST–vegetation abun- dance relationship in Indianapolis. More recently, Lu and Weng applied spectral mixture analysis (SMA) to ASTER images in order to derive hot-object and cold-object fractions from the TIR bands of the sensor and biophysical variables from the nonthermal bands. Statistical analyses were then conducted to examine the relationship between LST and the derived fraction variables across the resolution from 15 to 90 m.

The most recent advances include development and utilization of quantitative surface descriptors for assessing the interplay between urban material fabric and urban thermal behavior. Moreover, the landscape ecology approach was employed to assess this interplay across various spatial resolutions and to identify the operational scale at which both LST and LULC processes interacted to generate the urban thermal landscape patterns. Because an ASTER sensor collects both daytime and nighttime TIR images, analysis of LST spatial patterns has also been conducted for a diurnal contrast.

A key issue in the application of TIR remote-sensing data in urban climate studies is the use of LST measurements at the microscale to characterize and quantify UHIs observed at the mesoscale. Streutker used AVHRR data to quantify the UHI of Houston, Texas, as a continuously varying two-dimensional (2D) Gaussian surface superimposed on a planer rural background, and derived the UHI parameters of magnitude (i.e., intensity), spatial extent, orientation, and central location. Rajasekar and Weng applied a nonparametric model by applying fast Fourier transformation (FFT) to MODIS imagery for characterization of the UHI over space, so that UHI magnitude and other parameters may be derived. Despite these advances, estimation of UHI parameters from multitemporal and multilocation TIR imagery still remains a promising research direction and will continue to be so in the years to come, given the increased interest of the urban climate community in using remote-sensing data.

Case Study: Characterizing an Urban Heat Island in Beijing, China, Using Advanced Spaceborne Thermal Emission and Reflection Radiometer Images

This section briefly introduces a method for characterizing UHIs using remotely sensed LST data and explains its application in Beijing, China. Higdon explained the process convolution for a one-dimensional (1D) process and made suggestions for its extension to two or three dimensions. In this case study, the process convolution model was extended to model the UHI of Beijing as a 2D Gaussian process using ASTER LST data. The procedure is detailed next.

Let $y_{(1,1)}, \ldots, y_{(i,j)}$ (where q is a 2D matrix of (1,1), …, (i,j)) be data recorded over the 2D spatial locations $s_{(1,1)}, \ldots, s_{(i,j)}$ in S. In this research, the spatial method represents data as the sum of an overall mean μ, a spatial process $z = (z_{(1,1)}, \ldots, z_{(i,j)})^T$, and Gaussian white noise $\varepsilon = (\varepsilon_{(1,1)}, \ldots, \varepsilon_{(i,j)})^T$ with variance $\sigma^2{}_{\varepsilon}$:

$$y = s + z + \varepsilon \tag{6.1}$$

Here, the elements of z are the restriction of the spatial process $z(s)$ to the 2D data locations $s_{(1,1)}, \ldots, s_{(i,j)}$; $z(s)$ is defined to be a mean zero Gaussian process. But rather than specifying $z(s)$ through its covariance function, it is determined by the latent process $x(s)$ and the smoothing kernel $k(s)$. The latent process $x(s)$ is restricted to be nonzero at the 2D spatial sites $\omega_{(1,1)}, \ldots, \omega_{(a,b)}$, also in S, and $x = (x_{(1,1)}, \ldots, x_{(a,b)})^T$ where $x\omega_p = x(\omega_p)$; $p = (1,1), \ldots, (a,b)$. Each x_p is then modeled as an independent draw from an $N(0,\sigma^2{}_{\omega})$ distribution. The resulting continuous Gaussian process is then

$$z(S) = \sum_{p=(1,1)}^{(a,b)} X_j k(s - \omega_p) \tag{6.2}$$

where $k(s - \omega_p)$ is a kernel centered at ω_p. This gives the following linear model:

$$y = \mu l_{(i,j)} + Kx + \varepsilon \tag{6.3}$$

where $l_{(i,j)}$ is the (i,j)th vector of ls; the elements of K are given by

$$K_{pq} = k(s_p - \omega_q)x_q \tag{6.4}$$

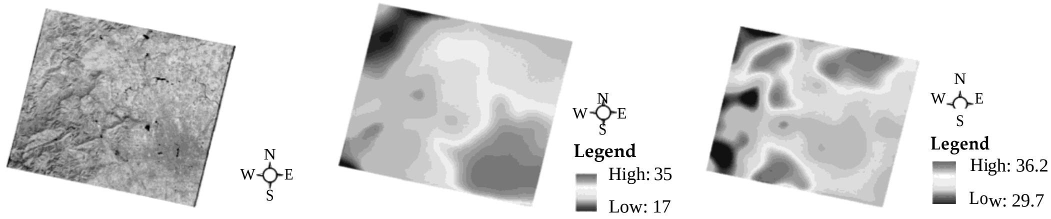

(a) ASTER true color composite (b) August 31, 2004 (c) April 9, 2004

FIGURE 6.2
(See color insert following page 426.) The results of kernel convolution for two advanced spaceborne thermal emission and reflection radiometer (ASTER) images of Beijing: (a) A true color composite of Beijing using ASTER acquired on August 31, 2004; (b) and (c) the results of convoluted images (with a smoothing parameter of 0.6) showing thermal landscape pattern of Beijing on August 31, 2004 and April 9, 2004, respectively. The temperature is given in degrees Celsius.

$$x \sim N(0, \sigma^2{}_x l_{(a,b)}) \text{ and } \tag{6.5}$$

$$\varepsilon \sim N(0, \sigma^2{}_x l_{(i,j)}) \tag{6.6}$$

The results of convolution modeling can then be analyzed for patterns over space and time. The results of the kernel convolution can be compared to examine how UHI magnitude, center, and spatial extent change over space and time. In order to determine UHI magnitude, the mean temperature value within each image is considered as a background temperature and all values less than the mean are brought to the same level.

Figure 6.2 shows the results of kernel convolution (with a smoothing parameter of 0.6) for two ASTER images of Beijing acquired on August 31, 2004 and April 9, 2004, respectively. The August image clearly displays a UHI (Figure 6.2a) with a magnitude of 7°C. The built-up area had a higher temperature than the surrounding rural areas, and there was a temperature gradient from the urban areas in the southeastern corner to the mountainous area in the northwest. In contrast, the April image shows an urban heat sink in central Beijing (Figure 6.2b). According to our computation, the intensity of the heat sink was about 3°C. Higher temperatures corresponded to the three suburban agricultural/residential areas in the north, northwest, and south. The lowest temperature was detected in the western mountainous area.

Estimation of Urban Heat Fluxes Using Remote Sensing Data

Knowledge of urban surface energy balance is fundamental to the understanding of UHIs and urban thermal behavior. Three items of information are needed in order to estimate land surface energy fluxes: (1) energy driving forces (i.e., incident solar energy, albedo, and resulting net radiation), (2) soil moisture availability and the vegetation–soil interaction, and (3) capacity of the atmosphere to absorb the flux, which depends on surface air temperature, vapor pressure gradients, and surface winds. Previous studies have focused on the methods for estimating variables related to the first two items from satellite remote sensing data, but little has been done to estimate the surface atmospheric parameters. These parameters are measured in the traditional way in the network of meteorological stations or by in situ field measurements.

Remote sensing TIR data can be applied to relate LSTs with surface energy fluxes for characterizing landscape properties, patterns, and processes. Remotely sensed thermal imagery has the advantage of providing a time-synchronized dense grid of temperature data over a whole city, whereas optical sensing data have been used to monitor discrete land-cover types and to estimate biophysical variables. Together, remote sensing data can be used to estimate surface parameters related to the soil–vegetation system and surface soil moisture, radiation forcing components, and indicators of the surface's response to them. If the advantage of time-sequential observations of satellite sensors (some sensors can even scan a specific geographic location twice a day—one at daytime and one at nighttime) is considered, remote-sensing data have great potential for studying the urban surface energy budget, as well as the spatial pattern and temporal dynamics of urban thermal landscapes. One of the earliest studies that combined surface energy modeling and remote sensing approaches was conducted by Carlson et al. They used satellite temperature measurements in conjunction with a 1D boundary layer model to analyze the spatial patterns of turbulent heat fluxes, thermal inertia, and ground moisture availability in Los Angeles, CA, and St. Louis, MO. This method was later applied in Atlanta by using AVHRR data, in which the net urban effect was determined as the difference between urban and rural simulations. Because analyses of surface energy flux are extensively conducted over vegetated and agricultural areas, successful methods have been applied to urban areas. Zhang, Aono, and Monji used Landsat TM data, in combination with routine meteorological data and field measurements, to estimate the urban surface energy fluxes in Osaka, Japan, and to analyze their spatial variability in both summer and winter. Chrysoulakis used ASTER imagery, together with in situ spatial data, to determine the spatial distribution of all-wave surface net radiation balance in Athens, Greece. Kato and Yamaguchi combined ASTER and Landsat ETM+ data with ground meteorological data to investigate the spatial patterns of surface energy fluxes in Nagoya, Japan, over four distinct seasons. Furthermore, this study separated anthropogenic heat discharge and natural heat radiation from sensible heat flux.

The seasonal and spatial variability of surface heat fluxes is crucial to the understanding of UHI phenomenon and dynamics, which has not been thoroughly addressed by previous studies. In a recent study, based on the two-source energy balance (TSEB) algorithm, we developed a method to estimate urban heat fluxes by the combined use of multispectral ASTER images and routine meteorological data, and applied it to the city of Indianapolis, for understanding the seasonal changes in the heat fluxes. The ASTER images of the four seasons were acquired and processed with atmospheric, radiometric, and geometric corrections before using them for the analysis. The ASTER data pertaining to surface kinetic temperature, surface spectral emissivity, and surface reflectance (VNIR and SWIR) was used. All the images were resampled to a resolution of 90 m. The nonvegetation and vegetation areas were separated for estimating heat fluxes based on computed NDVI values. The needed meteorological data was obtained from the Indiana State Climate Office, including data regarding shortwave radiation, air temperature, relative humidity, air pressure, and wind speed. Shortwave radiation data was obtained from the National Solar Radiation Database.

Figure 6.3 shows the estimated net radiation, sensible heat flux, latent heat flux, and ground heat flux on October 13, 2006, recorded in Indianapolis. The mean values and standard deviations of the surface heat fluxes by LULC type are displayed in Table 6.1. This study found that the estimated surface heat fluxes showed a strong seasonality, with the highest net radiation recorded in summer, followed by spring, fall, and winter. Sensible heat flux tended to change largely with surface temperature, whereas latent heat was largely modulated by the change in vegetation abundance and vigor over a year and the accompanying moisture condition. The fluctuation in all heat fluxes tended to be high in the summer months and low in the winter months. Sensible and latent heat fluxes showed

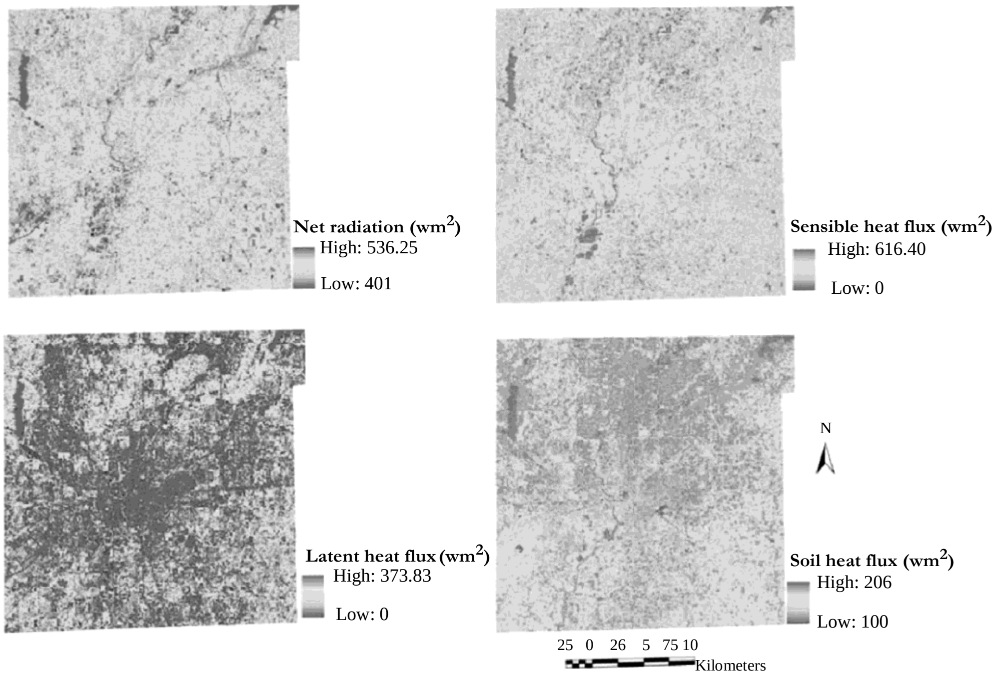

FIGURE 6.3
(See color insert following page 426.) Net radiation, sensible heat flux, latent heat flux, and soil heat flux on October 13, 2006 in Indianapolis estimated by the combined use of advanced spaceborne thermal emission and reflection radiometer image and ground meteorological data.

TABLE 6.1
Statistics of Surface Heat Fluxes by LULC Type in Indianapolis on October 13, 2006 (Unit: W/m^2)

Heat Fluxes	Urban and Built-Up Land	Agricultural Land	Forest Land	Grassland	Water	Bare Ground	Overall
Net	377.87	394.98	426.37	378.76	484.40	363.61	396.47
radiation	(40.97)	(33.30)	(20.15)	(25.99)	(28.61)	(56.88)	(40.73)
Soil	151.15	118.49	63.96	113.63	169.54	109.08	113.09
heat flux	(16.39)	(9.99)	(3.02)	(7.80)	(10.01)	(17.07)	(37.30)
Sensible	293.34	183.35	269.26	243.82	77.49	91.10	242.62
heat flux	(41.95)	(31.91)	(95.34)	(73.24)	(11.86)	(14.51)	(100.31)
Latent	0.94	65.99	63.73	39.67	231.50	150.20	39.53
heat flux	(8.78)	(39.88)	(34.70)	(37.31)	(52.90)	(49.28)	(52.15)

a stronger spatial variability than net radiation and ground heat flux. By computing heat fluxes by LULC type, we further investigated the geographic pattern and spatial variability of urban surface energy balance. The variations in net radiation among the LULC types were found to be attributable mainly to surface albedo and temperature, whereas the within-class variability in turbulent heat fluxes were more associated with changes in vegetation, water bodies, and other surface factors.

Future Prospects of Thermal Infrared Sensors

There has been significant progress in the studies focusing on LST–vegetation relationship, UHI modeling with remotely sensed TIR data, and estimation of urban surface heat fluxes. However urban climate and environmental studies will be difficult, if not impossible, without TIR sensors having a global imaging capacity. At present, there are few sensors that have such TIR capabilities. The TM sensor aboard Landsat 5 has been acquiring images of the Earth nearly continuously from July 1982 to the present, with a TIR band of 120-m resolution, and is thus long overdue. On April 2, 2007, updates to the radiometric calibration of Landsat 5 TM data processed and distributed by the U.S. Geological Survey (USGS) Earth Resources Observation System (EROS) created an improved Landsat 5 TM data product that is now more comparable radiometrically to Landsat 7 ETM+ and provides the basis for continued long- term studies of the Earth's land surfaces. Another TIR sensor that has global imaging capacity is with Landsat 7 ETM+. On May 31, 2003, the ETM+ scan-line corrector (SLC) failed permanently. Although it is still capable of acquiring useful image data with the SLC turned off, particularly within the central part of any given scene, the National Aeronautics and Space Administration (NASA) has teamed up with USGS to focus on the Landsat Data Continuity Mission (LDCM), which is most likely not to have a TIR imager. In addition, Terra's ASTER TIR bands of 90-m resolution have been increasingly used in urban climate and environmental studies in recent years. The ASTER is an on-demand instrument, which means that data are acquired only over requested locations. The Terra satellite, launched in December 1999 as part of NASA's Earth Observing System, has a life expectancy of 6 years, and is now also overdue. The scientific and user community is looking forward to a Landsat ETM–like TIR sensor. The draft requirements for the LDCM thermal imager indicate that two thermal bands (10.3–11.3 μm and 11.5–12.5 μm) of 90 m or better spatial resolution are preferred (for details, readers are referred to the LDCM Web site, http://ldcm.nasa.gov/procurement/TIRimagereqs051006.pdf). The National Research Council Decadal Survey indicates the need for such a TIR sensor. The Hyperspectral Infrared Imager (HyspIRI) is defined as a mission with tier-2 priority to be launched in the next 8–10 years. Because of its hyperspectral visible and shortwave infrared bandwidths and its multispectral TIR capabilities, HyspIRI will be well suited for deriving land-cover and other biophysical attributes for urban climate and environmental studies (for more information, the readers are referred to the HyspIRI Web site, http://hyspiri.jpl.nasa.gov/). Its TIR imager is expected to provide seven bands between 7.5 and 12 μm and one band at 4 μm, all with 60-m spatial resolution. This TIR sensor is intended for the imaging of global land and shallow water (less than 50 m) with a 5-day revisit at the equator (1 day and 1 night imaging). These improved capabilities would allow for a more accurate estimation of

LST and emissivity, and for deriving unprecedented information on biophysical characteristics and even socioeconomic information such as population, quality of life indicators, and human settlements. Such information cannot be obtained from the current generation of satellites devices in orbit, such as MODIS, Landsat, or ASTER. Two major areas of application identified by the HyspIRI science team are urbanization and human health through the combined use of visible to shortwave infrared (VSWIR) and TIR data. Until then, we may have to bear with Landsat and ASTER for medium-resolution TIR data, and MODIS and AVHRR for coarse-resolution data. It is from this perspective that international collaborations on Earth resources satellites become very important.

Chapter 5

Lidar Remote Sensing

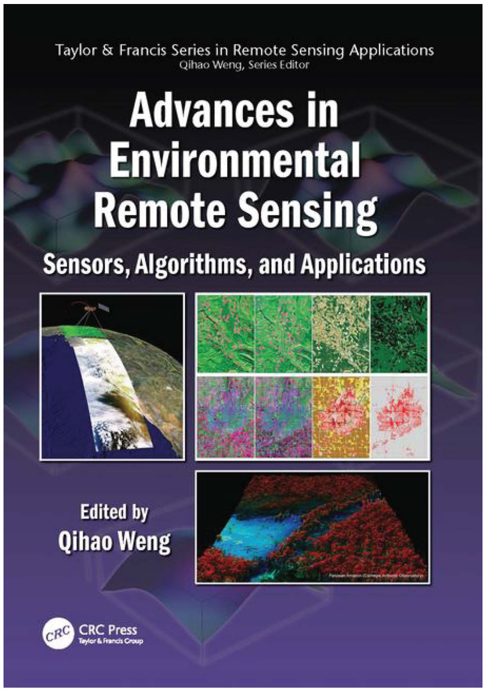

Advances in Environmental Remote Sensing: Sensors, Algorithms, and Applications

By Qihao Weng

© 2011 Taylor & Francis Group. All rights reserved.

To purchase a copy, click here.

3.1 Foundations of Laser Theory

Laser ranging systems are commonly referred to as "lidar" systems. Lidar is an acronym describing light detection and ranging systems, which are sometimes also referred to as "ladar," either from laser detection and ranging or from laser radar. A universally accepted terminology does not exist, but most commonly we refer to these systems as lidar systems, although the spelling of lidar may differ—lidar, LiDAR, or LIDAR.

Lasers have been one of the greatest scientific developments of the twentieth century. After five decades of achievements in this field, lasers are still a symbol of high technology. The word laser is an acronym that summarizes the nature of laser light—light amplification by the stimulated emission of radiation. Therefore, a laser is a special type of light source with certain characteristics related to its wavelength, output power, duration of emission, beam divergence, coherence, and the systems and materials that generate it.

Albert Einstein developed the foundation of stimulated emission of radiation and published his findings in 1916 and 1917. In essence, Einstein demonstrated that atoms can absorb and emit radiation spontaneously and that atoms in certain excited states can be induced to emit radiation. For about 40 years after Einstein's theoretical work on stimulated emission was published, the concept was used only in theoretical discussions and had little relevance in experimental work. The first successful production of stimulated emission was achieved by Charles H. Townes between 1951 and 1953, who was then at Columbia University; he built a device called a "maser"—microwave amplification by the stimulated emission of radiation. This device produced a coherent beam of microwaves. Later, in 1964, Townes shared the Nobel Prize in physics with two other maser pioneers, Nikolai Basov and Aleksander Prokhorov. A collaborator of Townes, Arthur Schawlow, also received the Nobel Prize in physics in 1981 for research done on lasers. However, the winner of the laser invention race, who is accredited with the development of the first ruby laser in 1960, is Theodore H. Maiman, with what was at that time the Hughes Aircraft Corporation research laboratory. The ruby laser is a good example of what we expect a laser to be. The wavelength of the ruby laser is toward the end of the red region of the electromagnetic spectrum, at 694 nm, and it emits coherent waves in short pulses in a concentrated beam of light.

There are many types of lasers. Depending on how they operate, laser sources can emit light in a pulsed mode or as steady beams; the latter are also known as "continuous-wave" (CW) lasers. Laser pulses are characterized by pulse duration and repetition rates. The pulse duration can range from milliseconds to femtoseconds, that is, from 10^{-3} to 10^{-15} seconds. Because the human eye's response is much slower than the laser pulse frequency, some lasers that may look continuous to the eye are actually pulsed lasers.

Lasers can also be differentiated based on power output, which spans a wide range from milliwatts—thousandths of a watt—to kilowatts. Nevertheless, lasers cannot adjust their power output on demand, but they may be able to adjust it over a limited range. Power output is a characteristic of the materials that produce lasers. Moreover, each type of laser-producing material emits laser light with a characteristic wavelength or a range of wavelengths. Table 3.1 presents a list of the most common laser types based on materials

TABLE 3.1

Most Common Laser Types

Laser Material Type	Laser Light Wavelength (nm)
Organic dye dissolved in solvent	300–1000 (tunable laser)
Rare gas ions (e.g., argon ion)	450–530
Helium neon	543 (red), 632.8 (green), 1150 (near-infrared)
Semiconductor	670–680 and 750–900
Nd: YAG	1064 (near-infrared)
Hydrogen fluoride	2600–3000

producing laser light and their wavelengths, in nanometers, although the actual list is much longer with lasers ranging from the ultraviolet region to the microwave region.

How Is Laser Light Generated?

A laser is a light source with unique properties. As the expansion of the acronym suggests, a laser amplifies light signals that stimulate emission of radiation. The stimulated emission occurs in an amplifying medium contained in an optical resonator or cavity, which holds the amplified light and redirects it through the medium for repeated amplifications. A set of two mirrors feed the light back into the amplifier medium. One cavity mirror reflects essentially all of the light back into the amplifying medium, whereas the other mirror transmits a constant fraction of the light, for example, 10%, which becomes the laser beam, and reflects the rest back into the medium.

Laser Light Properties

Laser light has important properties that differentiate it from white or ordinary light, most notably coherence, wavelength and spectral purity, directionality, beam divergence, power modulation, and polarization. Probably the best known property of laser light is coherence.

Coherence of Laser Light

Figure 3.1 illustrates the concept of coherence, when light waves are in phase with one another, which means their peaks are lined up at the same point in time. To have coherent waves, light waves must start with the same phase at the same position, and they also need to have the same wavelength, that is, to be spectrally pure. Perfect coherence is difficult to achieve, and not all types of laser light are equally coherent. Coherence can be characterized as spatial or temporal. Laser light waves may encounter different optical path conditions, which make them drift out of phase. As such, temporal coherence is defined by how long the laser light waves remain in phase as they travel. Spatial coherence measures the area over which light waves are coherent, and it is the essential prerequisite that gives a strong directionality to laser beams. Probably the most fundamental difference between laser light and radiation from other light sources, such as ordinary light, is that laser light has the potential to generate beams with very high temporal and spatial coherence.

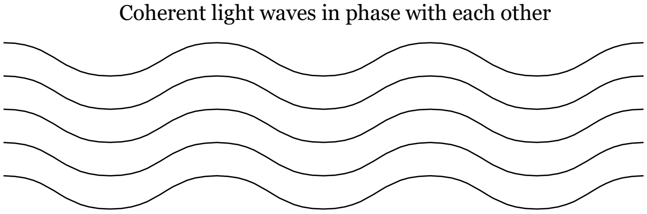

FIGURE 3.1
Coherent electromagnetic waves.

Laser Wavelength and Spectral Purity

Laser light is commonly considered monochromatic, meaning that all photons have nearly the same wavelength. Although lasers normally emit a range of wavelengths, the bandwidth of even the broadest-band laser is much narrower than that of ordinary light.

Laser Beam Divergence

Laser light can form tightly focused beams that travel long distances without spreading out like ordinary light. The most common definition of beam divergence is based on the spreading angle measured in milliradians (mrad). The divergence of most CW lasers is around 1 mrad, whereas for pulsed lasers it may be slightly larger. For reference purposes, a full circle, or 360°, equals 2π radians, 1 radian equals approximately 57.30°, and 1 mrad corresponds to 0.057°. Laser beam divergence is usually reported for the far field, at large distances from the laser, and the divergence angle is normally measured from the center of the beam to the edge. Most commonly, beam divergence is considered the angle between the beam sides. No matter how divergence is measured, calculating the size of the beam or the laser footprint diameter is a trigonometric problem (see Equation 3.1). Where do we consider the edge of the beam? Laser beam propagation can be approximated by assuming that the beam is a Gaussian-type beam, which means that the intensity profile follows a Gaussian function, with the transverse irradiance profile shown in Figure 3.2. This profile shows that the beam intensity gradually drops off toward the sides of the beam, and the beam edge is considered where intensity has fallen to $1/e^2$ or 13.5% of its peak, or maximum axial value.

Figure 3.3a shows an exaggerated divergence of a laser beam in a simplified representation that ignores the near range of the laser beam where the light rays remain parallel, sometimes called the "Rayleigh range."

$$D = 2H \tan(\theta/2) \tag{3.1}$$

where D is the beam diameter (diameter of illuminated area or footprint), H is the distance from the laser to the illuminated spot (flying height for airborne laser scanning), and θ is the divergence angle.

For a small divergence angle and large distances occurring in airborne laser applications, the angle in radians offers a good enough approximation of its tangent function; therefore, a commonly used formula is

$$D = H\theta \tag{3.2}$$

For example, for a beam with a divergence of 1 mrad and a distance of 1000 m, the footprint diameter becomes 1 m. With airborne laser scanning, the illuminated footprint size and shape is also affected by the scanning angle and the slope of the terrain. With airborne laser scanning, Equation 3.2 can be used for calculating footprint diameter of laser beams at nadir, but for laser beams at a certain scan angle on a flat terrain, Equation 3.3 provides a more appropriate calculation using trigonometry with triangles ABC and ABD shown in Figure 3.3b:

$$D = H\left[\tan\left(\theta_{\text{scan}} + \frac{\theta}{2}\right) - \tan\left(\theta_{\text{scan}} - \frac{\theta}{2}\right)\right] \tag{3.3}$$

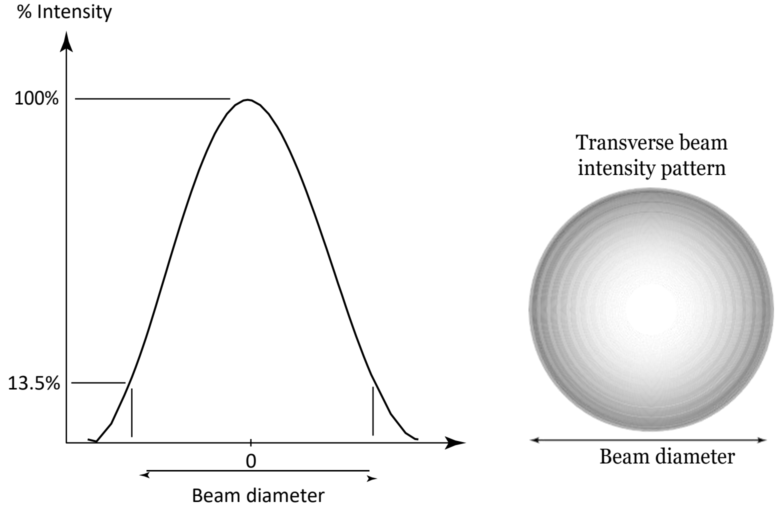

FIGURE 3.2
Transverse beam intensity pattern and beam diameter.

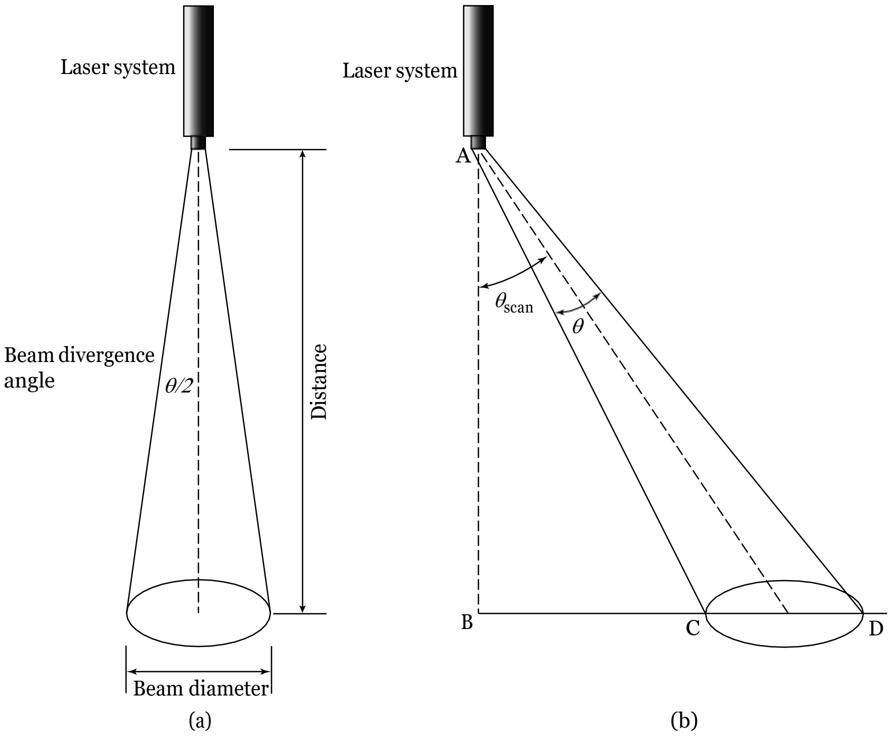

FIGURE 3.3
Beam divergence at (a) nadir and (b) a certain scan angle.

A formula that is easier to use can be derived from Equation 3.3 by considering the laser path distance equal to $H/\cos(\theta_{scan})$. Projecting the footprint on the flat terrain gives the following formula:

$$D = \frac{\square H}{\cos^2\theta_{scan}}\theta \tag{3.4}$$

For the example given for Equation 3.4, for a beam with a divergence of 1 mrad and a flying height of 1000 m, the footprint diameter at a scanning angle of 20° from nadir becomes 1.13 m. For inclined terrain, the footprint size calculation becomes more complicated, with details and formulas given by Baltsavias.

Laser Ranging

Laser range finding uses the same principles as radar distance measurements, with the major difference being the use of shorter wavelengths of the electromagnetic spectrum. The basic principle of laser ranging is the measurement of the time it takes for a laser signal to travel from the transmitter to the reflecting surface of a target and back to the receiver, although two major physical effects are used: For pulsed lasers, the traveling time of light pulse is measured and converted to a distance estimate, whereas for CW lasers, ranging is obtained by measuring the phase difference between the transmitted and the received signals. These range-finding techniques belong to time-of-flight (TOF) methods. Soon after lasers were invented, precise distance measurements were obtained through laser range finding. In the late 1960s, the National Aeronautics and Space Administration (NASA) used lasers to measure the distance from the Earth to reflectors installed on the Moon by Apollo missions. Armed forces use lasers to measure distances to targets on the battlefield, whereas a plethora of handheld laser range finders are used in hunting, golf, archery, and other sports. Terrestrial field surveyors and engineers also use range finders, more recently coupled with theodolites in total stations. With respect to laser ranging for remote-sensing purposes, laser sensors are installed on air- or spaceborne platforms, which most commonly employ pulsed laser systems with scanning technology. Ground-based laser sensors are installed on tripods and are capable of scanning targets on the ground from various angles.

Most laser ranging applications use pulsed lasers, usually solid-state lasers with high power outputs. A common laser type is the neodymium-doped yttrium aluminum garnet (Nd: YAG) laser, which emits light with a wavelength of 1064 nm, in the infrared portion of the electromagnetic spectrum, with pulse widths around 10 nanoseconds and several megawatts of power.

For range measurements with pulsed lasers, the laser system measures the traveling time between the emitted pulse and the received echo, and the distance between the ranging unit and the target surface is calculated by

$$D = c\frac{t}{2} \tag{3.5}$$

where c is the speed of light and t is the pulse travel time; t is divided by two since the pulse travels twice the distance to the target, that is, from transmitter to target and from target to receiver.

Travel time is measured by a time counter relative to the leading edge of the pulse (Figure 3.4). The leading edge is not well defined, but generally it is considered as a fraction of the signal peak to avoid issues caused by various pulse amplitudes.

For accurate range measurements, the laser pulse should be short. Equation 3.6 relates range resolution (ΔD) and time resolution (Δt):

$$\Delta D = c\frac{\Delta t}{2} \tag{3.6}$$

Equation 3.6 shows that the range resolution is determined by the resolution of the time interval measurement. As such, for a 10-nanosecond pulse, the range resolution is 3×10^5 km/s $\times 10^{-8}$ s/2 = 1.5 m. Equations 3.5 and 3.6 show that range measurement accuracy does not depend on the distance. The term "resolution" should not be confused with range measurement accuracy. Range resolution refers to the smallest change in the distance that can be resolved with the TOF laser. Range accuracy refers to the largest total error in measuring distances and is usually in the order of centimeters for airborne laser range finders, although it differs in the vertical and horizontal axes.

For CW lasers, ranging is obtained by modulating the laser intensity with a sinusoidal signal. The traveling time is proportional to the phase difference between the transmitted and the received signals, and the distance information is extracted from the received signal by comparing its modulation phase with that of the emitted signal. Due to laser complexity in achieving a similar ranging performance to pulsed lasers, CW lasers are rarely used.

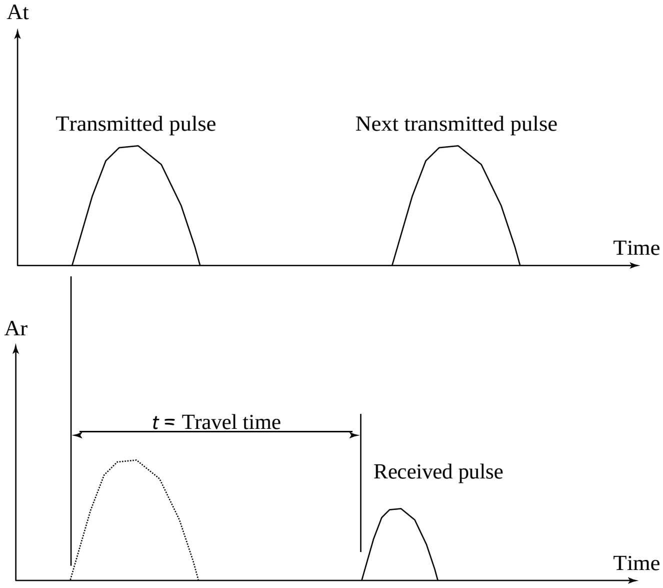

FIGURE 3.4
Variation of beam power level with time.

Laser Ranging Power Balance

Airborne and satellite laser range measurements are influenced by atmospheric conditions, laser power, and the reflectivity of the target. The power of the laser echo received at the sensor is directly proportional to target reflectivity. Table 3.2 shows the typical reflectivity of various materials for a laser wavelength of 900 nm. Range and reflectivity are directly related, or more specifically, the range is proportional to the square root of reflectivity.

$$R \propto \sqrt{\rho} \tag{3.7}$$

Equation 3.7 can be used to determine a correction factor for maximum laser range depending on the reflectivity of the target, as shown in Figure 3.5. As the figure shows, targets with a reflectivity of 40% restrict maximum range to about 70% of the maximum range for a target with 80% reflectivity. When flying an airborne laser scanning system over forests with mixed species, coniferous and deciduous, it is important to be aware of the maximum range limitations for the two species types. For coniferous trees with a typical reflectivity of about 30%, the maximum range is approximately 60% of that for deciduous trees, which have a typical reflectivity of about 60%.

The reflectivity of a target also affects the minimum size of a detectable object. For example, if we ignore the influence of other factors, such as atmospheric conditions, target shape, or terrain slope, a laser system that is capable of measuring the distance to a target with a reflectivity of 30% should be capable of detecting a target with a reflectivity of 60% that is half the size of the less-reflective target.

TABLE 3.2

Reflectivity Values for Various Diffuse Reflecting Materials and Surfaces, Natural and Human-Made, for a Laser Wavelength of 900 nm

Material	Reflectivity
White paper	Up to 100%
Dimension lumber (pine, clean, dry)	94%
Snow	80%–90%
White masonry	85%
Limestone, clay	Up to 75%
Deciduous trees	Typically 60%
Coniferous trees	Typically 30%
Carbonate sand (dry)	57%
Carbonate sand (wet)	41%
Beach sands, bare areas in dessert	Typically 50%
Rough wood pallet (clean)	25%
Concrete, smooth	24%
Asphalt with pebbles	17%
Lava	8%

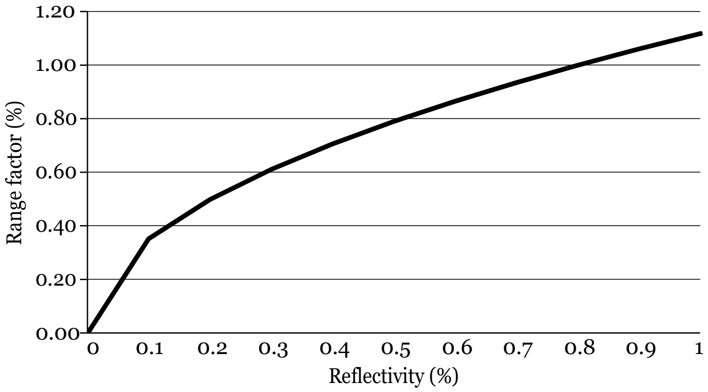

FIGURE 3.5
Correction factor for maximum laser range based on target reflectivity (normalized for 80% reflectivity).

Enabling Technologies

In the late 1960s, NASA used lasers to measure the distance from the Earth to reflectors installed on the Moon by Apollo missions. About 3 decades later, since the mid-1990s, laser ranging using airborne and terrestrial scanners became accepted as a proven technology with multiple applications for the surveying and mapping communities. There are no major differences between the optical and mechanical principles of airborne, spaceborne, and terrestrial lidar scanning systems, other than those in the mounting platforms and the complexity of additional technologies for determining sensor position and orientation. These additional or enabling technologies, along with advances in laser sensor technology, have defined the developmental stages of scientific and commercial laser scanning systems.

Global Positioning System Unit

Global positioning system (GPS) units have become essential components of navigation systems and surveying tools. This system is a key component of "direct georeferencing," which consists of the direct recording of the position and orientation parameters of a remote sensing instrument used for registering the acquired data to a geographic coordinates system. Mapping applications of direct georeferencing include aerial photogrammetry and airborne lidar.

Inertial Measurement Unit

The inertial measurement unit (IMU) is sometimes referred to as a part of the inertial navigation system (INS), which integrates other components in addition to the IMU, such as a navigation processor to handle navigational computations, a GPS, an electronic compass, or a barometric system. The IMUs detect motion with respect to a hypothetical stationary reference system and normally contain three gyroscopes and three accelerometers, all orthogonal, measuring angular velocities and linear accelerations, respectively. By processing the signals from these devices, normally recorded at a frequency of 50–1000 Hz, it is possible to track the position and orientation of the device, the current rate of acceleration, and changes in rotational attributes, including pitch, roll, and yaw.

In an airborne lidar application, the IMU is used to measure the orientation of the laser beam at the exact time of a range measurement. Most commonly, the IMU is mounted rigidly to the lidar sensor housing in order to provide orientation parameters with respect to the laser reference point, which can be the laser scanning mirror or the fiber optic bundle, depending on the sensor scanning principle. A calibration process known as "boresight calibration" corrects for the mounting misalignment between the IMU and the lidar reference frame. Typically, the boresight calibration of a sensor requires airborne calibration using a reference surface test to correct for pitch, roll, and heading offsets.

The GPS-aided INS provides direct measurement of the position and orientation parameters and is also referred to as a direct georeferencing system. When used with a remote sensor, such as a lidar sensor or a digital camera, direct georeferencing provides all the information needed to register the acquired data in geographic coordinates. Since the mid-1990s, direct georeferencing has become an alternative to aerial triangulation by either totally replacing it or complementing it. Aerial triangulation is used to solve for aerial photography camera exterior orientation parameters, which convey the information necessary to tie image measurements to ground coordinates for planimetric and topographic map compilation, orthophoto production, and digital terrain model editing. Direct georeferencing systems are integral components of airborne remote sensing systems, including lidar, interferometric synthetic aperture radar, and digital cameras.

Components of a Lidar System

A lidar system may include different components depending on the mounting platform. These can be air- or spaceborne components or ground-based components. Ground-based lidar systems, also referred to as "terrestrial" lidar or laser scanning systems, can be mounted on mobile and fixed, but portable, platforms. Air- or spaceborne instruments can fly on rotary or fixed-wing platforms and satellites, respectively. The basic components of an airborne lidar system are shown in Figure 3.6. For airborne systems, the three main components include (1) a laser ranging unit, (2) an orientation unit, most commonly referred to as the IMU and (3) the GPS unit. Computer hardware and software integrate data streams coming from all components and provide data storage and a variety of post-acquisition registration, processing, and export functions. Terrestrial lidar systems vary in complexity and may include the same components as an airborne system, especially for mobile units mounted on vehicles or boats, or may have a simpler construction for fixed units mounted on a tripod. The latter types may include only the laser ranging unit, a computer, data storage components, and an optional digital camera.

The IMU describes the orientation or the attitude of the unit in terms of roll, pitch, and yaw (Figure 3.7) and serves the characterization of flight dynamics and the derivation of accurate ground coordinates for each laser shot. The GPS unit consists of an onboard differential GPS receiver, which is commonly assisted by one or more ground stations for improving the accuracy of laser footprint coordinates after post-processing.

By knowing the location of the sensor platform and the sensor in three-dimensional (3D) coordinates (GPS-provided data), the trajectory of the laser beam provided by the orientation of the sensor (IMU data), the angle of the laser pulse relative to the sensor, recorded by the laser scanning device, and the range to targets on the Earth's surface as measured by the laser ranging unit, we can compute accurate 3D coordinates for each laser footprint

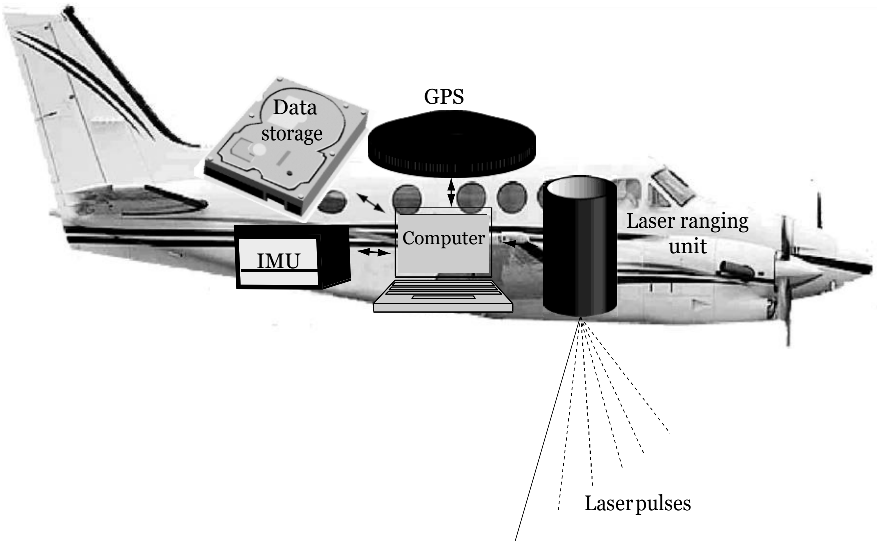

FIGURE 3.6
Basic components of an airborne lidar system. GPS = global positioning system; IMU = inertial measurement unit.

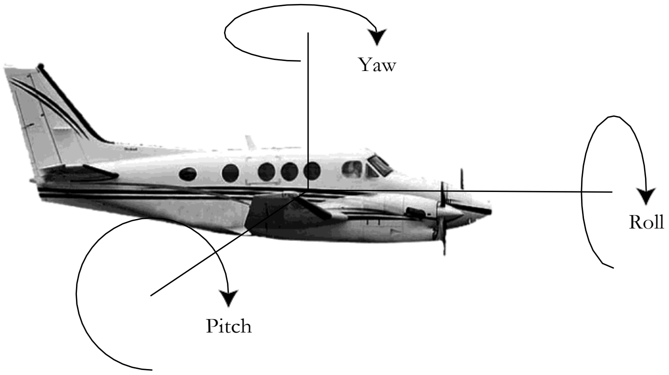

FIGURE 3.7
Orientation unit (inertial measurement unit) detects changes in roll, pitch, and yaw.

on the ground. All these data sources that allow the calculation of the 3D coordinates in a post-processing mode are integrated by computer hardware and software and linked together using a time stamp.

3.6.1 Laser Ranging Unit

The principles of laser ranging are described in Section 3.3. The pulse ranging measurement principle is employed by most airborne, satellite, and terrestrial systems, and they commonly include a laser transmitter and a receiver, each with their associated optics. The laser ranging unit may be coupled with an optical and mechanical scanning unit that deflects the laser beams across their flight path to collect a swath of ranging data.

The transmitter part of the laser ranging unit expands the laser beam to reduce the area density of the laser-pulse-transmitted energy and controls the divergence of the laser beam. The receiver part works as a photodiode by converting the backscattered laser light intensity into electrical impulses. The received laser power of the backscattered echo is only a small fraction of the transmitted power.

Types of Laser Sensors

Different lidar sensors may have similar components, but the recorded data may be of distinct formats. This section categorizes lidar sensors based on their ability to record discrete returns or waveform data and presents the three different platforms used for acquiring lidar data, terrestrial, airborne, and satellite-based.

Discrete-Return Lidar Sensors

The design of the receiver part of the laser ranging unit is particularly important as it may determine the type of lidar data the receiver records—discrete return measurements or the full waveform. In the first case, a laser pulse may provide multiple returns depending on the type of surface it intercepts. When the laser beam hits porous objects, such as the forest canopy, it may intercept foliage or tree branches over part of the laser footprint, which may backscatter enough energy to trigger the recording of the travel time by the laser receiver (Figure 3.8). After hitting the top of the canopy, part of the laser beam may continue its travel through openings in the canopy until it again hits another layer of foliage or branches, or possibly the ground, which may generate secondary returns of the same pulse. Depending on the complexity of the forest canopy and the settings of the laser receiver, a laser pulse may generate up to four or five discrete returns, sometimes with less dependence on the limitations imposed by the receiver.

Ideally, a laser pulse hitting the forest canopy would provide a return from the top of the canopy—the first return in Figure 3.8—and it would still be able to penetrate to the ground and record a last return from the forest floor—the third return in Figure 3.8. Such measurements allow us to accurately characterize vegetation height and the terrain elevation under the canopy. Some of the laser pulses intercepting the canopy may provide only one return when foliage, branches, or tree trunks block the entire footprint or when these pulses hit the bare ground without intercepting tall layers of vegetation. Similarly, when the laser footprint covers completely nonporous objects, such as roofs, sides of buildings, or other human-made structures, the laser pulse will provide only one return. Therefore, discrete-returns lidar data include first returns, intermediate returns, and last returns.

Most discrete-returns lidar sensors use constant fraction discriminators (CFDs) to minimize the “range walk” or systematic variation in range with signal level. Backscattered laser signals have varying amplitudes depending on the initial pulse energy, size of the intercepted object, and target reflectance characteristics. In order to handle such variations, most laser receivers use a constant amplitude ratio to identify a laser return and record its travel time and power, denoted as amplitude or intensity. The CFD is used to define the leading edge of the pulse (Figure 3.9), which, as explained in Section 3.3, is not well defined but generally considered to be a fraction of the signal peak to avoid issues caused by various pulse amplitudes.

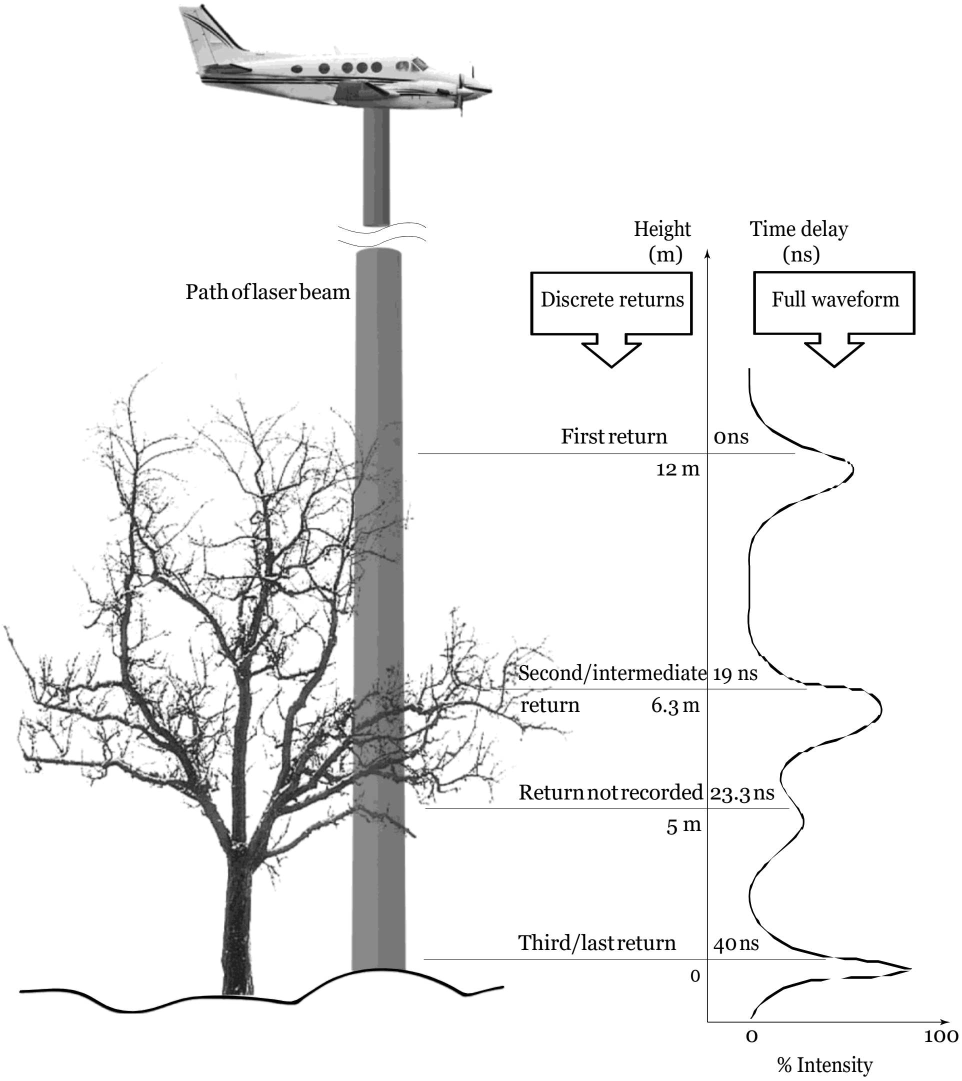

FIGURE 3.8
Laser beam interaction with vegetation and variation of the backscattered laser signal.

The CFD-based receivers need to reset their detectors to prepare for the next pulse or the next echo returned from the same pulse; therefore, there is a time separation between returns recorded for the same echo. Although the reset time, sometimes referred to as "nominal dead time," varies with sensors and manufacturers, it is most commonly around 8–10 nanoseconds. This reset time translates to a range separation of 1.2–1.5 m between the recorded returns of the same pulse, when considering to- and from-target travel times.

The reset time and the minimum range separation between multiple returns have implications for detecting ground covered by vegetation. When the ground is covered by tall grasses or shrubs with heights less than 1.2–1.5 m, the laser beam may provide a return from the top of the vegetation cover and may penetrate to the ground and generate a secondary ground return. This ground return may not be detected due to the fact

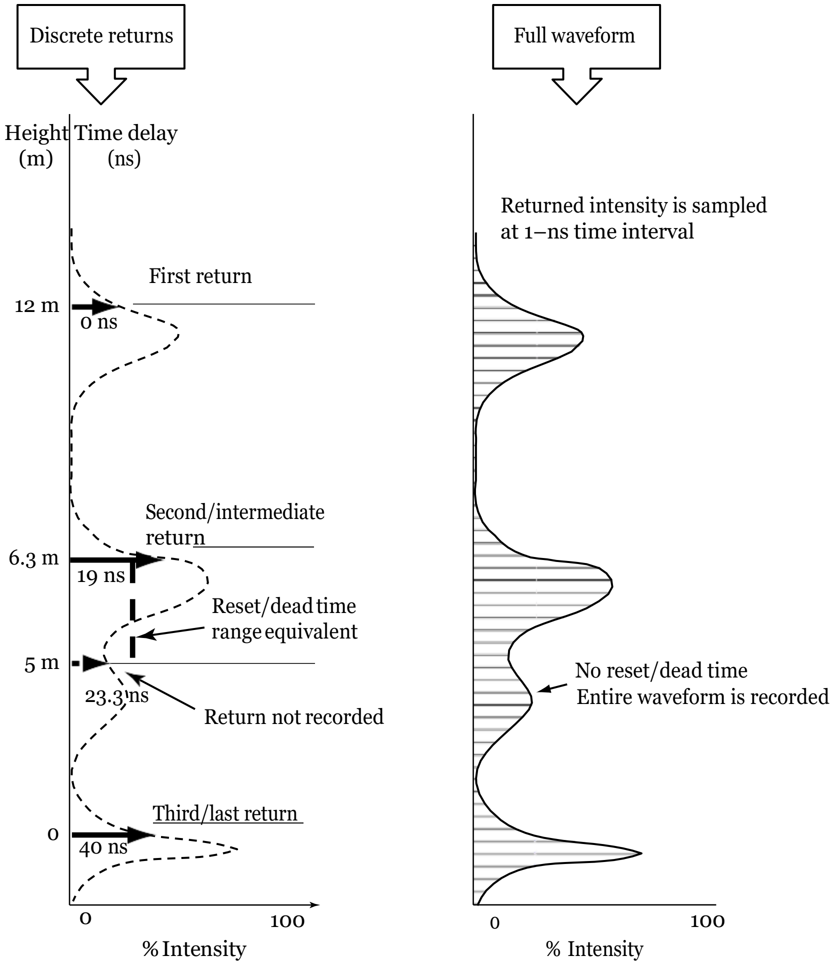

FIGURE 3.9
Conceptual differences between discrete-return and waveform lidar systems.

that no returns are recorded by the receiver within the reset time. This situation does not mean that characterizing ground elevation is always biased toward higher elevation values when there is a low layer of vegetation. A significant number of laser pulses will penetrate to the ground, and laser point classification algorithms will identify lower pulses that most likely hit the ground and use them to generate digital elevation models.

Some airborne lidar sensors manufactured during the mid-1990s could be toggled to record either the first or the last return, and two flights over the same area were necessary to get the bare ground terrain model and the top of the canopy surface, when flown over forest vegetation. Surveys in the U.S. Pacific Northwest carried out using the Optech ALTM 1020 scanning system indicated a minimum 2030% penetration of coniferous canopies. In the same region, with conifer-dominated stands and dense overstory, Means observed a very low penetration to the ground of only 1–5%, for a small-footprint lidar. Kraus and Pfeifer estimated a penetration rate of less than 25% for their lidar study in the Vienna Woods (Wienerwald), in Austria, using an Optech ALTM 1020 lidar system.

A study by Popescu, Wynne, and Nelson conducted in Virginia over forests of varying age classes including deciduous, coniferous, and mixed stands estimated the penetration rate for the last return laser hits, or first return when there was only one return, to be approximately 4%. The laser point density on the ground, for one flight line, was 0.47 points per square meter for the first return, and the last return when there was only one return; 0.20 points per square meter for the second return, less than half compared to the first return point density; 0.02 points per square meter for the third return; and 0.0001 points per square meter for the fourth return. None of the pulses were able to produce a fifth return for the given vegetation conditions, although the sensor, an AeroScan system that later became Leica's ALS40 sensor, was configured to receive up to five returns.

Since the early 1990s, discrete-returns lidar sensors have experienced major technological advances, reflected mainly in an increased pulse frequency, the recording of multiple returns for each pulse, the recording of intensity information, and the positional accuracy. The latest generation of airborne laser scanners has added waveform-recording capability and the ability to handle multiple pulses in the air. Systems that are able to track echoes from multiple pulses in the air have the potential to significantly increase the productivity of airborne lidar data acquisition systems as these systems, do not depend on receiving the target reflection before starting the next range measurement cycle. More pulses providing range measurements will enable lidar data users to fly a notably wider swath while maintaining the same point densities as conventional systems, or acquire significantly increased point densities for the same swath widths, leading to appreciably reduced flight costs in the end. Due to such innovative technological achievements developed by commercial laser systems manufacturers and the increased number of service providers, airborne lidar is used routinely for topographic mapping, vegetation assessment and forest inventory, 3D urban modeling, wireless communications planning, corridor mapping of power lines and oil pipes, and transportation planning, to mention just a few of the applications. Ground-based laser scanners have been used mainly for surveying and industrial 3D mapping.

Despite the advances in scanning lidar technology, a number of research groups are using airborne lidar profiling systems to extract elevation profiles along flight lines, mainly due to the lower cost of the sensor and the reduced data volume acquired during flight time. Such a system has been developed at NASA for forest research, called a "portable airborne laser system" (PALS), by Nelson, Short, and Valenti. This system is in fact based on off-the-shelf components, including a Riegl laser range finder, a Garmin GPS receiver, and a video camera.

Waveform Lidar Systems

Lidar sensors able to record the entire backscatter amplitude of the laser pulse are referred to as waveform lidar systems. Such sensors have been used from both airborne and satellite platforms.

Airborne Lidar Systems

Whereas discrete-returns lidar systems record, for each laser pulse, the time of travel and the intensity of every return, waveform lidar systems record the time-varying intensity of the returned energy from each laser pulse and therefore provide information on the height distribution of the returned intensity (Figure 3.9). The shape of the returned intensity offers a direct description of the vertical distribution of surfaces illuminated by the laser pulse and is useful in characterizing complex targets, such as forest canopy. The returned energy is digitized at equal time intervals, such as for every nanosecond.

Terrestrial applications using waveform lidar have been documented from the early 1980s. Aldred and Bonner were the first to describe an application of waveform lidar to study forest canopies in Canada. For their study, they used a laser system originally developed for characterizing bathymetric water depth and measured forest biophysical properties, such as tree height, canopy cover, and type of tree species—hardwoods, conifers, or mixed. They also studied the effect of different laser beam footprint sizes on stand-height estimates and found that the footprint diameter was not critical when estimating stand height. An interesting investigation in their study looked at different methods of estimating tree height by analyzing waveform start and end points and concluded that the leading edge threshold, followed by the peak-to-peak and trailing edge values, provided the best forest height estimates. Another bathymetric lidar system with dual frequency, 532 and 1064 nm, and waveform recording was used by Nilsson to measure tree heights and timber volume. The pulse length was 7 nanoseconds, the sampling interval was 2.5 nanoseconds, and the digitized waveform was a combination of the two, green and infrared, returns.

It has been proven that waveform lidar systems are most successful for vegetation analysis. NASA has developed experimental sensors that record the complete waveform from medium- and large-footprint lasers with a ground beam diameter between 5 m and tens of meters as predecessors of spaceborne lidar systems. Two NASA airborne research lidar systems have been used to characterize vegetation: the scanning lidar imager of canopies by echo recovery and the laser vegetation imaging sensor. The LVIS sensor emits laser pulses with a duration of 10 nanoseconds at full width half maximum (FWHM) and digitizes the detected return energy at 500 megasamples per second or every 0.5 nanoseconds. The LVIS beam diameter depends on the flying height, with a typical size of 10–25 m for its footprint. This sensor has a scan angle of about 12° and can cover 2-km swaths from an altitude of 10 km.

Commercial Waveform-Recording Small-Footprint Lidar

A discrete-returns lidar system has limitations with respect to the number of echoes it can record from a single pulse. A waveform-recording lidar overcomes this constraint by recording the entire laser pulse energy as a function of time. This approach to recording the laser backscatter amplitude with high frequency affords a better characterization of the vertical distribution of reflecting surfaces within the laser footprint, which for most of the commercial airborne sensors is smaller than 1 m in diameter.

As explained in Section 3.7.1, discrete-returns systems are affected by the reset time between separate returns of the same pulse, which translates to a range separation of 1.2–1.5 m between consecutive echoes, when considering to- and from-target travel times. This has implications for detecting ground covered by vegetation, such as tall grasses or shrubs, when the laser beam may provide a return from the top of the vegetation cover and penetrate to the ground and generate a secondary ground return.

By using adequate modeling of the recorded waveform, it has been shown that full-waveform analysis enables the extraction of additional information compared to discrete-return systems, such as the range to the ground peak underneath tall grasses, shrubs, or forest vegetation. Most often, wave- form analysis extracts range, elevation variation, and reflectance properties from the pulse width and amplitude. In their study conducted in 2005, Gutierrez, Neuenschwander, and Crawford compared the elevations derived from a conventional discrete-return system with waveform data collected using the same sensor, an Optech ALTM instrument, and found that elevation data agree well between the two datasets. They also concluded that the waveform data provided increased information about the vertical distribution of reflecting surfaces. A common approach to extracting information from waveform data is to model the waveform as a series of Gaussian distribution functions, as demonstrated for LVIS by Hofton, Minster, and Blair , or Persson et al.

Some of the commercial airborne lidar systems are able to collect waveforms for small-footprint laser beams, such as the Riegl LMS-Q680, TopEye Mark II, or Optech's ALTM 3100. Some sensor manufacturers, such as Optech and Leica, provide the option of waveform digitizer modules that can be integrated with their discrete-return systems to allow full-waveform digitization.

Spaceborne Lidar Systems

The lidar waveform-recording technology developed for the NASA airborne systems made use of prototypes of methods and techniques later used by spaceborne altimeter systems such as the shuttle laser altimeter, which in 1996–1997 provided the first global-scale laser altimeter dataset. In 1997, the Mars orbiter laser altimeter (MOLA), an instrument used aboard the *Mars Global Surveyor* spacecraft, acquired its first pass across the surface of Mars. The altimeter obtained measurements of topographic profiles, surface reflectivity, and backscattered laser pulse width, with surface spot sizes of 70–300 m. The next space-based system was the geoscience laser altimeter system (GLAS) carried on the ice, cloud and land elevation satellite (ICESat), which was launched on January 13, 2003 from the Vandenberg Air Force Base in California.

An overview of the ICESat mission is provided by Schutz et al. The ICESat laser measurements were designed with the primary objective of monitoring ice sheets mass balance. Measurements are currently distributed in 15 science data products, which have interdisciplinary applications, including the characterization of land topography and vegetation canopy heights. The system operates by sending laser pulses with a frequency of 40 Hz and pulse duration of approximately 5 nanoseconds. The returning laser echo is sampled every nanosecond, and the digitized pulses are referred to as laser waveforms. The ICESat platform orbits at an altitude of approximately 600 km, and from that height above the ground, the laser footprints have approximately a 64-m circular diameter. More precisely, the footprints are elliptical, with their size and ellipticity varying during the course of the mission. Along one orbital transect, the footprints are spaced at about 172-m intervals. The GLAS surface elevations are reported with respect to the TOPEX/Poseidon reference ellipsoid. Among all GLAS standard products, the level-1 altimetry products, GLA01, contain waveforms digitized in 544 bins with a bin size of 1 nanosecond or equivalently 15 cm; however, beginning with the data acquisition phase L3A, the bin size of BIN 1-151 has been changed to 4 nanoseconds (60 cm) to reduce the risk of waveform truncation. The level-2 global land-surface products, GLA14, provide an alternate fitting that locates up to six Gaussian components (mode, amplitude, and sigma) to characterize the shape of the total waveform. The ICESat spacecraft allows for off-nadir pointing of the laser, by up to ±5°, in order to target areas of interest or to com- pensate for orbit drift.

Flash Lidar

An alternative to scanning the target of interest with pulses of laser light is offered by the flash lidar technology. Rather than using one receiver to detect echoes from each laser pulse, flash lidar uses a focal plane array as a detector to acquire a frame of 3D data from a laser pulse that floods the scene. The concept of the flash lidar detector is similar to that of the focal plane array of a two-dimensional optical digital camera. Each pixel in the array configuration can independently measure the travel time for each laser pulse.

The sensor captures an entire frame of range data from a single pulse of laser light with a certain frequency, such as 60 frames per second. Just like scanning lidar sensors, flash lidar sensors are capable of capturing both range and intensity data.

At the time of this writing, little information is available about the flash lidar technology. Few companies pursue the development of this technology, such as Ball Aerospace & Technologies Corp., Boulder, CO, and Advanced Scientific Concepts, Inc., Santa Barbara, CA.

Ground-Based Lidar

Over the last 30 years, lasers have been incorporated into surveying instruments such as simple range finders or more complex total stations. Such uses of lasers have led to the development of ground-based or terrestrial lidar scanners, which are capable of scanning the landscape surrounding their location. Most of the time, such sensors are set up on a tripod or on vehicles, and they are respectively called “static” and “dynamic” or “mobile” systems. Static systems do not require the integration of supporting technologies or units, such as GPS and IMUs, whereas mobile systems need direct georeferencing through the use of GPS and IMUs.

Ground-based lidar systems have developed considerably over the last decade, and the use of such sensors has resulted in the proliferation of a large number of applications, from surveying, architecture, accident scene reconstruction, monitoring of buildings and bridges, measurement of complex industrial facilities, monitoring of quarries and open mines, and recording of building and monument facades, to geological structures and vegetation analysis.

Most of the ground-based lidar systems utilize the TOF principle for range measurements, although a few employ the phase measuring technique. Depending on the coverage they are capable of illuminating with lidar points, ground-based lidar systems can be differentiated as panoramic, hybrid, or camera-type scanners. Panoramic scanners cover the surrounding landscape in a systematic pattern with 360° coverage in the horizontal plane and more than 270° in the vertical plane, practically missing only the area below the instrument’s tripod in covering a full spherical field of view. Although the hybrid scanners are capable of scanning a 360° field of view in the horizontal plane, they may have limited scanning angles toward the zenith, since most such scanners are used for topographic applications and are not required to scan objects overhead. The camera- type scanners normally have a limited field of view in both horizontal and vertical planes. Panoramic scanners are the most versatile for indoor or outdoor applications and can be set to cover a limited viewing angle, if so desired.

With respect to the range over which ground-based systems can be used, depending on the manufacturer and the intended application, such systems can record ranges from 100 m to 1 km. The most common terrestrial sensors are manufactured by the same companies that build airborne lidar sensors, such as Leica, Optech, and Riegl, although there are other systems as well, such as Trimble, Topcon, or research systems like Echidna.

With the development of dynamic terrestrial laser scanners, mobile mapping literally takes on new dimensions. The mobile lidar technology has in fact many similarities with airborne lidar, mainly in requiring continuous georeferencing of the moving vehicle that carries one or more sensors. As such, the mobile lidar technology integrates GPS and IMU components. Such systems are mainly used in the urban environment for reproducing facades of buildings from the ground level, which can be integrated with airborne datasets for producing accurate and complete 3D urban models.

Lidar Data Format

Until recently, discrete-return lidar data were provided in text or binary format, which was usually proprietary, most commonly with geographic coordinates and intensity recordings for multiple returns and pulses making up the point cloud. The drawback of this approach was the lack of portability and consistency among software tools used for processing the datasets from different providers or different sensors. The first version of a standard lidar file format, the LAS 1.0, was released in 2002 with the intention of allowing different lidar hardware and software tools to output data in a common format. The initial LAS specification was a relatively compact binary encoding of point location and point attribute data. The third revision of the LAS format specification was released in July 2009, and it is owned by the American Society for Photogrammetry & Remote Sensing (ASPRS). The LAS 1.3 specification includes a noteworthy improvement over previous specifications, that is, the possibility of encoding lidar waveform data. In addition, the LAS 1.3 includes important information regarding the sensor used to collect lidar data, processing software, number of lidar points, point coordinates, intensity, classification, and other relevant data. Table 3.3 shows the standard lidar point classes in LAS 1.3.

TABLE 3.3

Standard Lidar Point Classes in the ASPRS LAS 1.3 Data Format

Classification Value (Bits 0:4)	Meaning
0	Created, never classified
1	Unclassified 1
2	Ground
3	Low vegetation
4	Medium vegetation
5	High vegetation
6	Building
7	Low point (noise)
8	Model key point (mass point)
9	Water
10	Reserved for ASPRS definition
11	Reserved for ASPRS definition
12	Overlap points 2
13–31	Reserved for ASPRS definition

Examples of Environmental Applications of Lidar Remote Sensing

Environmental applications of lidar remote sensing cover a wide spectrum, such as applications in environmental engineering, mapping geologic faults under the forest canopy, monitoring coastal changes, assessing landslide hazards, quantifying the growth and retreat of ice sheets, and estimating vegetation structural attributes, biophysical parameters, and habitat characterization. Developments in lidar remote-sensing applications for environmental studies are occurring rapidly, and they are driven by intensive research and increasing availability of lidar data from commercial and governmental sources. Two general application trends can be observed: (1) characterizing the topographic features and (2) assessing the 3D structure of vegetation canopies. Topography mapping with lidar remote sensing is potentially the fastest-growing area of environmental applications. Most environmental studies need topographic information, and lidar has proven its ability to acquire highly accurate and detailed elevations, which have a strong influence on the structure, spatial extent, composition, and function of ecological systems. Most often, topographic applications use discrete-returns lidar data provided by commercial remote sensing companies. When deriving topographic information, a substantial number of lidar points in the point cloud, mainly representing vegetation hits, are discarded in the step known as "vegetation removal." On the contrary, for most ecological applications that use discrete-returns lidar data, the lidar returns from the canopy are of the highest interest. In addition to the discrete-return airborne systems, waveform lidar data have been used for characterizing vegetation structure over large areas. Since topographic lidar applications have been described in great detail in other texts, such as the works of Maune or Shan and Toth.

Lidar for Estimating Forest Biophysical Parameters

The use of remote sensing in mapping the spatial distribution of canopy characteristics allows an accurate and efficient estimation of tree dimensions and canopy properties at local, regional, and even global scales. In particular, lidar remote sensing has the capability to acquire direct 3D measurements of the forest structure that are useful for estimating a variety of forest biophysical parameters, such as tree height; crown dimensions, canopy closure, leaf area index, tree density, forest volume, and forest biomass, and in mapping fire risk by assessing surface and canopy fuels.

During the late 1980s, a number of lidar studies for estimating tree height, forest biomass, and carbon date were conducted, for example, studies by Maclean and Krabill, Nelson, Swift, and Krabill, and Nelson, Krabill, and Tonelli. These first studies used profiling lidar systems and developed models to predict stem volume and dry biomass based on forest canopy height and closure as measured by airborne lidar. Since then, numerous researchers have used a variety of lidar systems and sampling techniques to quantify tree dimensions, standing timber volume, aboveground biomass, and carbon date, mainly with scanning systems.

Previous lidar studies, whether using waveform or discrete-return lidar data, attempted to derive measurements, such as tree height and crown dimensions, at stand level, plot level, or individual tree level and then use allometric relationships or statistical analysis to estimate other characteristics, such as biomass, volume, crown bulk density, and canopy fuel parameters. Figure 3.10 shows a lidar point cloud with a point density of 8 points per square meter collected by a discrete-return sensor over coniferous forests in the western United States. Figure 3.11 displays the ground-based lidar data acquired from a tripod system in Mesquite forests in central Texas.

Forest canopy structure was estimated using data from scanning lasers that provided lidar data with full-waveform digitization. Small-footprint, discrete-returns systems were used to estimate canopy characteristics, with many studies focusing on tree height or crown dimensions, such as the study conducted by Popescu, Wynne, and Nelson. Figure 3.12 shows a portion of a canopy height model of mixed forest conditions in the southern United States. The canopy model has been processed automatically with methods described by Popescu and Wynne in identifying individual trees, and their heights and crown dimensions have been measured.

After more than two decades of research in vegetation assessment with lidar, the following four aspects could be concluded: First, with waveform lidar systems having large footprints, robust regressions can be developed to predict volume and biomass over large area extents. The R^2 values for plot-level models range from 0.8 to 0.9.

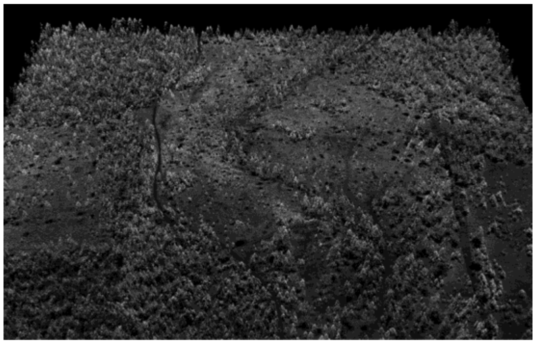

FIGURE 3.10
(See color insert following page 426.) Lidar point cloud over coniferous forests in the western United States.

FIGURE 3.11
(See color insert following page 426.) Ground-based lidar data collected over Mesquite trees in central Texas.

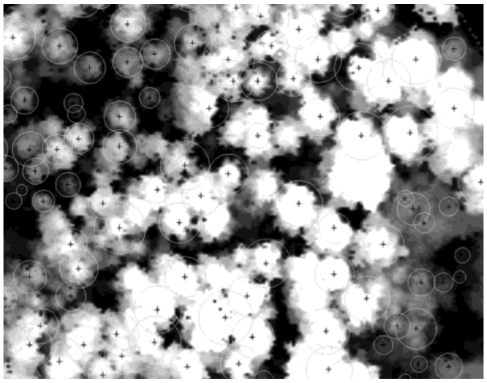

FIGURE 3.12
(See color insert following page 426.) Automatically measuring individual trees on a lidar-derived canopy height model. Circles represent computer-measured crown diameters, whereas each cross sign indicates identified individual trees.

With discrete-returns systems, that is, scanning lidar systems with small footprints, usually of submeter range, the strength of the prediction models for volume and biomass are more variable, with R^2 values ranging from 0.4 to 0.9. Second, conifer attributes can be estimated with higher accuracy than hardwood parameters. The evidence for this statement is found scattered throughout the literature and may be attributed to the more complex canopy structure of deciduous stands and individual tree growth form, which make height–volume or biomass relationships noisier for hard- woods. Third, despite intense research efforts and few operational uses, there is a lack of lidar processing tools and, thus, investigators are spending considerable efforts on developing software. Fourth, airborne lidar data can be used to inventory biomass and carbon at scales from local to regional and global. With scanning lidar, biomass and carbon can be accurately estimated at local scales; for examples, see the studies by Popescu et al. Using profiling lidar data, as in the studies of Nelson, Short, and Valenti , biomass and carbon can be estimated over large areas, whereas satellite lidar (e.g., ICESat/GLAS) can be used for global estimates of canopy properties.

Lidar Applications for Estimating Surface and Canopy Fuels

Few lidar studies focus on assessing canopy structure and characteristics, such as fuel weight, canopy and crown base height, and crown bulk density. Among these studies, there seems to be a unanimous acceptance that airborne lidar over- estimates crown base height for individual trees or plot-level canopy base height, which is an intuitive finding given the fact that airborne lidar portrays crowns from above, and lower branches have a reduced probability of being intercepted by laser pulses that might be blocked by higher branches.

Lidar Remote Sensing for Characterizing Wildlife Habitat

Ecologists have long recognized the importance of vegetation structure for characterizing wildlife habitat, but field methods for gathering such information are time consuming and challenging. Vertical forest structure is related to biodiversity and habitat. “In general, the more vertically diverse a forest is the more diverse will be its biota …”. Remote sensing techniques provide an attractive alternative, especially when 3D data are acquired directly with sensors such as lidar.

Hinsley et al. and Hill et al. employed an airborne laser system to assess bird habitat. They used an airborne laser scanning system to map forest structure across a 157-hectare deciduous woodland in the eastern United Kingdom. The researchers related laser-based forest canopy heights to chick mass (i.e., nestling weight), a surrogate for breeding success, which, in turn, is a function of “territory quality.” They found that for one species, chick mass increased with increasing forest canopy height, and for a second species, chick mass decreased. Hill et al. concludes that airborne laser scanning data can be used to predict habitat quality and to map species distributions as a function of habitat structure.

Nelson, Keller, and Ratnaswamy mapped and estimated the areal extent of Delmarva fox squirrel (DFS) habitat using an airborne profiling lidar flown over Delaware. The study results indicated that (1) systematic airborne lidar data can be used to screen extensive areas to locate potential DFS habitat; (2) 78% of sites meeting certain minimum length, height, and canopy closure criteria will support DFS populations, according to a habitat suitability model; (3) airborne lidar can be used to calculate county and state acre- age estimates of potential habitat; and (4) the linear transect data can be used to calculate selected patch statistics.

Hyde et al. used a large-footprint (12.5 m) scanning lidar to map California spot- ted owl habitat across a 60,000-hectare study area in the Sierra Nevada, California. They looked at forest canopy height, canopy cover, and biomass in the mountainous forests. Their ultimate objective was to produce maps for the U.S. Forest Service for wildlife habitat and forest resource management and to conclude that lidar provides “important metrics that have been exceptionally difficult to measure over large areas.”

Recent studies, such as the ones conducted by Clawges et al. or Vierling et al., show the potential of using airborne lidar in studying animal–habitat relationships and in quantifying the vegetation structural attributes important for wildlife species. Clawges et al. used lidar to assess avian species diversity, density, and occurrence in a pine aspen forest in South Dakota. They concluded that lidar data can provide an alternative to field surveys for some vegetation structure indices, such as total vegetation volume, shrub density index, and foliage height diversity. They calculated different foliage height diversity indices using various foliage height categories and found that habitat assessment may be enhanced by using lidar data in combination with spectral data.

Lidar Systems for Atmospheric Studies

Although this chapter focuses on lidar remote sensing for environmental applications, laser remotesensingtechnologiesarealsousedefficientlyforprovidingfour-dimensional—space and time—measurements of the atmosphere and its constituents. Range-resolved measurements of the atmosphere have been carried out from the ground, air, and space.

In fact, Middleton and Spilhaus, who are credited with coining the lidar acronym, did so in the context of meteorological instruments, but without expressly mentioning what it could be the acronym of. Fiocco and Smullin described atmospheric measurements with a ruby laser in 1963. Currently, lidar systems used in atmospheric studies observe spatial and temporal distribution of atmospheric gases, atmospheric pressure, temperature, turbulence, and wind. Physical processes observed with these lidars include laser backscattering by aerosols and clouds (Mie scattering), laser backscattering by molecules (Rayleigh scattering), absorption by atoms and molecules (differential absorption lidar [DIAL]), Raman scattering, fluorescence, and Doppler shift by aerosols and clouds (Doppler lidar). These lidar systems are not discussed further in this book. Similarly, this book does not discuss short-distance laser remote sensing technologies used in industrial, security, and medical applications. Interested readers can find a relatively rich lidar literature for atmospheric studies both in book and scientific articles formats, for example, studies by Fujii and Fukuchi.

Conclusions

Lidar data availability is increasing along with the spectrum of lidar applications in environmental remote sensing at a multitude of scales and the user's need for up-to-date information on sensors, processing algorithms, and applications. As such, the goal of this chapter is to provide the fundamentals of lidar remote sensing technology and some examples of environmental applications of this technology for characterizing the 3D structure of vegetation canopies.

The present widespread use of lidar remote sensing offers an optimistic vision of the future for environmental applications and research investigations. Intrinsic lidar data structure allows the integration of data acquired by different platforms, terrestrial, airborne, and spaceborne, as complementary or validation tools for applications at multiple scales from local to regional and global. In addition, the fusion of lidar and optical or radar data aims at reducing the limitations of each technology and utilizing their synergistic characteristics for complex environmental assessment. In the context of global climate and environmental changes, lidar proves to be an important technology that makes possible the analysis of the 3D structure of vegetation canopies and facilitates operational applications and scientific discovery. There is no doubt that lidar will continue to be one of the most important geospatial data acquisition technologies subject to continuous developments of all its components: acquisitions systems and hardware, data formats, processing algorithms and software, operational principles, quality, accuracy, and standards.